UNIVERSITY OF MODENA AND REGGIO EMILIA
Department of Engineering

MUNER ADVANCED AUTOMOTIVE ENGINEERING

Advanced Powertrain

Damping System modelling for multi-body analysis of Moon-Mars Lander landing phase

Academic tutor:

Prof. Antonio ZIPPO

Candidate:

Attilio MARASCO

Company tutor:

Eng. Matteo MARRONE

Academic Year 2024/2025

ABSTRACT

In 1609, a man pointed an instrument toward the sky for the first time and saw space with new eyes. Galileo Galilei, with his telescope, broke the barriers of knowledge and paved the way for the era of scientific exploration. His discovery not only changed our view of the cosmos but laid the foundations for the technological advancements that, centuries later, would take us beyond Earth's boundaries.

About 360 years later, another revolution was underway. It was December 24, 1968, and for the first time in history, humankind observed Earth from a new perspective: not from the ground, but from space. During the Apollo 8 mission, William Anders captured a photograph of a moment destined to remain etched in humanity’s collective memory. The image, known as "Earthrise," showed our planet suspended in the cosmic void, fragile and beautiful.

"We came all this way to explore the Moon, and the most important thing is that we discovered the Earth." These words summarize the significance of that discovery: it was not just a technological milestone but a new way of seeing ourselves and our planet. Just as Galileo had revolutionized our ability to explore the sky, that photograph forced us to reflect on Earth, its fragility, and the importance of space exploration. Today, with missions aiming to venture even further, all the way to Mars, the knowledge gained from these explorations becomes essential to tackling the engineering challenges of landing and survival on new worlds.

Summary

CHAPTER 1 : INTRODUCTION 10
1.1 Lunar Descent and Landing Systems: From the Early Missions to Today 10
1.2 Landing on Mars: Techniques and Engineering in Recent Missions 11
1.3 Simcenter 3D: Multibody Modeling and FEA 13
CHAPTER 2 : MOON – MARS LANDER 14
2.1 Structure of the lander 14
2.2 Structural Analysis of the Landing Leg System 16
2.2.1 Primary strut 17
2.2.2 Secondary strut 18
2.2.3 Landing footpad 19
2.2.4 Fixing support 19
2.3 Spring 20
2.4 Plascore CrushLite honeycomb damper 20
2.4.1 Configurations of honeycomb 21
CHAPTER 3 : BOUNDARY CONDITIONS 24
3.1 Case Studies 24
3.2 Safety margin 25
3.3 Stabilty index 26
CHAPTER 4 : RIGID BODY SIMULATION 27
4.1 Step file 27
4.2 Motion ambient 27
4.3 Joints 28
4.3.1 Creation of joint on SimCenter 3D 30
4.4 Contacts 31
4.4.1 Creation of 3D Contact on SimCenter 3D 32
4.5 Markers and sensors 33
4.5.1 Creation of marker on SimCenter 3D 33
4.5.2 Creation of sensor on SimCenter 3D 34
4.5.3 Relative velocity 35
4.5.4 Relative displacements – Ks purpose 36
4.5.5 Relative displacements – safety clearance purpose 36
4.6 Loads 36
4.6.1 Creation of load on SimCenter 3D 37
4.6.2 Honeycomb force 39
4.6.3 Anti-pullout force 39
4.7 Step function 40

4.7.1 Creation of step function on SimCenter 3D 40
4.7.2 Step function – Single cartridge honeycomb 42
4.7.3 Step function – Double cartridge honeycomb 42
4.7.4 Step function – Anti pullout force 42
CHAPTER 5 : FLEXIBLE BODY 44
5.1 Creation flexible body 44
5.1.1 FEM Model Creation 44
5.1.2 Mesh Generation 45
5.1.3 Material Assignment 46
5.1.4 RBE2 Constraint Definition 46
5.1.5 Boundary Condition Definition 48
5.1.6 Flexible Body Export 48
5.1.7 Integration into the Motion Simulation 48
CHAPTER 6 : CASE 9 49
6.1 Landing dynamics 49
6.1.1 Initial condition 50
6.1.2 First impact 50
6.1.3 First stabilization 51
6.1.4 Sliding 51
6.1.5 Impact with the rock 52
6.1.6 Overturning 52
6.1.7 Second impact 53
6.1.8 Complete stop 53
6.2 Stability index – Single cartridge 54
6.3 Safety margin – Single cartridge 54
6.4 Crush- box deformation (single cartridge) 55
6.5 Impact loads – single cartridge 56
6.6 Consideration to better understand the graphs 59
6.6.1 Influence of pad orientation on force fluctuations 60
6.6.2 Influence of spring's stiffness on force fluctuations 62
6.7 Stability index – Double cartridge 63
6.8 Safety margin – Double cartridge 63
6.9 Crush-box deformation – double cartridge 64
6.10 Impact loads – double cartridge 65
CHAPTER 7 : CASE 10 67
7.1 Landing dynamics 67
7.1.1 Initial condition 68

7.1.2 First impact 68
7.1.3 Impact of other legs and sliding 69
7.1.4 Impact with the rock 69
7.1.5 Bounce 70
7.1.6 Second impact with the rock 70
7.1.7 Rotation 71
7.2 Crush-box deformation – single cartridge 72
7.3 Impact loads – single cartridge 73
7.4 Crush-box deformation – double cartridge 75
7.5 Impact loads – double cartridge 76
CHAPTER 8 : NEW CASE TEST 78
8.1 Initial condition 78
8.2 Landing's dynamics 78
8.3 Stability index 80
8.4 Impact loads 80
CHAPTER 9 : DOUBLE CARTRIDGE COMPARISON 82
9.1 Crush-box choice 82
9.1 Results 82
9.1.1 TEST 1 83
9.1.2 TEST 2 84
9.1.3 TEST 3 85
9.2 Conclusion 86
CHAPTER 10 : COMPARISON SINGLE AND DOUBLE CARTRIDGE 87
10.1 Comparison: crush-box deformation 87
10.2 Comparison: vertical loads 88
10.3 Comparison: acceleration 88
10.4 Comparison: force at joints 90
10.4.1 Comparison: force at latch 90
10.4.2 Comparison: force at bracket 91
10.5 Comparison overall review 92
CHAPTER 11 : CONCLUSION 93

CHAPTER 1 : INTRODUCTION

In space missions involving the descent of a lander onto the lunar or Martian surface, the landing phase represents one of the most critical and challenging moments from an engineering perspective. To ensure the safety and structural integrity of the module, it is essential to develop accurate models capable of predicting the dynamic behavior of the system during impact.

Building upon activities previously carried out at *Highftech Engineering S.R.L.*, a numerical analysis was developed to simulate the behavior of a deformable element integrated within a shock absorber, which is part of the landing leg of a space exploration module.

The aim of this study is to evaluate the plastic response of the shock absorber under impact conditions, focusing on the assessment of plastic deformations and the analysis of the loads transmitted to the structure during the landing phase.

1.1 Lunar Descent and Landing Systems: From the Early Missions to Today

The Moon has always been a fundamental point of reference for space exploration, both due to its proximity to Earth and the engineering challenges involved in landing. The first human landing occurred in 1969 with NASA's Apollo 11 mission, marking the beginning of an intensive period of technological experimentation and development related to descent and landing on celestial bodies.

For a lander to safely reach the surface, careful trajectory planning and a detailed analysis of the terrain characteristics are required. The entire descent phase is controlled by onboard systems that cooperate with devices such as retrorockets and, in some cases, parachutes, aimed at progressively reducing vertical speed.

At the moment of impact, the accumulated kinetic energy must be managed and dissipated through damping systems, designed to absorb the stresses in extremely short times, thus protecting both the vehicle structure and the payload.

Among the various configurations explored throughout the missions, the one with landing legs has proven to be particularly reliable. This configuration has been used in both robotic missions, such as Surveyor, and crewed missions, such as those of the Apollo program [1], Figure 1.

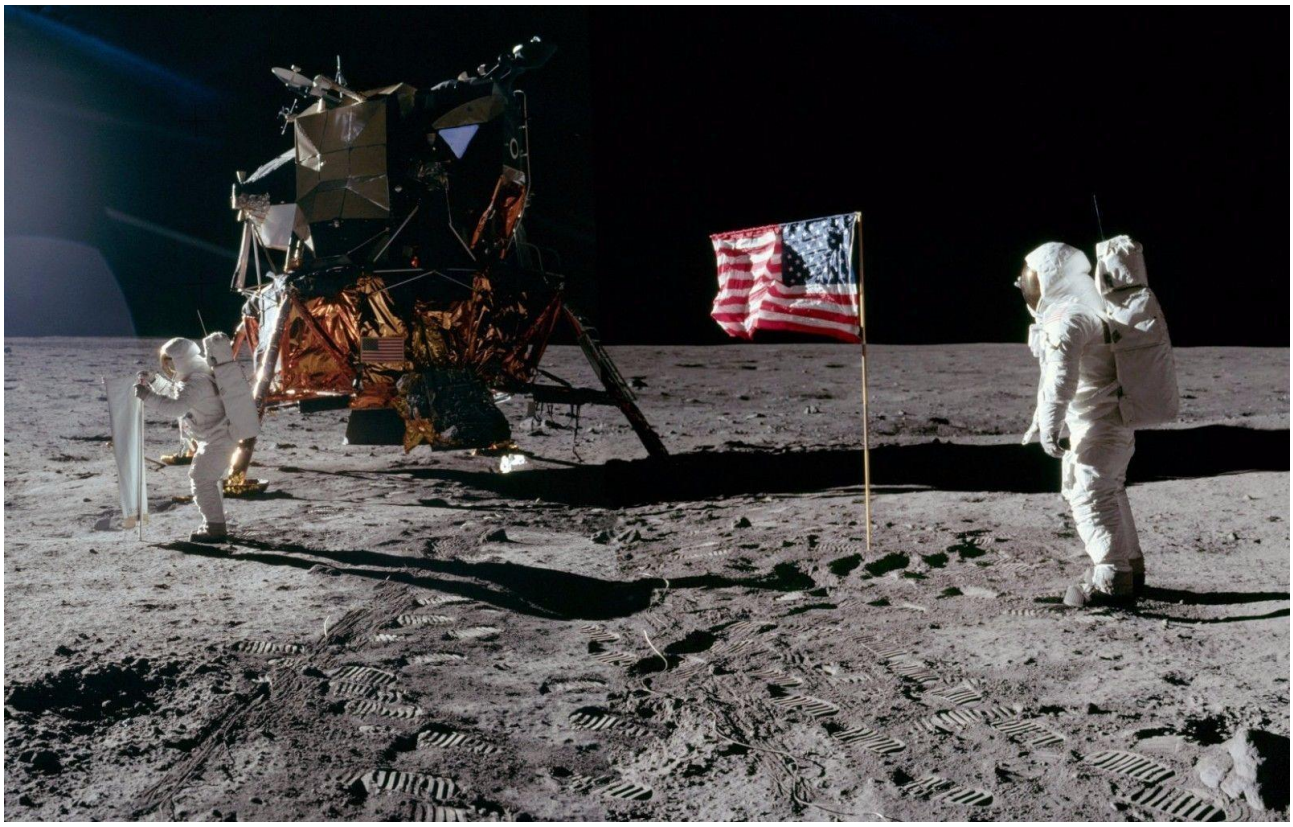


Figure 1: Apollo 11 Lunar Module on the Lunar Surface

1.2 Landing on Mars: Techniques and Engineering in Recent Missions

Mars, the Red Planet, has generated growing scientific and engineering interest since the early years of space exploration, due to its similarity to Earth and the potential to study its geology and atmospheric conditions. The first missions to the Red Planet were launched in the 1960s, but it was not until the 1970s that space agencies succeeded in achieving controlled landings and transmissions from the surface. The most notable of these was Viking 1, which in 1976 became the first lander to operate successfully on Mars, studying the atmosphere and soil composition.

Over the decades, NASA, along with other space agencies, has refined descent and landing technologies for Mars, addressing the challenges posed by its thin atmosphere, the presence of dust, and the difficulty of precisely determining position and velocity during landing. Unlike the Moon, Mars has an atmospheric density that allows the use of parachutes, but not as efficiently, as the atmosphere is too thin to provide optimal deceleration during the final descent phases. This has led

to the adoption of innovative engineering solutions such as retrorockets and "sky-cranes," technologies that enabled recent missions, such as Curiosity in 2012 and Perseverance in 2021, to land successfully.

A critical phase of every Mars mission is accurate terrain mapping and the design of a precise descent trajectory. The main difficulty lies in adapting to the variability of atmospheric conditions and terrain, which may present unforeseen obstacles. Landing systems must therefore be extremely responsive and adaptable, with the capability to correct the trajectory during descent.

Additionally, just like on the Moon, during the landing on Mars, the lander must dissipate the accumulated kinetic energy rapidly to avoid damage to both the module's structure and the payload. Impact forces must be effectively absorbed by damping systems, which reduce the risk of damage to sensitive components such as scientific instruments.

The configurations of Mars landers, such as those used in the Viking, Spirit, Opportunity, Curiosity, and Perseverance missions, have employed various solutions, including landing legs, advanced parachute systems, and rocket structures to slow down the landing, always with the goal of ensuring minimal impact and optimal safety for the precious instruments onboard.

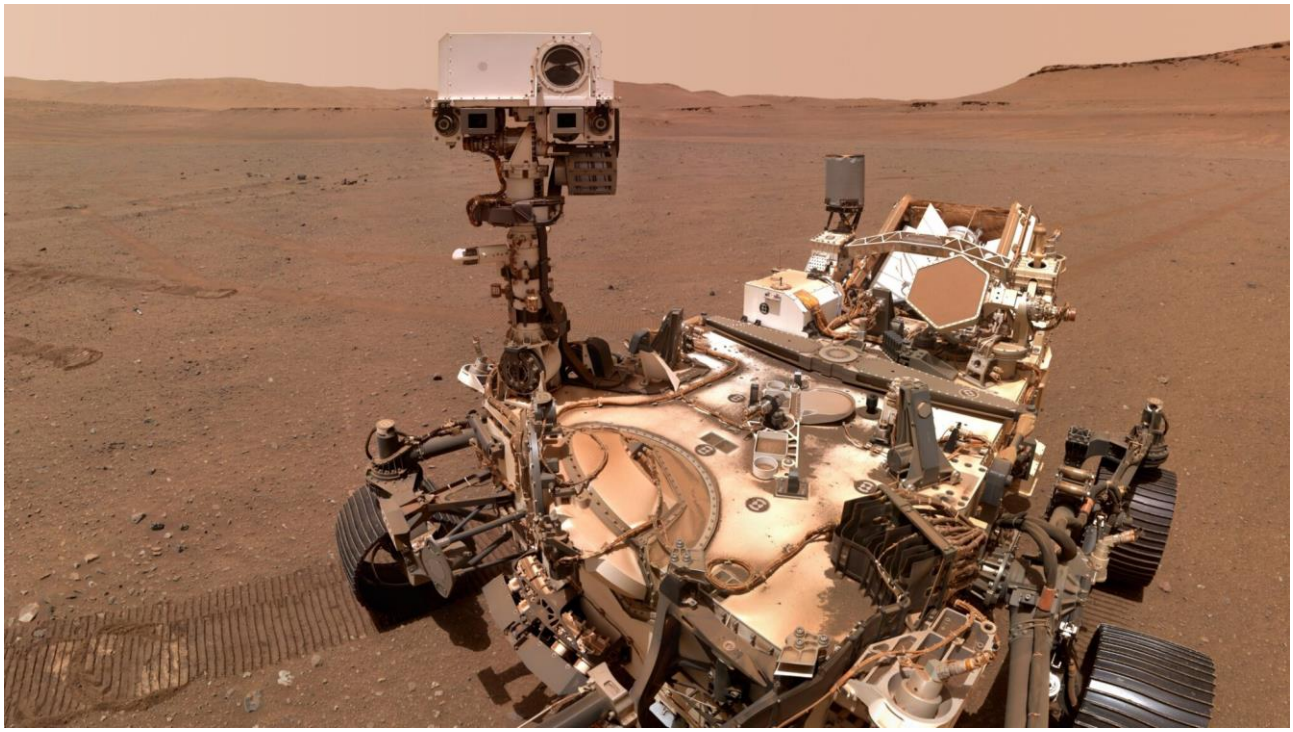


Figure 2: Perseverance Rover Conducting Soil Sampling on the Martian Surface

1.3 Simcenter 3D: Multibody Modeling and FEA

Simcenter 3D is an advanced simulation software used for multibody dynamics (MBD) and finite element analysis (FEA). It enables engineers to create digital models of complex systems with multiple interacting bodies, which is crucial for understanding dynamic behavior in systems like vehicles, machinery, and aerospace components. The software supports both rigid and flexible body modeling, allowing for precise simulations of how components move and interact under various conditions.

For FEA, Simcenter 3D offers tools for structural, thermal, and vibrational analysis, helping engineers to assess stress, deformation, and thermal behavior. By integrating MBD and FEA, the software provides comprehensive insights into product performance, reducing the need for physical prototypes and enabling more efficient design optimization. This combination helps streamline the product development process, improving accuracy, performance, and time-to-market.

CHAPTER 2 : MOON – MARS LANDER

2.1 Structure of the lander

A lander is typically equipped with a comprehensive suite of instruments, technologies, and materials essential for conducting scientific operations on extraterrestrial surfaces. One of the most critical components is the deployment of robotic rovers, which are capable of traversing the terrain, collecting geological samples, and performing on-site experiments. To support these activities, the lander carries specialized sensors and devices designed to analyze soil composition, monitor environmental conditions, and detect phenomena such as cosmic radiation. It may also include tools for extracting and storing samples of regolith, rocks, or other materials for later analysis, potentially back on Earth. In some mission architectures, propellant reserves are included to enable ascent from the planetary surface or to perform controlled maneuvers. Communication systems, comprised of antennas and high-frequency transmitters, ensure the continuous relay of data between the lander and Earth-based mission control. Power generation and thermal management are handled by solar panels, rechargeable batteries, and active temperature regulation systems, which collectively maintain operational stability in harsh and variable environments. Precise landing is made possible through autonomous navigation technologies and descent systems equipped with sensors and controlled thrusters, ensuring a safe and accurate touchdown. The integration of these systems underscores the complexity and engineering precision required for successful planetary exploration missions.

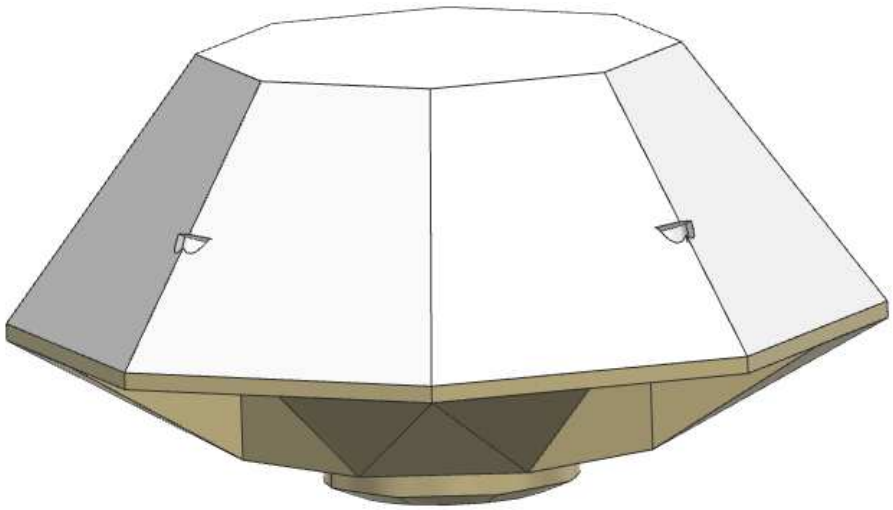


Figure 3: Lateral view of the MML

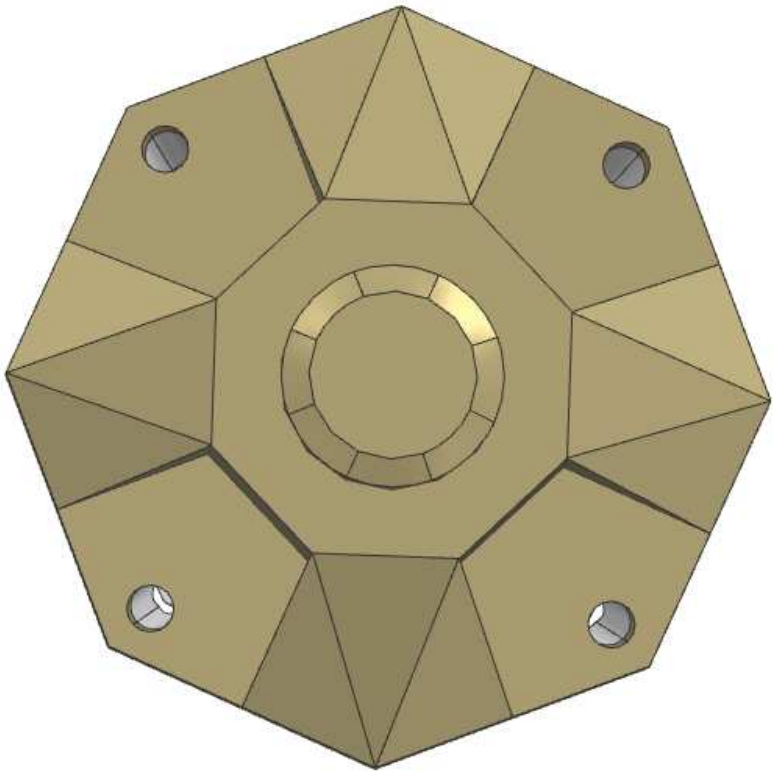


Figure 4: Inferior view of the MML

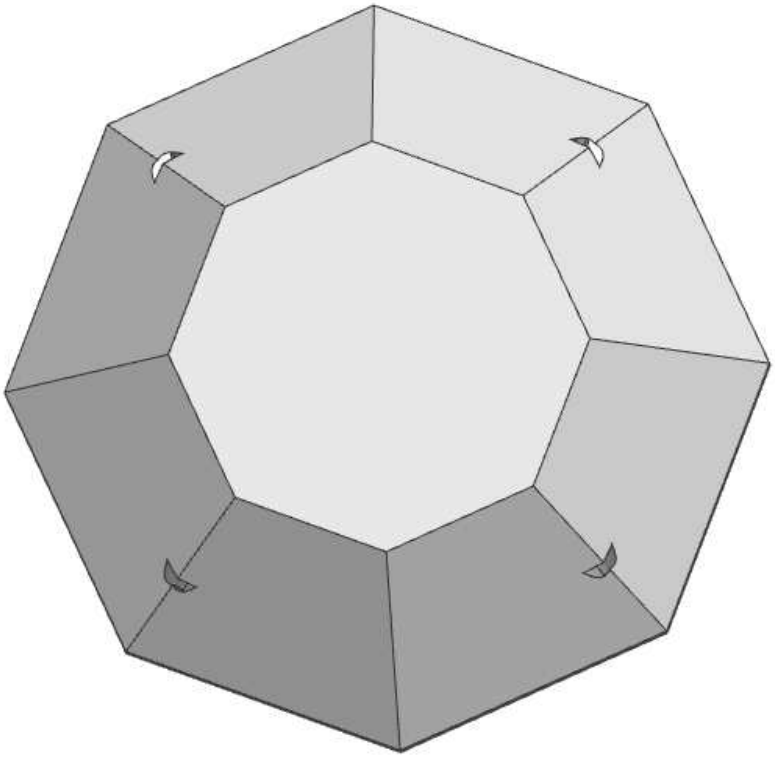


Figure 5: Superior view of the MML

2.2 Structural Analysis of the Landing Leg System

The landing leg system consists of four distinct components, each made from different materials selected according to their specific structural and functional roles. A structural analysis is necessary to assess the strength and stability of the system under operational loads. Figure [5] [6] below shows the complete structure, including all four components.



Figure 6: Lateral view of the leg

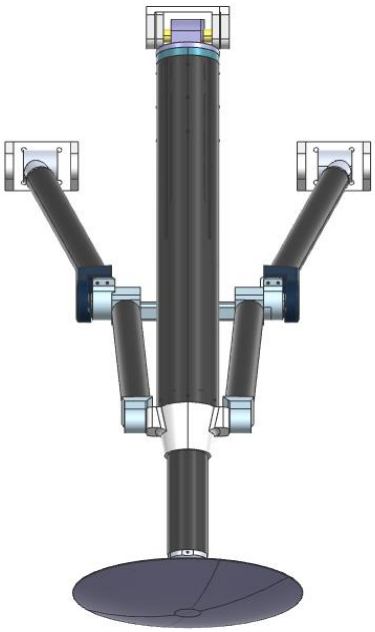


Figure 7: Front view of the leg

2.2.1 Primary strut

The *primary strut* is a telescopic leg composed of two carbon fiber reinforced polymer (CFRP) tubes, referred to as Tube A and Tube B. It is connected to the MML through dedicated fixing supports, as illustrated in Figure [6] [7]. Housed within this main structural element is an aluminum honeycomb damper.

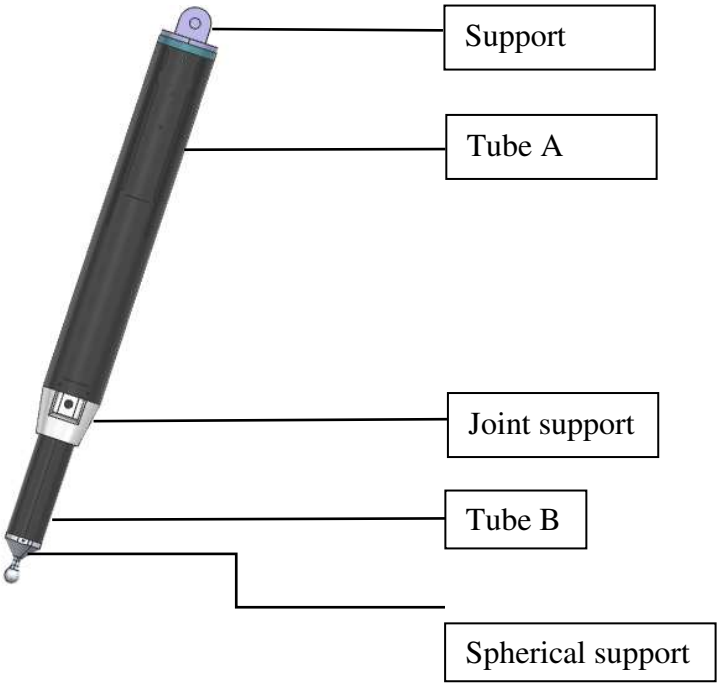


Figure 8: External view of the primary strut

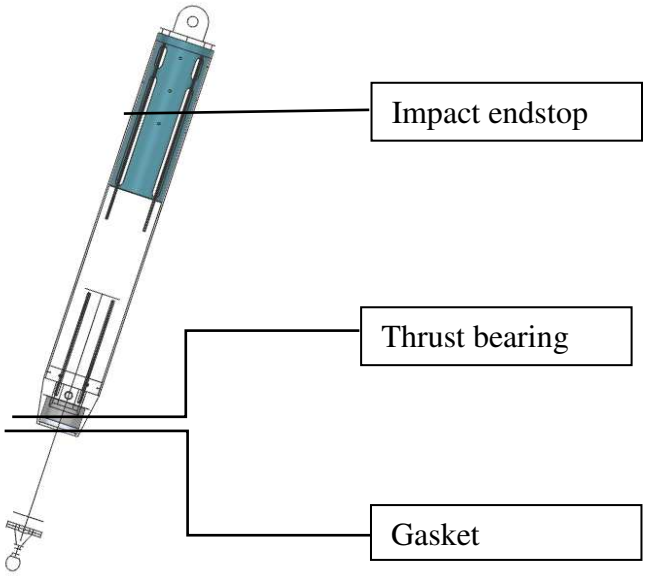


Figure 9: Internal view of the primary strut

2.2.2 Secondary strut

The *secondary strut* consists of two quadrilateral linkages connected to the primary structure and anchored to the central body through fixing supports, as shown in Figure [8]. This mechanism plays a key role in both deploying the landing system and securing it in its fully extended configuration.

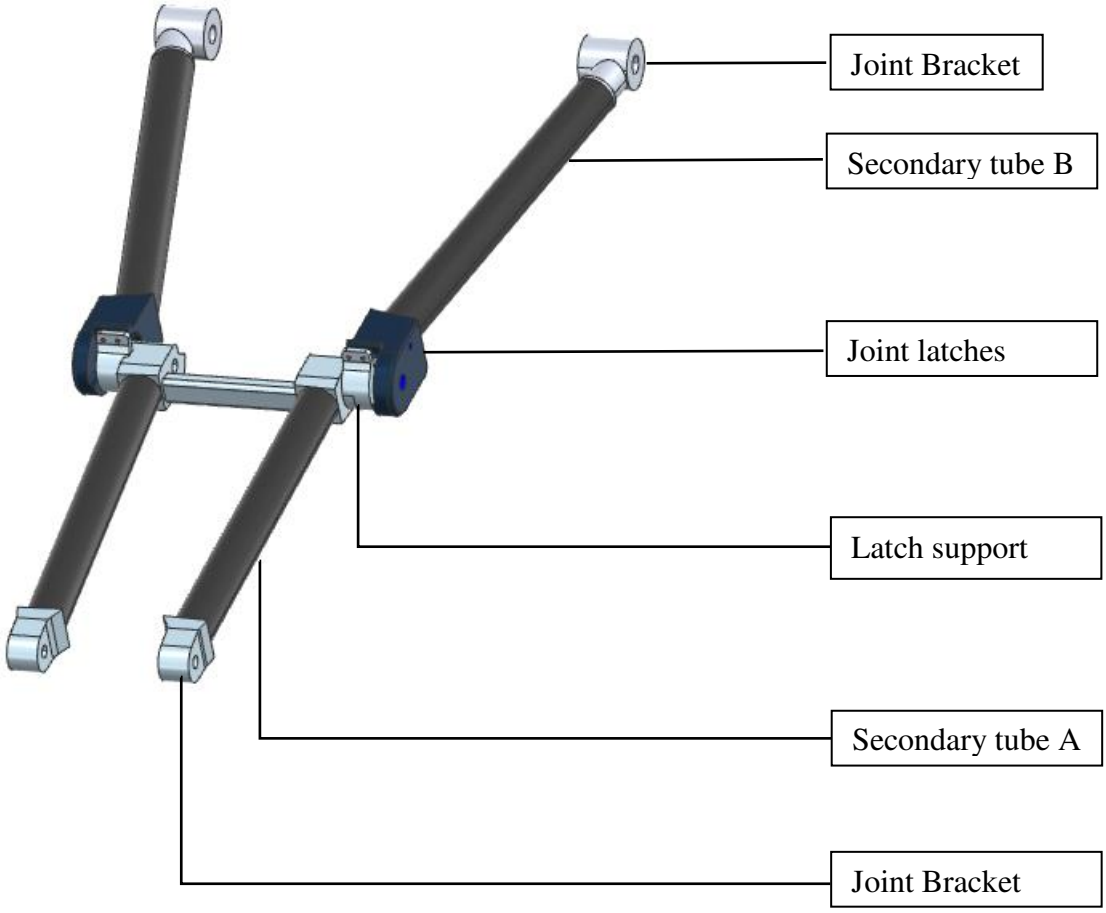


Figure 10: Secondary strut

2.2.3 Landing footpad

The *landing footpad* serves as the ground contact interface and is attached to Tube B of the primary structure via a spherical joint, as illustrated in Figure [9].

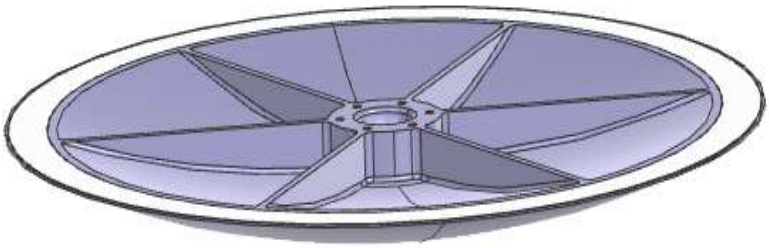


Figure 11: Landing footpad

2.2.4 Fixing support

The *fixing supports* connect the landing leg structure to the central body of the module, as shown in Figure 9. Specifically, the two brackets on the right are mounted to the lander's platform, while the Fixing Support on the left is attached directly to the central body.

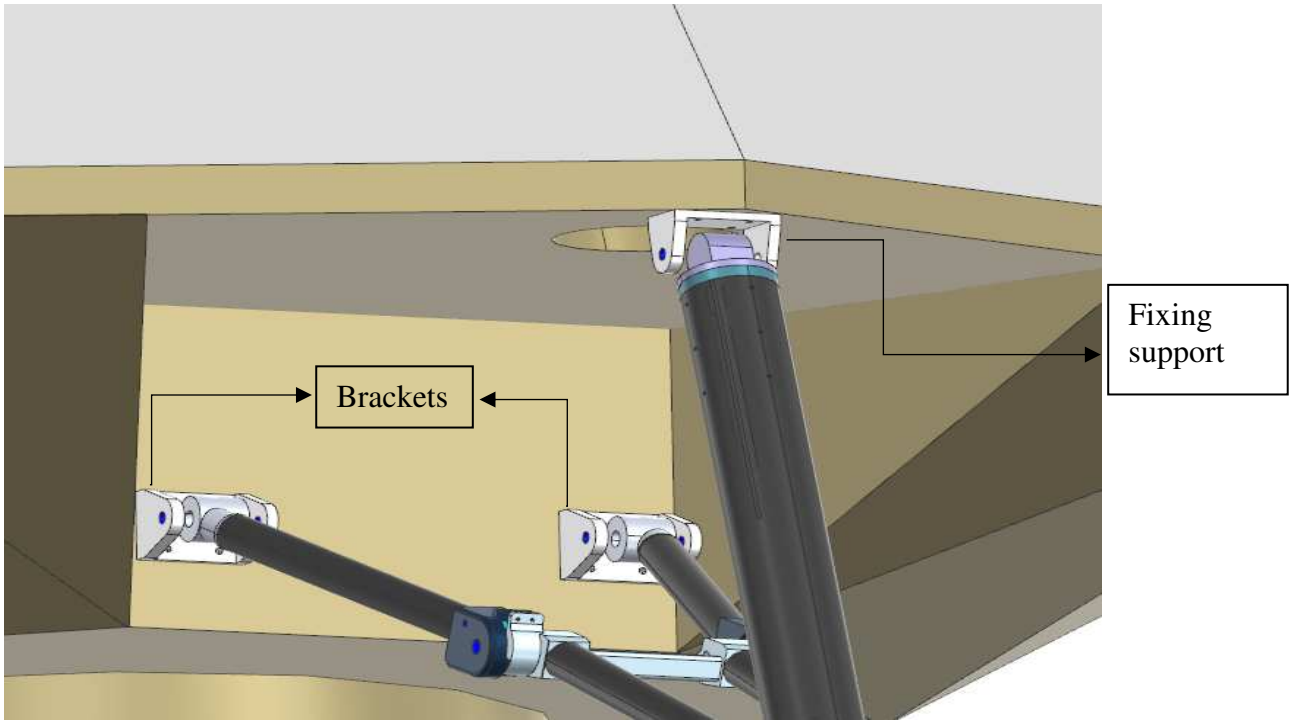


Figure 12: Brackets and fixing support

2.3 Spring

For each pad, four springs are used in order to ensure a certain stability of the footpad, preventing incorrect movement during the landing. Each spring has a value of stiffness in the order of 100 N/mm

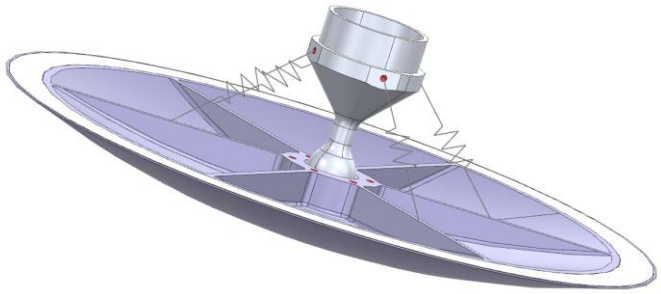


Figure 13: Representation of four springs on the software view

2.4 Plascore CrushLite honeycomb damper

Plascore CrushLite is a lightweight aluminum honeycomb material specifically engineered to provide controlled crush resistance for energy absorption applications. Its honeycomb architecture enables it to deliver a nearly constant force response during compression, ensuring consistent and reliable energy dissipation. This makes it particularly suitable for scenarios requiring impact mitigation or protection against external loads, such as in the automotive, aerospace, and high-performance packaging industries [11].



Figure 14 : Plascore CrushLite honeycomb damper

In the figure [12] below, the honeycomb damper is represented in the CAD model as a cylindrical component. It is important to note, however, that this cylindrical geometry is used solely for CAD representation purposes. In the subsequent rigid and flexible body simulations, the damper will not be modeled as a physical structure but instead will be represented through equivalent forces acting between Tube B and the impact endstop.



Figure 15 : Honeycomb damper representation

2.4.1 Configurations of honeycomb

In this study, two different energy-absorbing designs were evaluated and compared:

- A single-cartridge crush-box (HIGH-STRENGTH)
- A dual-cartridge crush-box (LOW-STRENGTH / HIGH-STRENGTH)

The dual-cartridge honeycomb configuration is widely adopted for soft landing applications due to its multiple functional benefits:

- The softer cartridge enhances resistance to tipping by improving stability.
- The stiffer cartridge prevents the complete collapse of the crush structure, thereby safeguarding the overall system by limiting transmitted loads.

Moreover, this dual-layered design contributes to a reduction in peak accelerations experienced by the payload during impact events . The figure below presents the typical load–displacement response of a dual-cartridge crush-box. The energy dissipated during compression corresponds to the area beneath this curve.

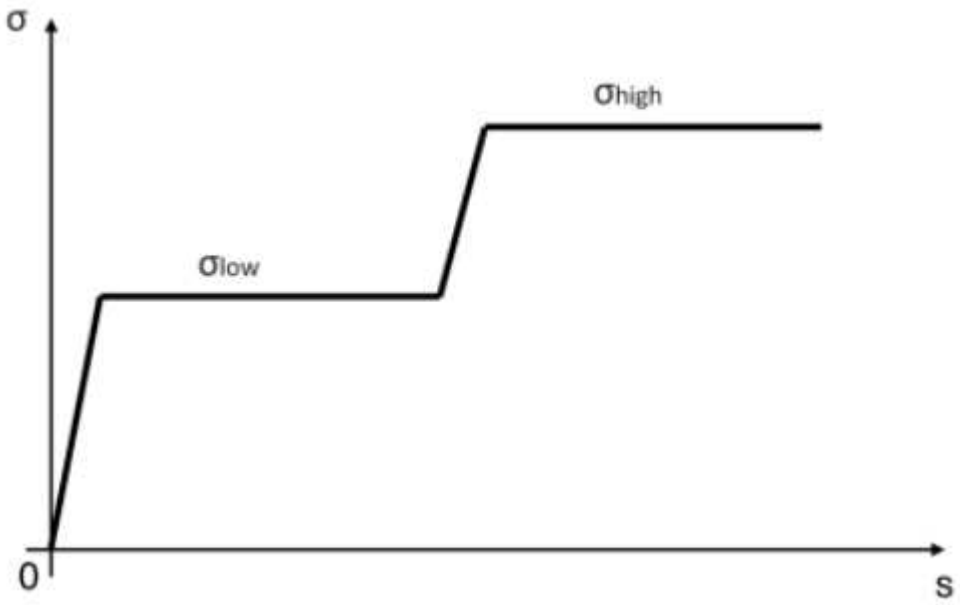


Figure 16 : Double-cartridge crush-box behaviour

During this study, the crush-box is modelled directly using its deformable part, so the 70% of the total length. The characteristics are:

Feature	**Value**	**Description**
$D_{CRUSH-BOX}$	83 mm	External diameter
$d_{CRUSH-BOX}$	24 mm	Internal diameter
$A_{CRUSH-BOX}$	4958.2 mm^2	Area of the section
L	198.8 mm	Length of the crush-box
σ	5.17 MPa	Resistance of the crush-box

Table 1: Single cartridge crush-box data

Feature	**Value**	**Description**
$D_{CRUSH-BOX}$	83 mm	External diameter
$d_{CRUSH-BOX}$	24 mm	Internal diameter
$A_{CRUSH-BOX}$	4958.2 mm^2	Area of the section
L_{HIGH}	130.5 mm	Length HIGH-STRENGHT crush-box
L_{LOW}	68.3 mm	Length LOW-STRENGHT crush-box
σ_{HIGH}	5.17 MPa	Resistance LOW-STRENGHT crush-box
σ_{LOW}	3.69 MPa	Resistance HIGH-STRENGHT crush-box

Table 2: Double cartridge crush-box data

CHAPTER 3 : BOUNDARY CONDITIONS

This chapter provides a detailed description of the boundary conditions applied to the simulations, along with preliminary considerations for the multibody dynamics (MBD) analysis. All simulations are based on the expected environmental and landing conditions for a Mars exploration mission. Accordingly, parameters such as gravitational acceleration, soil stiffness coefficients, and damping factors are defined according to the Martian environment. Specifically, the gravitational acceleration on Mars is approximately 3.721 m/s².

3.1 Case Studies

Table [3] below presents all the possible landing scenarios initially considered in the rigid body model simulations. Cases 9 and 10 will be analyzed and simulated in detail, as they represent the most critical scenarios.

Scenario	1	2	3	4	5	6	7	8	9	10
Slope (degrees)	0	15	15	15	15	15	15	15	15	15
Friction	0	0	0	0	0.5	0.5	0.5	0.5	0.5	0.5
Velocity along Z [m/s]	-2.5	-2.5	-2.5	-2.5	-2.5	-2.5	-2.5	-2.5	-2.5	-2.5
Velocity along X [m/s]	0	0	0	-2	-2	-2	-2	-2	-2	-2
Inclination MML (degree)	0	0	8.5	8.5	0	0	8.5	0	0	0
N. Leg initial contact	4	2	2	2	2	2	2	1	1	1
Obstacle	no	no	no	no	no	yes	yes	no	yes	yes

Table 3: Data of case studies

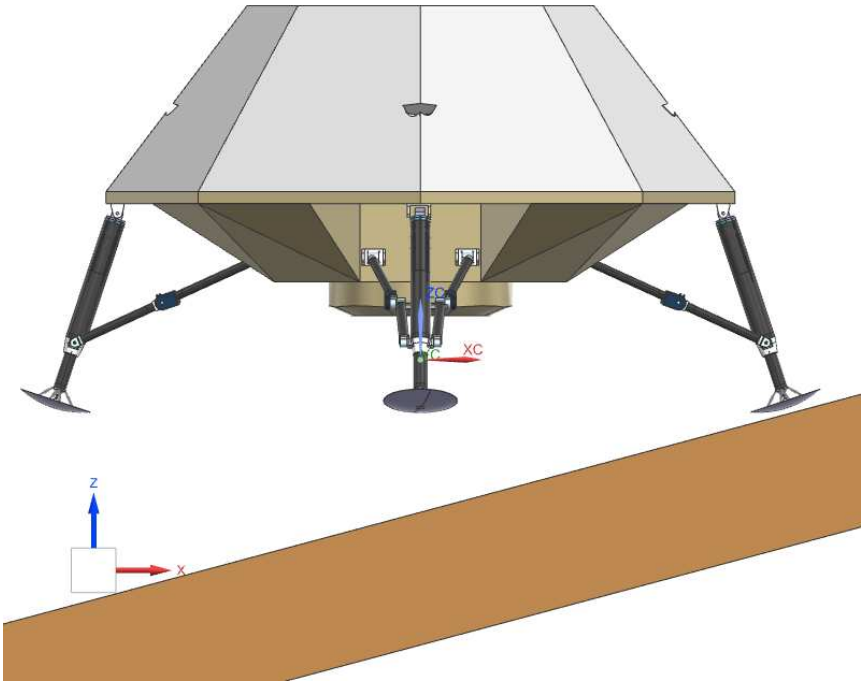


Figure 17 : Axis orientation

3.2 Safety margin

One of the main objectives of this thesis is to assess the safety margin for protecting the Secondary Strut. During the landing impact, it is crucial to prevent any collision between the secondary structure and potential obstacles, such as rocks, as shown in Figure 15. Such an impact would be catastrophic, as the primary structure alone would not be able to withstand frontal or lateral loads.

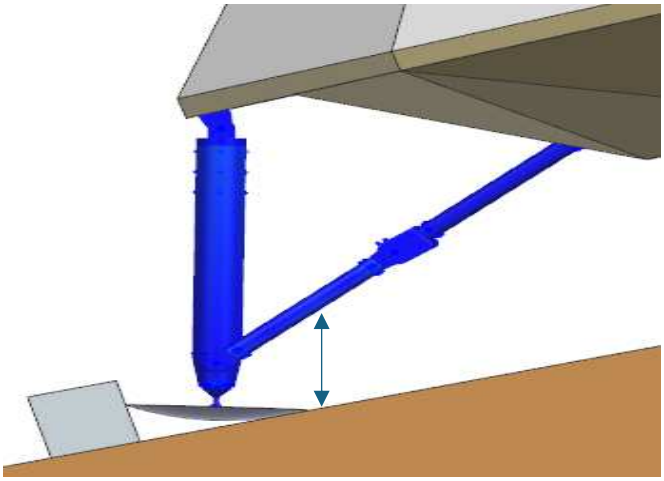


Figure 18 : Safety margin

3.3 Stabilty index

The stability index Ks was computed in the simulations to assess the worst-case scenario in terms of tipping risk. The corresponding values can be inferred from Figure . The Lander is considered stable when $Ks \geq 1.5$.

$$K_s = \frac{H_i - H_m}{H - H_m}$$

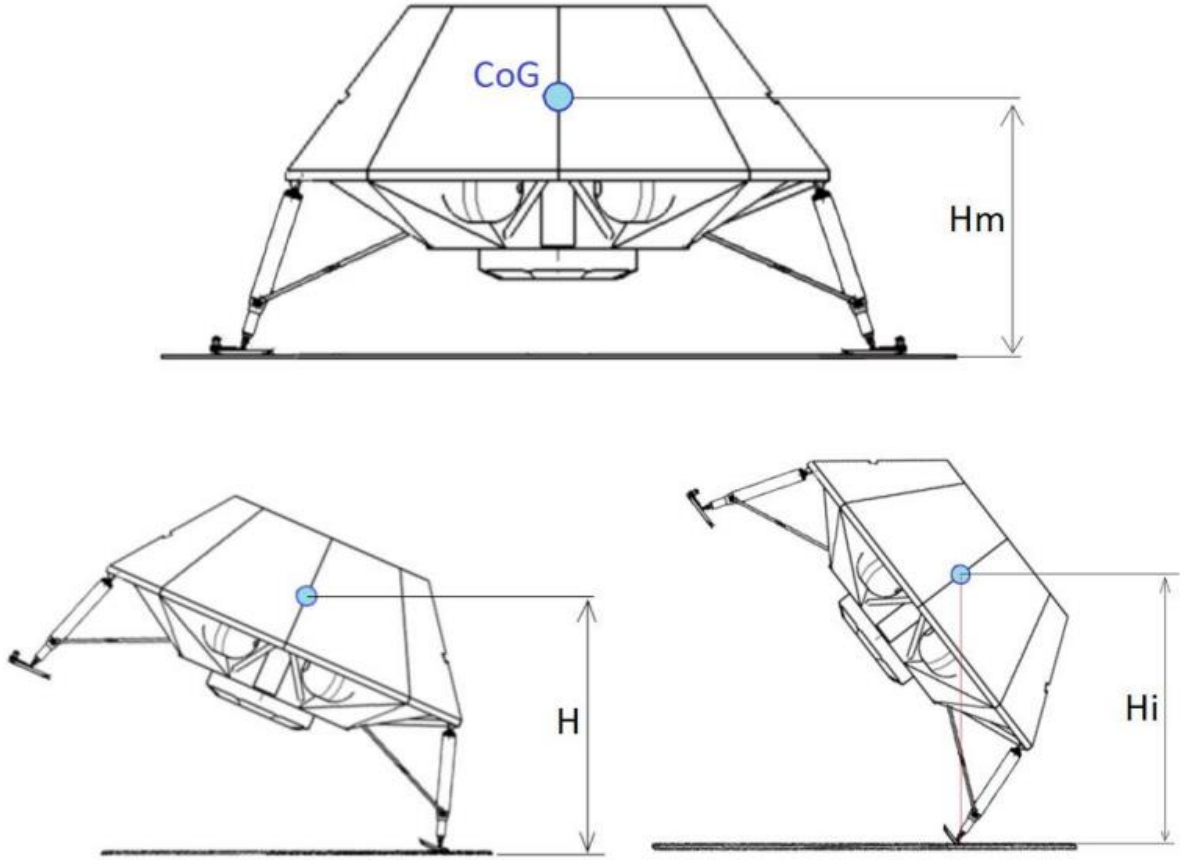


Figure 19: stability index references

- Hm represents the height from ground of the center of gravity
- Hi refers to the condition of incipient overturning (CoG aligned with the support pad)
- H represents the condition reached during the generic simulation, it is the only value of the three that is extrapolated from the individual simulation

CHAPTER 4 : RIGID BODY SIMULATION

4.1 Step file

The first action was to import the *.stp* file, which contains the complete lander model, into the *modeling* environment of Simcenter 3D.

4.2 Motion ambient

Subsequently, the model was transferred to the motion environment within Simcenter 3D. Initially, each component of the model was defined as a "Motion Body." Within this environment, the mass, center of mass, and center of gravity of each part are displayed. The mass calculations were made based on the materials assigned to each individual component, as detailed in the table [2] below.

Part	Material
Support	*Ti6Al4V*
Impact Endstop	*AA7075 T651*
Primary Tube A	*CFRP*
Joint Support	*Ti6Al4V*
Primary Tube B	*CFRP*
Joint Brackets B	*Ti6Al4V*
Secondary Tubes B	*CFRP*
Latch	*Ti6Al4V*
Secondary Tubes A	*CFRP*
Joint Latches	*Ti6Al4V*
Joint Brackets A	*Ti6Al4V*
Spherical Joint	*Ti6Al4V*
Footpad	*AA7075 T651*
Fixing Support	*Ti6Al4V*
Brackets	*Ti6Al4V*
Thrust bearing	-
Gasket	-

Table 4: material of the parts

4.3 Joints

In Simcenter 3D, joints are employed to define the mechanical connections between rigid bodies within the landing leg system, accurately representing the physical constraints and degrees of freedom in the actual assembly. The specific joints utilized in the model are detailed in the table [3] below.

Label	Body 1	Body 2	Connection type
1	Footpad	Spherical Support	*Spherical joint*
2	Spherical Support	Tube B	*Fixed*
3	Tube B	Tube A	*Translational joint*
4	Tube B	Joint Support	*Translational joint*
5	Tube A	Impact Endstop	*Fixed*
6	Impact Endstop	Support	*Fixed*
7	Support	Fixing Support	*Revolute joint*
8	Fixing Support	MML	*Fixed*
9	Right Bracket	MML	*Fixed*
10	Left Bracket	MML	*Fixed*
11	Joint Support	Tube A	*Fixed*
12	Joint Support	Right Joint Bracket A	*Revolute joint*
13	Joint Support	Left Joint Bracket A	*Revolute joint*
14	Right Joint Bracket A	Right Tube A	*Fixed*
15	Left Joint Bracket A	Left Tube A	*Fixed*
16	Right Tube A	Latch Support	*Fixed*
17	Left Tube A	Latch Support	*Fixed*
18	Latch Support	Right Joint Latch	*Revolute joint*
19	Latch Support	Left Joint Latch	*Revolute joint*
20	Right Joint Latch	Right Tube B	*Fixed*
21	Left Joint Latch	Left Tube B	*Fixed*
22	Right Tube B	Right Joint Bracket B	*Fixed*
23	Left Tube B	Left Joint Bracket B	*Fixed*
24	Right Joint Bracket B	Right Bracket	*Revolute joint*
25	Left Joint Bracket B	Left Bracket	*Revolute joint*

Table 5 : joints involved

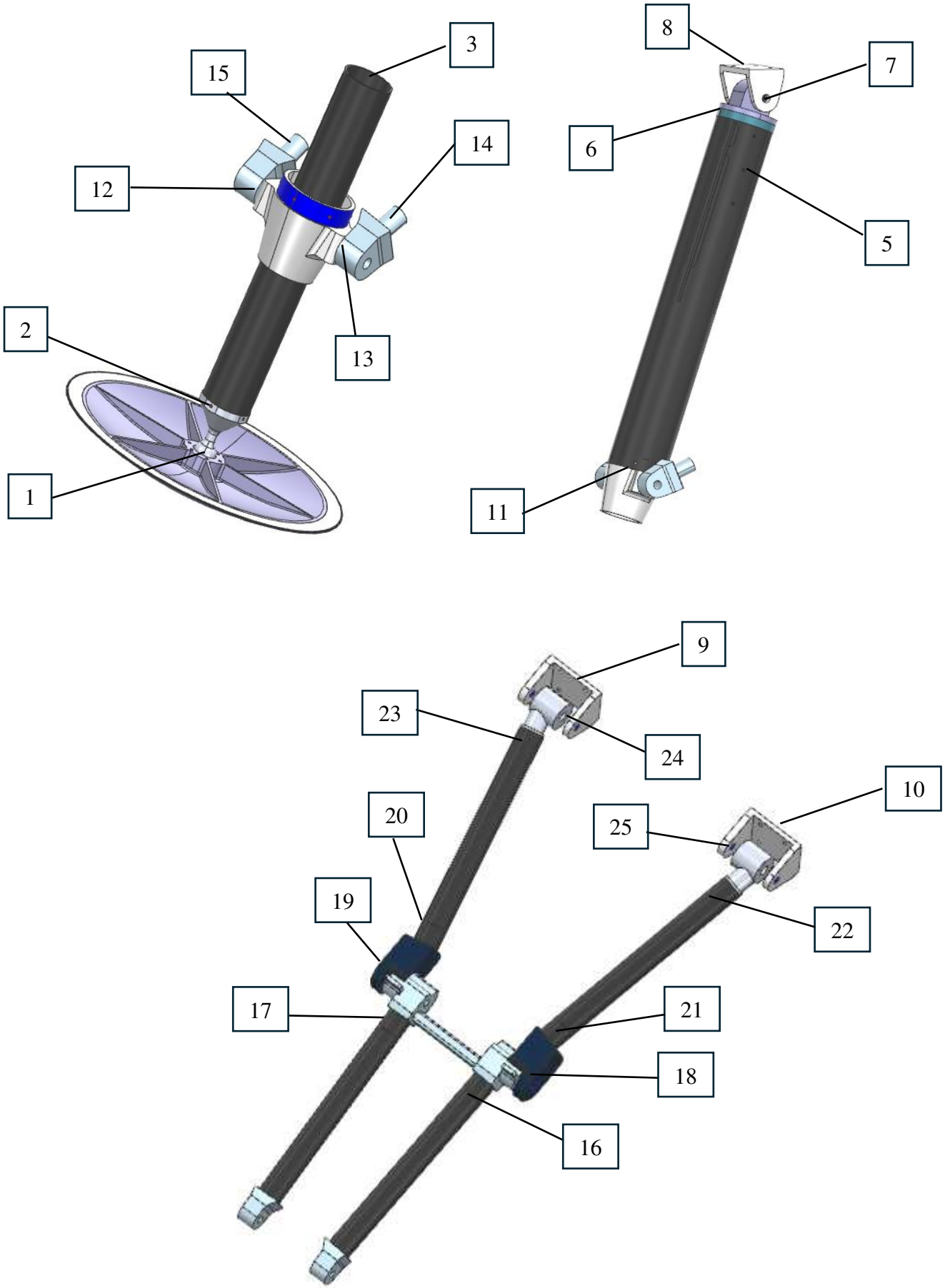


Figure 20: joints positioning

Some of the joints included in the model are not unique but multiple, as they are intended to simulate the connection between two parts using bolts. The table below shows the number of bolts used for these types of connections

Label	Body 1	Body 2	N° bolts
2	Spherical Support	Tube B	4
5	Tube A	Impact Endstop	12
6	Impact Endstop	Support	8
11	Joint Support	Tube A	6
14/15	Right/Left Joint Bracket A	Right/Left Tube A	4
16/17	Right/Left Tube A	Latch Support	4
20/21	Right/Left Joint Latch	Right/Left Tube B	4
22/23	Right/Left Tube B	Right/Left Joint Bracket B	4

Table 6 : number of bolts involved for joint

4.3.1 Creation of joint on SimCenter 3D

In this paragraph, one can see step by step, the way in which one can create a joint in the software.



Figure 21: joint position in the menu

In the figure below, one can see the main setting that one have to set in order to create a joint.

- Type: various types of joints are available, some of which correspond to physical joints in reality, such as universal joints and spherical joints, and others that offer detailed control over specific degrees of freedom.

- Select Motion Body: one has to select the one of the two bodies that can move

- Specify Origin: one has to select the point of origin of the joint

- Specify Vector: one has to select the vector along which the joint has to work

- Select Motion Body : one has to select the one of the two bodies that remain in quiet

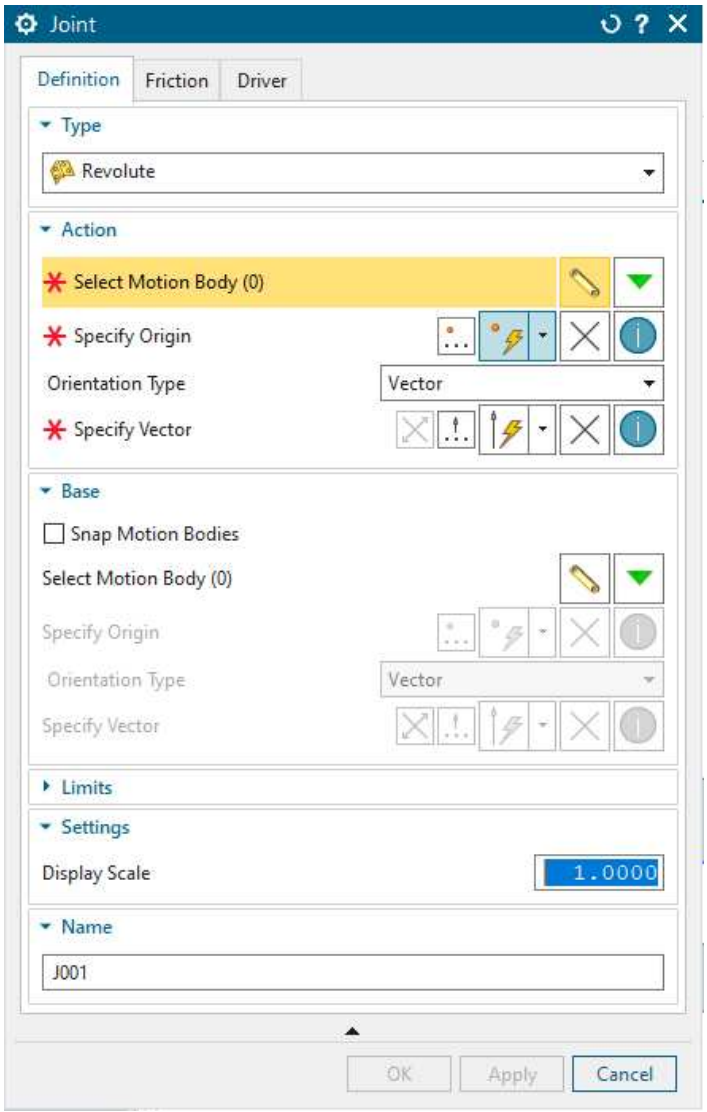


Figure 22: joint setting

4.4 Contacts

The *3D Contact* feature is used to model contact interactions between solid bodies within the motion simulation. This method generates a contact force whenever two motion bodies come into contact during the analysis. For contact purposes, each motion body is treated as a single solid, and the resulting contact force is based on the overlapping volume caused by penetration. Contacts are

used between the various pad and the soil. The data in the table below are representative of the Martian soil [1]

Stiffness	48800 N/mm
Force Exponent	3.43
Material Damping	360 N*s/mm
Max Penetration Depth	0.1
FRICTION DATA	
Static Coefficient	0.5
Striction Velocity	100 mm/s
Dynamic Coefficient	0.41
Friction Velocity	1000 mm/s

Table 7 : values utilized to represent Martian soil

4.4.1 Creation of 3D Contact on SimCenter 3D

In this paragraph, one can see step by step, the way in which one can create a contact in the software.

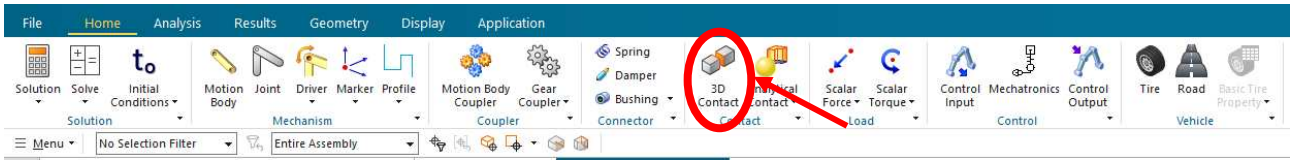


Figure 23 : 3D Contact position in the menu

For this purpose, one has to select the type “CAD Contact” since one wants to simulate the contact between two bodies. Then, one has to select the two bodies, respectively the action and the base body and in the end the various parameters of the contact

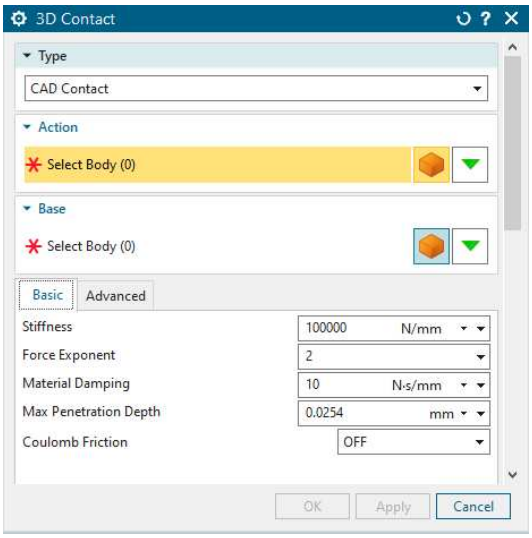


Figure 24 : 3D Contact Setting

4.5 Markers and sensors

In the motion model, *markers* were employed to identify specific points of interest on the motion bodies. A marker is a local coordinate system defined at a particular location on a body, serving as a reference for subsequent operations. *Sensors* were implemented to capture data regarding the relative motion or the relative displacements between specific points of interest.

4.5.1 Creation of marker on SimCenter 3D

In this paragraph, one can see step by step, the way in which one can create a marker in the software.



Figure 25: marker position in the menu

In the menu of the marker, one has to select the body in which one wants to fix a point to measure. Than, one has to specify the coordinates of the point that want to measure and its coordinate system

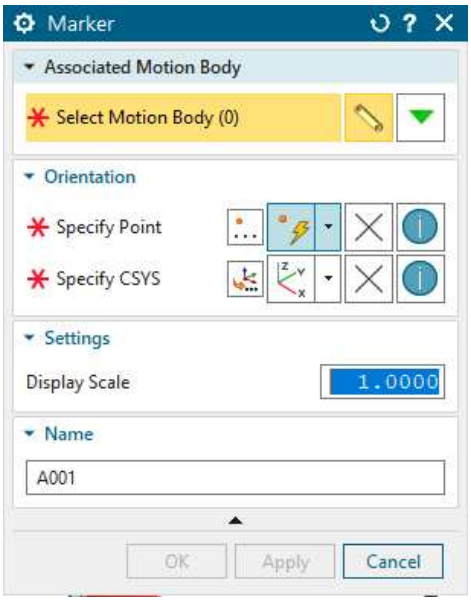


Figure 26: marker setting

4.5.2 Creation of sensor on SimCenter 3D

In this paragraph, one can see step by step, the way in which one can create a sensor in the software.

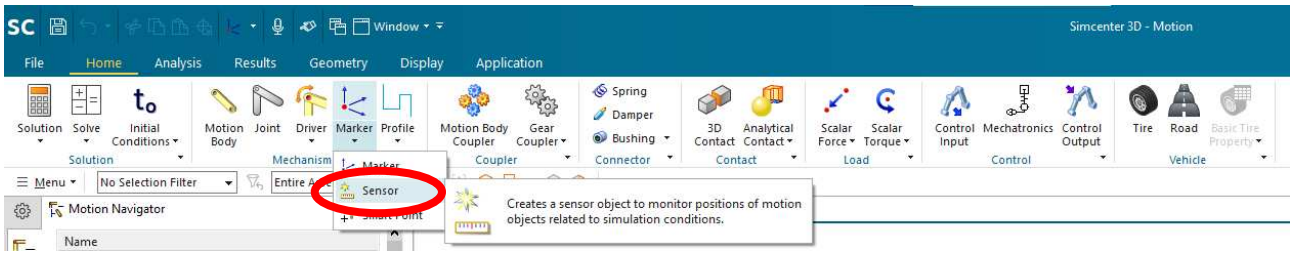


Figure 27: sensor position in the menu

There are various type of sensor that one can use in this software. For this purpose, one has utilized the “Displacement sensor” and the “Velocity sensor”. Once specified the component, that for this purpose is “Linear Magnitude”, one has select in the Reference Frame “Relative” since one wants to study a certain parameter between two bodies. In the end, in Measurement and Relative one has to select the two markers previously created.

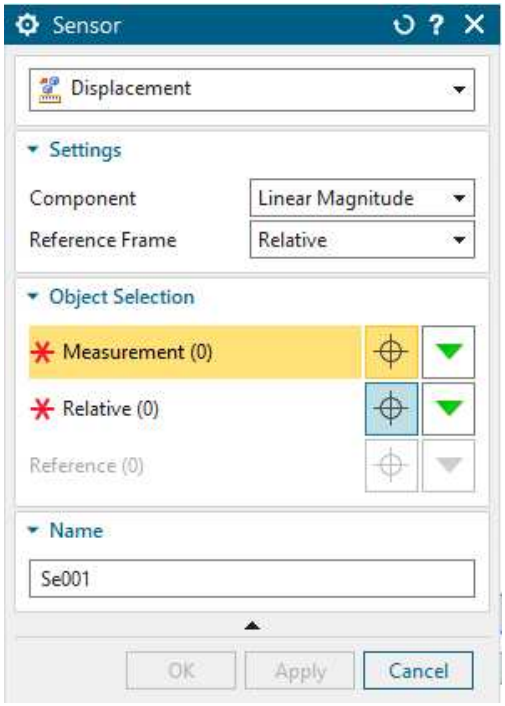


Figure 28: sensor setting

4.5.3 Relative velocity

As one can see in the figures below, markers were placed on Tube B and on the impact endstop. A sensor was used to measure the relative velocity along the Z-axis between the two markers placed on Tube B and the impact endstop. This measurement serves as a triggering condition for the application of the contact force. Specifically, a negative relative velocity between the two markers would indicate that, in a real scenario, the honeycomb damper is undergoing compression.



Figure 29 : Marker on tube B



Figure 30 : Marker on Impact Endstop

4.5.4 Relative displacements – Ks purpose

As mentioned in the past paragraph, a measure of the parameter “H” is necessary. For this purpose, a marker is placed in the COG of the lander and another in correspondence of the axis that pass thought the lowest point of the pad in contact with the land

4.5.5 Relative displacements – safety clearance purpose

One of the purposes of the simulations, is to ensure that the structure of the lander, once it land on the planet, does not hurt with some obstacles like a rock. To do this, one has chosen a limit value of 200 mm (that represent the height of a rock), beyond which a safety landing is not ensured. A marker is applied on the tube B of the leg 3, the most critical leg in terms of lowering, and another on the soil.

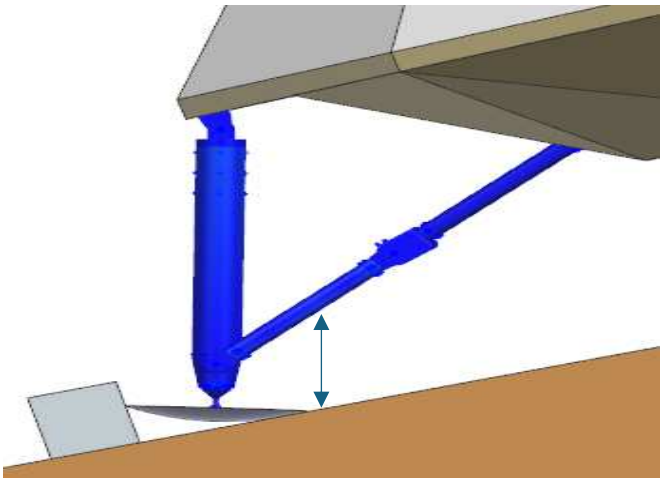


Figure 31: safety clearance

4.6 Loads

The *Loads* command in Simcenter 3D allows the definition and application of loading conditions to simulation models. Through this tool, forces, pressures, moments, and other external conditions can be assigned that influence the structural or thermal behavior of the analyzed elements, enabling precise simulation of the stresses to which the system is subjected. In our study, *Loads* were employed to simulate forces between relative components.

4.6.1 Creation of load on SimCenter 3D

In this paragraph, one can see step by step, the way in which one can create a contact in the software.

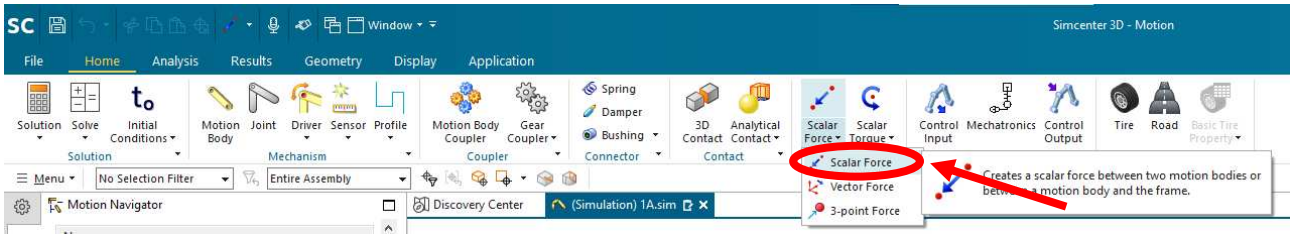


Figure 32: load position in the menu

As one can see in the figure below, one has to select first the direction along the force has to act. Then, one has to choose if the force is action-reaction or only action (as the case of this thesis). As the previously setting, one has to select the action and base body with the relative point of acting. In the end, one has to choose the type of force (in this thesis is a constant force, so one has selected “Expression”) and its value

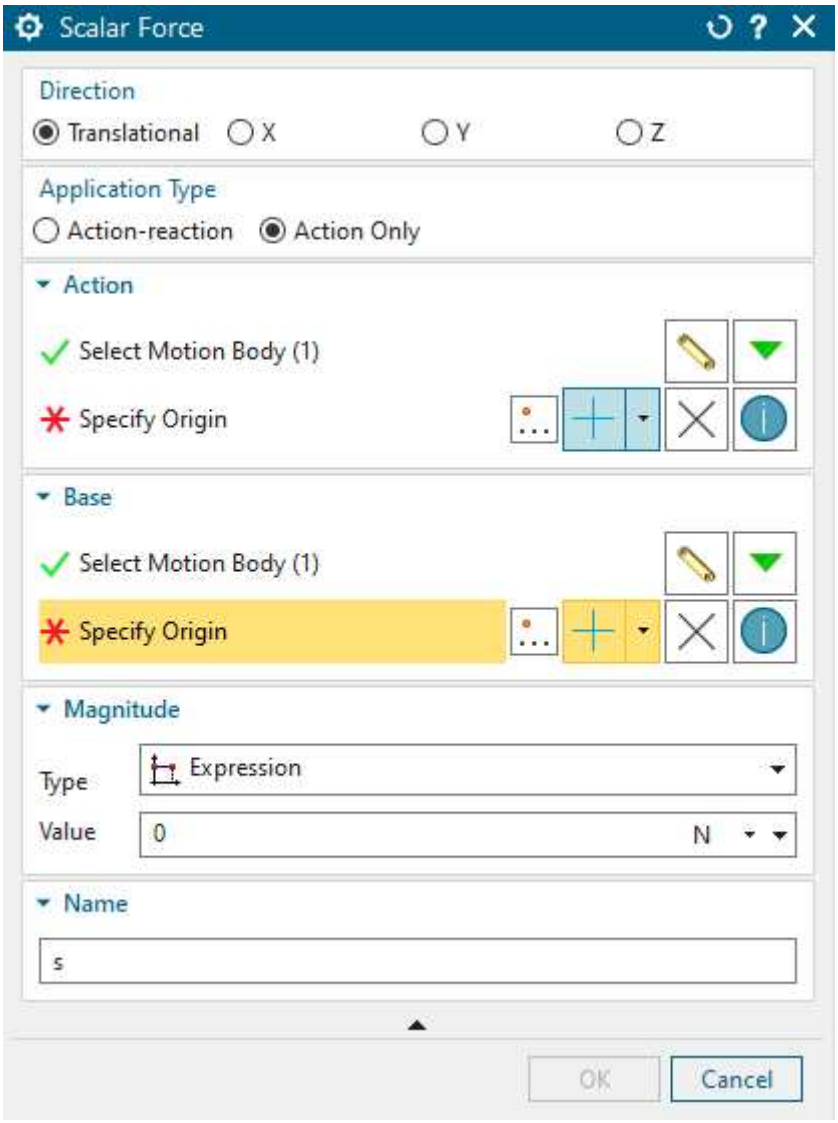


Figure 32/1: load setting

4.6.2 Honeycomb force

In order to simulate the costant force generated from the honeycomb during its deformation, a couple of forces are modelled. These forces simulate a action-reaction force between the honeycomb and the two component

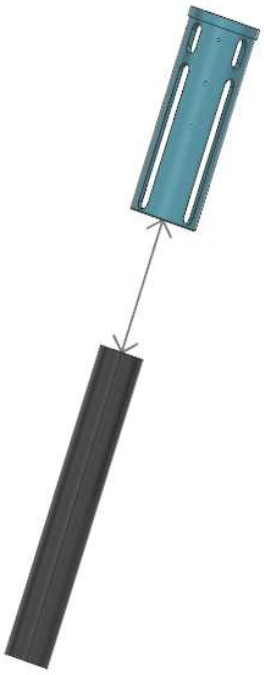


Figure 33 : honeycomb replaced by a couple of force

4.6.3 Anti-pullout force

To accurately represent the mechanical behavior of the assembly, the model required the implementation of a function capable of preventing the pull-out of the inner tube from the primary structure. This was necessary to replicate the effect of the adhesive bond created in the physical system by a flange, which is mechanically fastened to the inner tube and connected to the crush-box. The function serves to simulate this connection, ensuring that the inner tube remains fixed relative to the surrounding structure under operational loads.

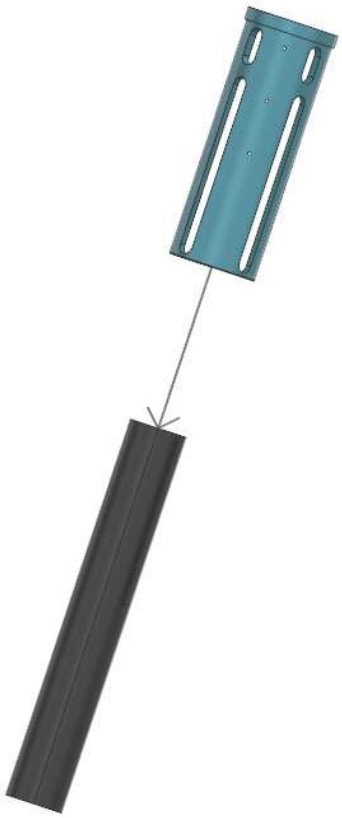


Figure 34 : anti pullout simulated by a force on the tube B

4.7 Step function

The **STEP** function defines a smooth transition between two constant values using a cubic interpolation. It is particularly useful in contexts where abrupt changes should be avoided, such as in numerical simulations or graphical animations.

$$STEP(u, x_{\min}, y_{\min}, x_{\max}, y_{\max})$$

The function takes an input expression u, along with two intervals: $[x_{min}, x_{max}]$ and $[y_{min}, y_{max}]$. When u is less than x_{min}, STEP returns y_{min}; when u exceeds x_{max}, it returns y_{max}. For values of u in between, it computes a cubic curve connecting the points (x_{min}, y_{min}) and (x_{max}, y_{max}), with zero slope at both ends. This ensures a smooth and continuous transition between the two value

4.7.1 Creation of step function on SimCenter 3D

In this paragraph, one can see step by step, the way in which one can create a step function in the software.

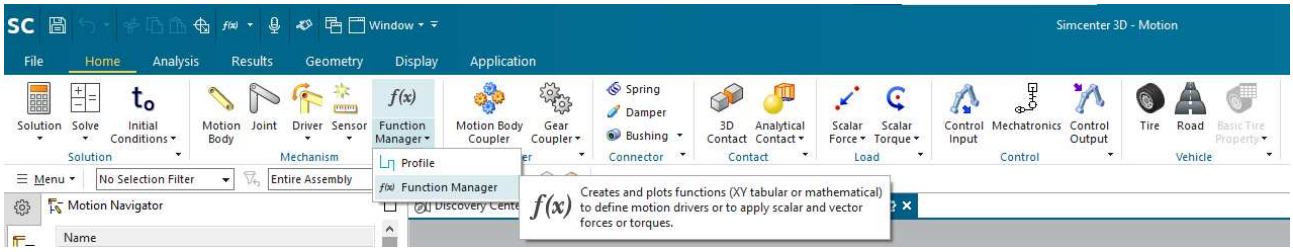


Figure 35: step function position in the menu

As one can see in the figure below, one has to choose the type of function and the purpose (in this thesis is "Motion", function of "Time". Once selected "Motion – Functions" in "Insert", one has to write the formula

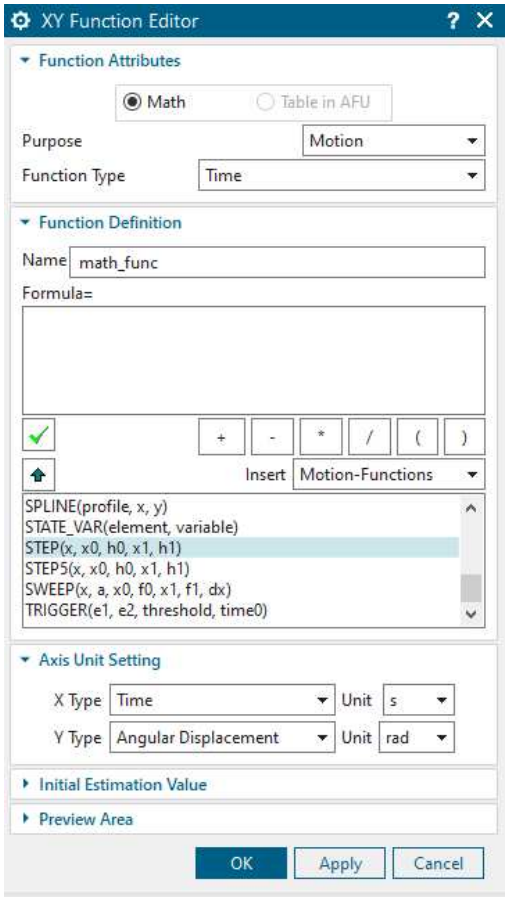


Figure 36: step function setting

4.7.2 Step function – Single cartridge honeycomb

The value of the force of the single honeycomb is calculated as:

$$F_{high-crush} = \sigma_{high} \times A_{CRUSH-BOX} = 5.17 \frac{N}{mm^2} \times 4958.2\, mm^2 = 25634\, N$$

The function utilized is:

```
STEP(Se_vel_1, -0.05, 25634, 0, 0)
```

This is the function utilized for the leg 1. The input take into account is the sensor velocity between tube B and the impact endstop. When the relative velocity is negative (with a threshold value of 0.05 mm/s), so it means that in the real the honeycomb is in compression, the force of 25639 N is activated. For positive value, the force is 0.

4.7.3 Step function – Double cartridge honeycomb

The function utilized is:

```
STEP(Se_vel_1, -0.05, (STEP(Displacement_1,196.8,18296,198.8,0)+STEP(Displacement_1,66.3,7338,68.3,0)), 0, 0)
```

This is the function utilized for the leg 1. With respect the function of the single cartridge honeycomb, one has substituted the force of 25639 N with the two forces of the two cartridge. In particular, the input is the displacement sensor between the tube B and the impact endstop. From the initial value to 68.3 mm, so the length of the first crush-box, the force is 18296 N. Then, the force is 7338 N, so the force generated from the deformation of the second crush-box.

4.7.4 Step function – Anti pullout force

The function utilized is:

```
STEP(Se_vel_1, 0, 0, 0.01, -1000)
```

This is the function utilized for the leg 1. The input take into account is the sensor velocity between tube B and the impact endstop. When the relative velocity is positive (with a threshold value of 0.01 mm/s), so it means that in the real there is the pull-out of the inner tube from the primary structure, a force of -1000 N is activated. For negative value, the force is 0.

CHAPTER 5 : FLEXIBLE BODY

To enhance the accuracy and realism of the simulation results, the modeling activity was extended to include a multibody model with flexible components (flexible body modeling). This approach accounts for elastic deformations of structural elements during motion and dynamic interactions within the system, thereby overcoming the limitations of a fully rigid-body model.

In particular, the main structural elements of the system, those subjected to significant loads during operation or playing a critical role in the overall dynamics, were modeled as flexible bodies. Conversely, the central body of the Lander, namely the main load-bearing structure, and the contact devices with the ground (FOOTPADs) were kept rigid. This decision was motivated both by computational considerations, aimed at reducing model complexity and simulation time, and by physical reasoning, as these components are designed to behave predominantly as rigid bodies under expected operational conditions.

This phase marked a substantial advancement in the simulation, making it more representative of the system's actual physical behavior and providing more reliable insights for the structural design and dynamic control of the Lander.

5.1 Creation flexible body

To perform a flexible body simulation in Simcenter, a structured workflow was followed, starting from a rigid component to create a FEM model with the aim of considering elastic deformations within the multibody simulation. The detailed steps are described below.

5.1.1 FEM Model Creation

The first step involved transitioning from the Motion environment to the **.prt** environment, where the **"New FEM and Simulation"** procedure was launched. This operation automatically generated two associated files: one with the **.fem** extension (for the finite element model definition) and another with the **.sim** extension (for simulation setup).
This phase is crucial as it constitutes the starting point to define the deformable representation of the component, which was initially treated as a rigid body.

5.1.2 Mesh Generation

Once inside the **.fem** environment, the three-dimensional mesh of the component was generated. An appropriate discretization was selected according to the geometry and the required level of detail, specifying parameters such as:

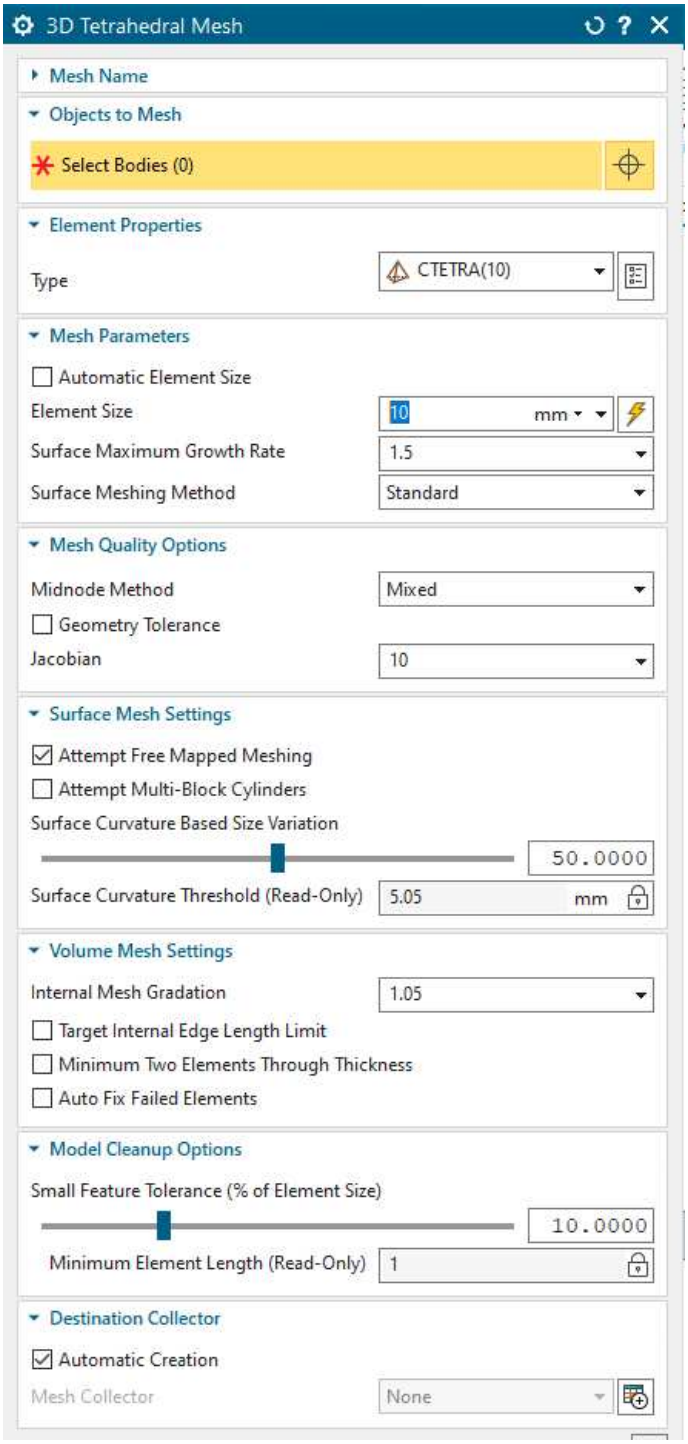


Figure 37: Mesh Parameters

5.1.3 Material Assignment

After meshing, the material was assigned to the model. A material consistent with the real physical properties of the component was selected, defining parameters such as:

MATERIAL	**E (GPa)**	ν	$R_y(MPa)$	$R_U(MPa)$	$\rho\ (\frac{kg}{m^3})$
AA7075 T651	70	0.346	503	572	2710
Ti6Al4V	114	0.34	880	950	4460
CFRP	53.3	0.05400001			1510

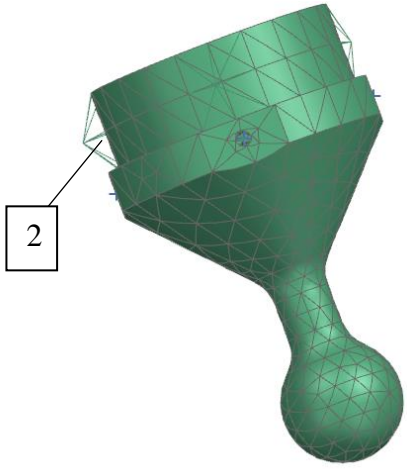
Table 8 : properties of material utilized

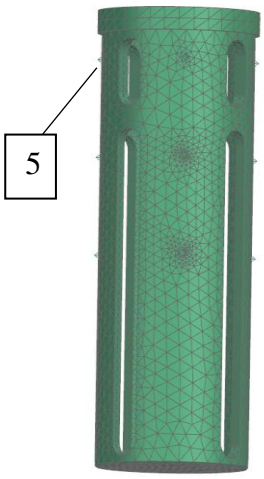
* shear modulus CFRP: 4.0099999e9 Pa

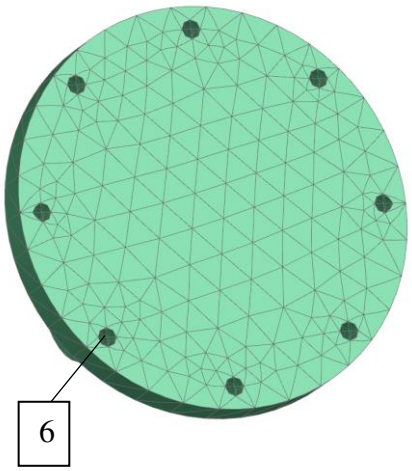
This phase is essential to ensure that the flexible body's behavior in the simulation reflects the real component's response under applied loads.

5.1.4 RBE2 Constraint Definition

Within the same **.fem** environment, **RBE2 (Rigid Body Element 2)** constraints were created. These constraints were positioned at the joints used in the rigid body version of the model. The RBE2 elements connect mesh nodes to the rigid nodes, ensuring correct transfer of forces and moments. The use of these constraints is essential to guarantee that the flexible body's connection points are compatible with those in the multibody simulation. As I said in the 4.3 paragraf, some joints are multiple. In the next figures, one can see the exactly positioning. The numeration is made with the usual labels







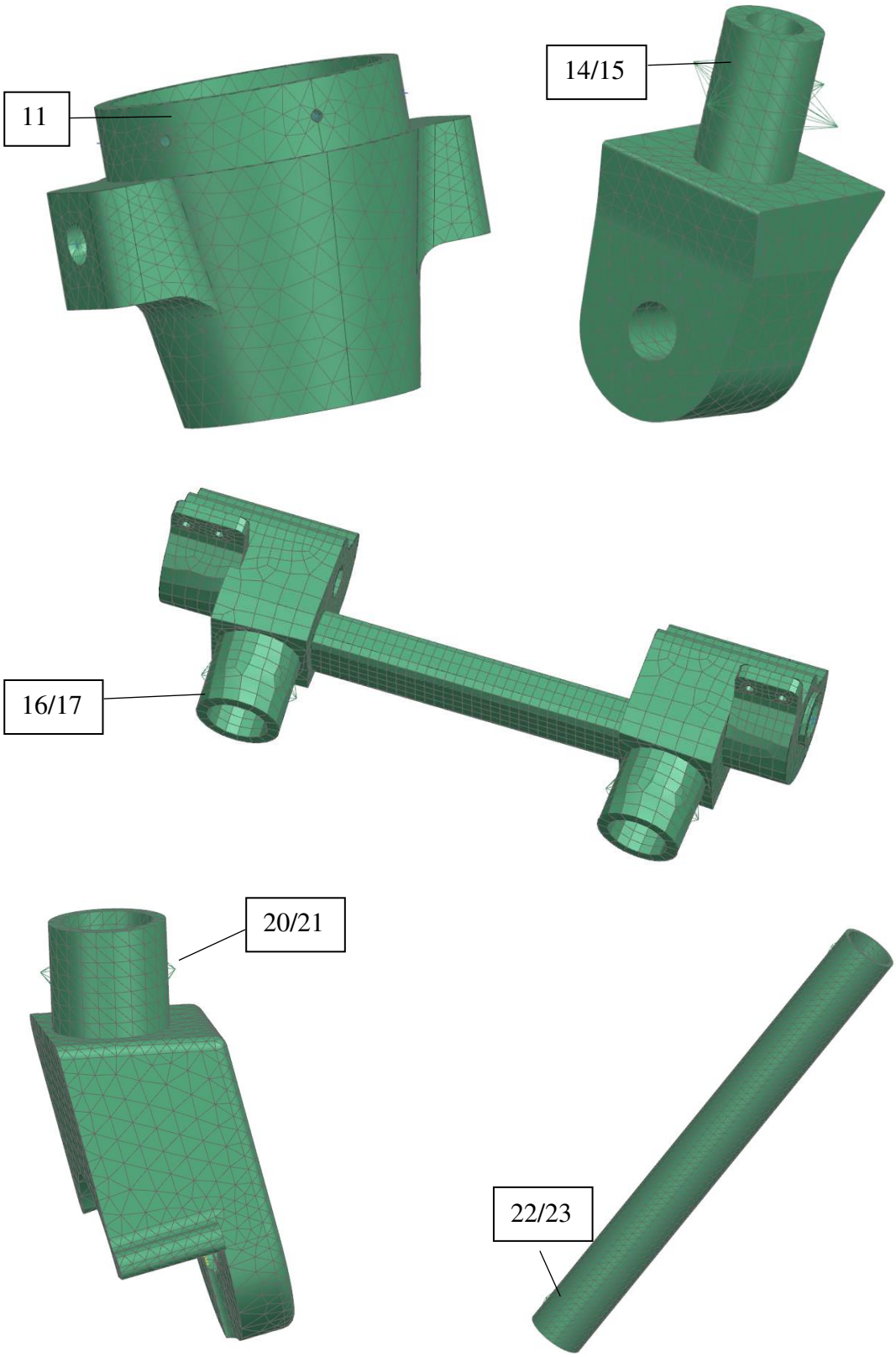


Figure 38: RBE2 positioning

5.1.5 Boundary Condition Definition

After completing the FEM model preparation, the process moved to the **.sim** environment. Here, the **"Fixed Boundary Degrees of Freedom"** function was used to fix all six degrees of freedom (3 translational and 3 rotational) of the previously created RBE2s. During this phase, the software automatically eliminates redundant constraints to avoid over-constraining errors in the model.

This step defines temporary fictitious kinematic constraints necessary to allow the solver to compute modal deformations and the global stiffness matrix before exporting the flexible body.

5.1.6 Flexible Body Export

Once meshing, material assignment, and constraint definition were complete, the flexible body was exported. This exported file serves as the basis for replacing the corresponding rigid body in the multibody simulation.

5.1.7 Integration into the Motion Simulation

Finally, the workflow returned to the **Motion** environment, where the previously generated flexible body was imported. This involved replacing the rigid body with its deformable counterpart while maintaining existing kinematic connections (joints, forces, actuators, etc.).

Thanks to this step, it became possible to run a simulation that accounts for the component's flexibility, allowing evaluation of:

- realistic dynamic effects (such as vibrations, bending, resonances),
- internal force distributions,
- and potential structural criticalities.

CHAPTER 6 : CASE 9

In this chapter, the main results of Case 9 are presented and discussed. This scenario is characterized by a frontal impact between the lander and an idealized Martian rock. Along with Case 10, it is considered one of the most critical cases due to the high impact force and the significant amount of energy that must be dissipated upon landing.

The terrain in this simulation features a slope inclined at 15 degrees, while the lander initially maintains a vertical orientation. The dynamics of the system are further complicated by the presence of an initial velocity applied to the lander in both the horizontal (X-axis) and vertical (Z-axis) directions. The lander contacts the surface with a single leg, which makes the impact even more severe and represents a worst-case scenario in terms of load distribution and structural response. This case provides valuable insight into the lander's behavior under extreme conditions, contributing to a better understanding of the critical parameters involved in landing on uneven and obstacle-rich Martian terrain.

6.1 Landing dynamics

The main phases of the landing can now be observed. For clarity in the following description, the numbering of the lander's legs is shown in the figure below. This reference will help to better understand the sequence of events. The name given to each phase will be reused in the following paragraphs in order to link the events to the graphs.

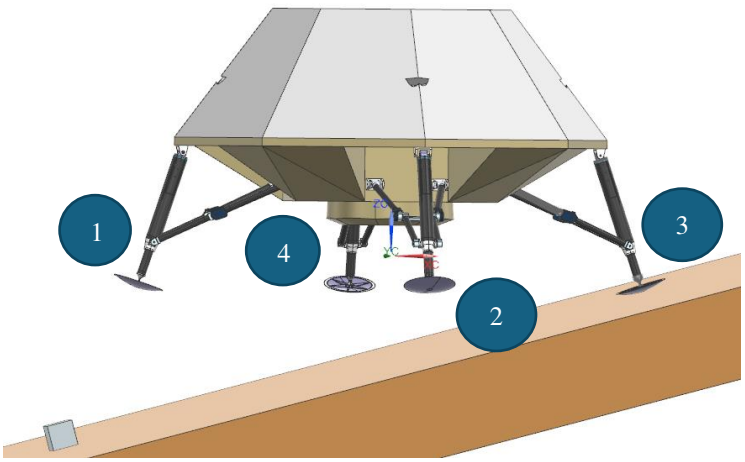


Figure 39: legs numeration

6.1.1 Initial condition

The lander is ready to land.

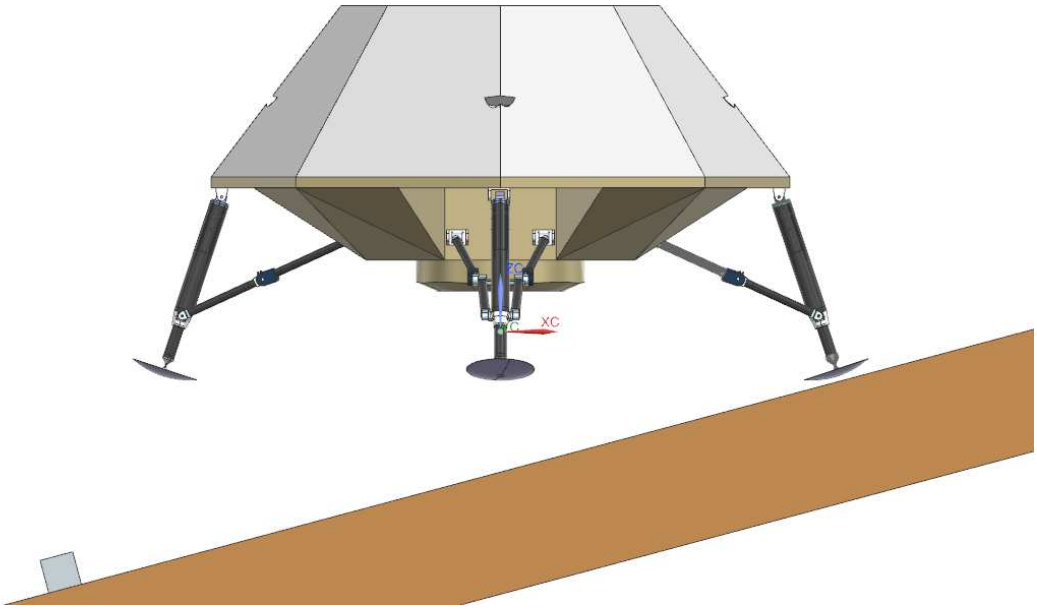


Figure 40: initial condition phase

6.1.2 First impact

The first leg that impact the land is the leg 1 and its crush-box starts to deform.

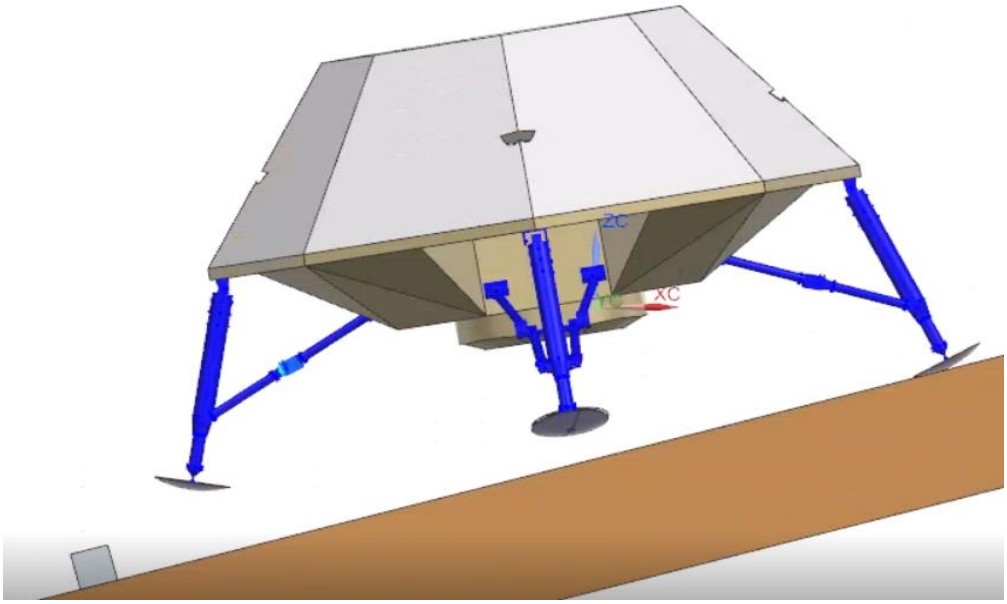


Figure 41: first impact phase

6.1.3 First stabilization

The remaining legs (2,3,4) impact with the land

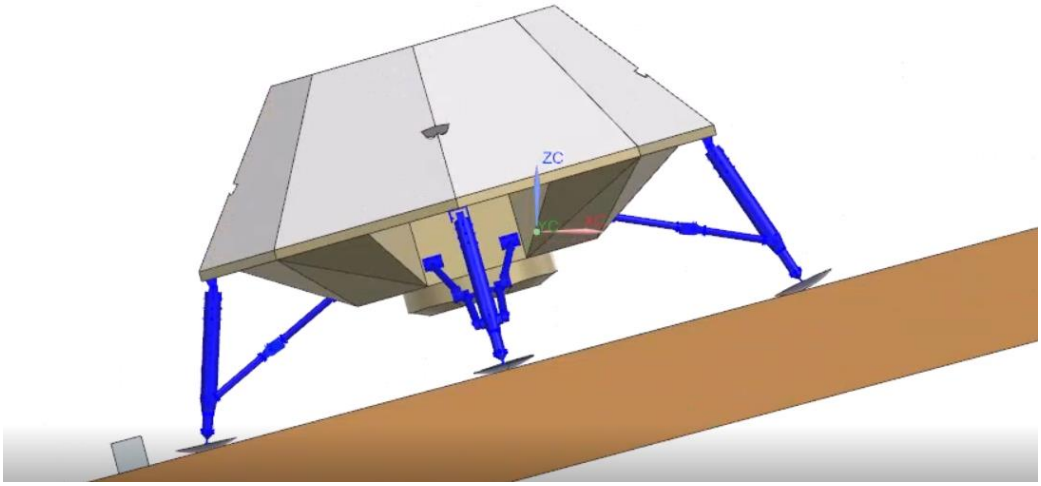


Figure 42: first stabilization phase

6.1.4 Sliding

Before hurt the rock, the lander has a short sliding

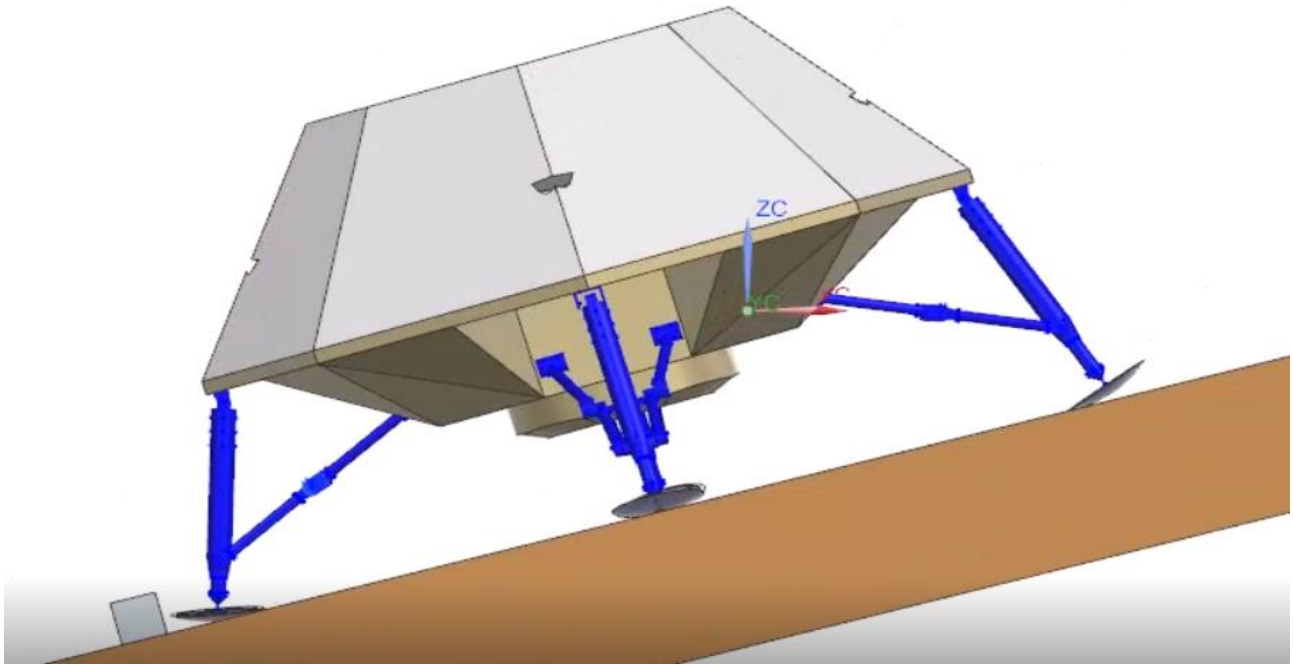


Figure 43: sliding phase

6.1.5 Impact with the rock

The leg 3 impact with the rock.

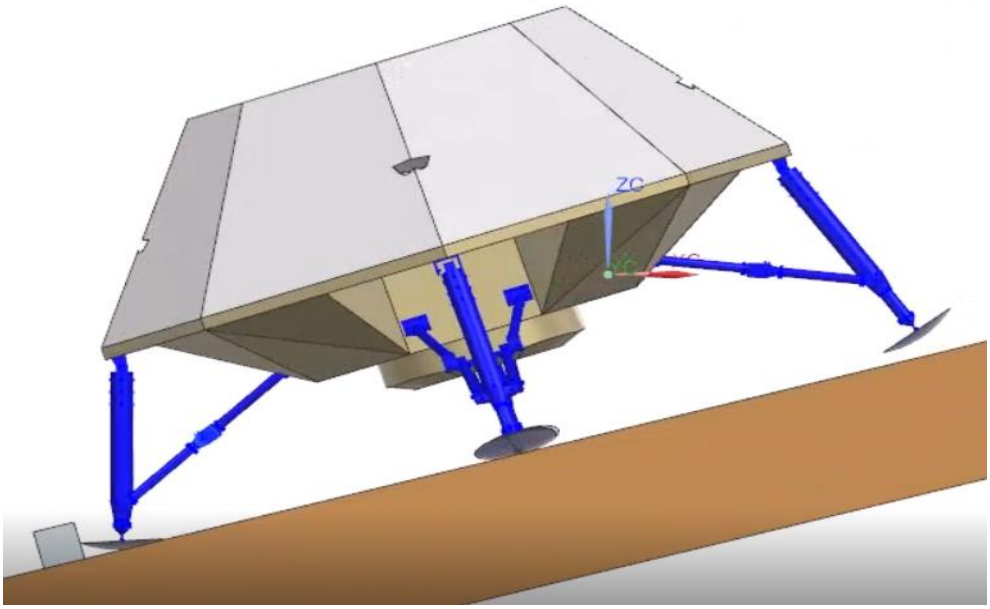


Figure 44: impact with the rock phase

6.1.6 Overturning

The lander overturn maintaining only the touch with the land with the leg 3

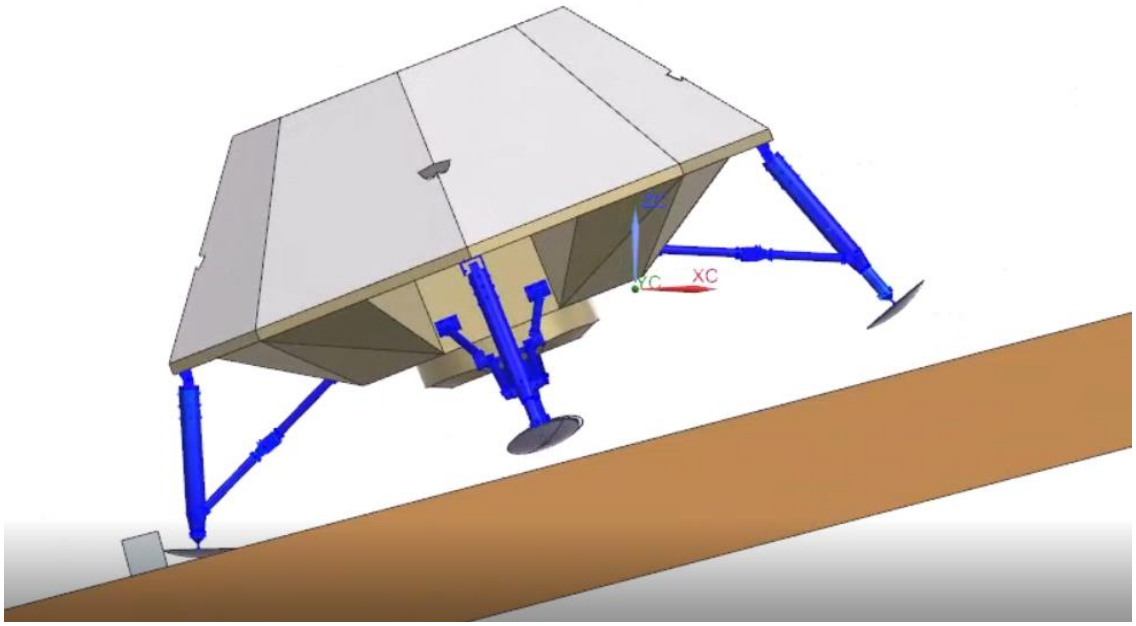


Figure 45: overturning phase

6.1.7 Second impact

The overturning motion comes to an end, and the lander falls back onto the ground, causing a second deformation of the crush-boxes.

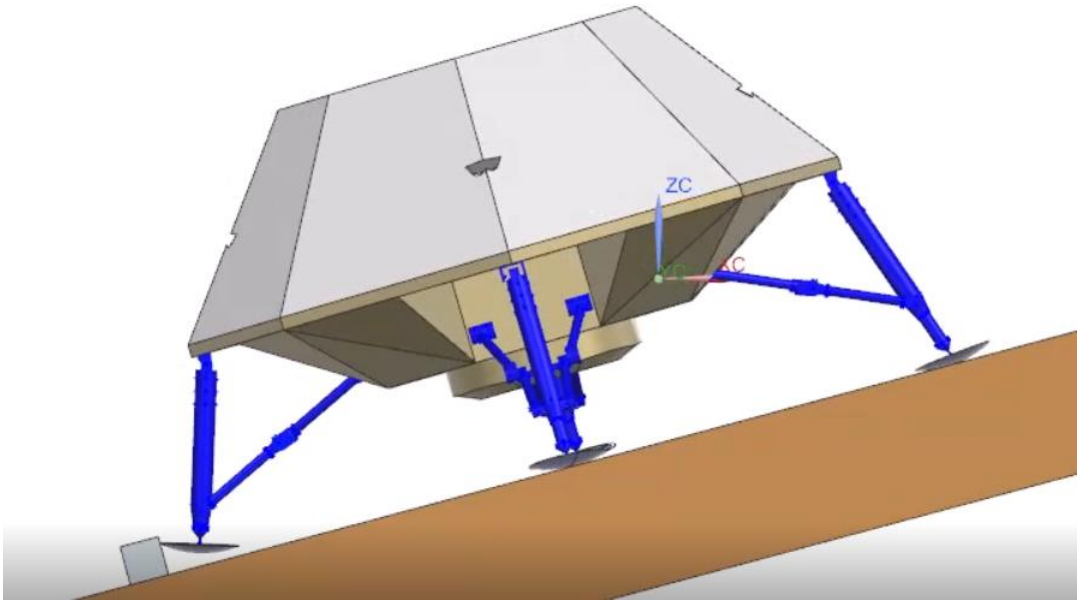


Figure 46: second impact phase

6.1.8 Complete stop

After a brief additional sliding, the lander comes to a complete stop.

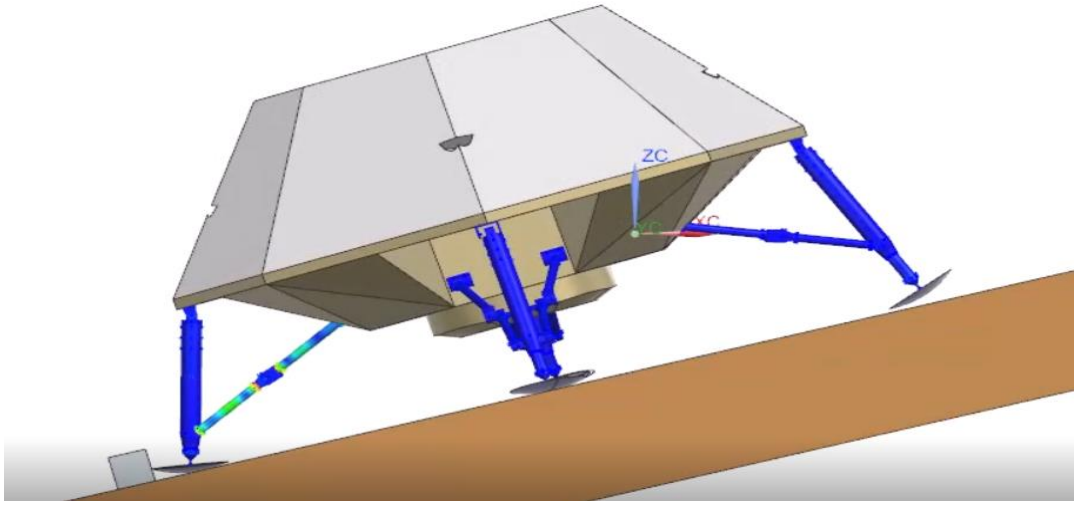


Figure 47: complete stop phase

6.2 Stability index – Single cartridge

In order to verify if the criterion of the stability index are satisfied, the parameters before discussed in the paragraph 3.3 are calculated

- $H_{m=}\ 1270{,}304\ mm$
- $H_i = 2451{,}148\ mm$
- $H = 1778\ mm$

$$K_s = \frac{2451 - 1270.304}{1778 - 1270.304} = 2{,}32$$

The criterion is satisfied because the Ks is higher than 1,5.

6.3 Safety margin – Single cartridge

As discussed in the paragraph 2.2, one of the main objectives of this thesis is to assess the safety margin for protecting the secondary strut. To do this, two markers are placed : one in the middle of the lower part of the leg and the other in correspondence of the land.

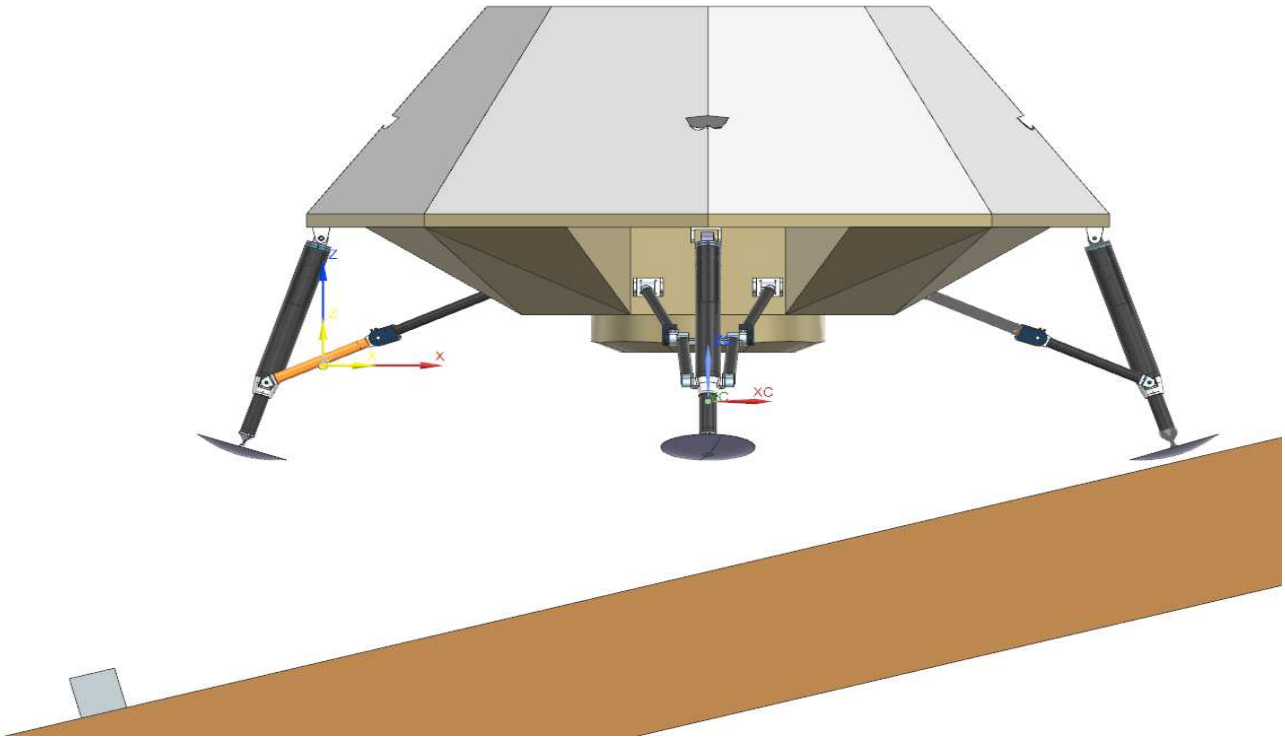


Figure 48: safety margin – case 9, single cartridge

The reference taken to consider the landing safe is 200 mm. As one can see in the graph, the final value is 283.042 mm.

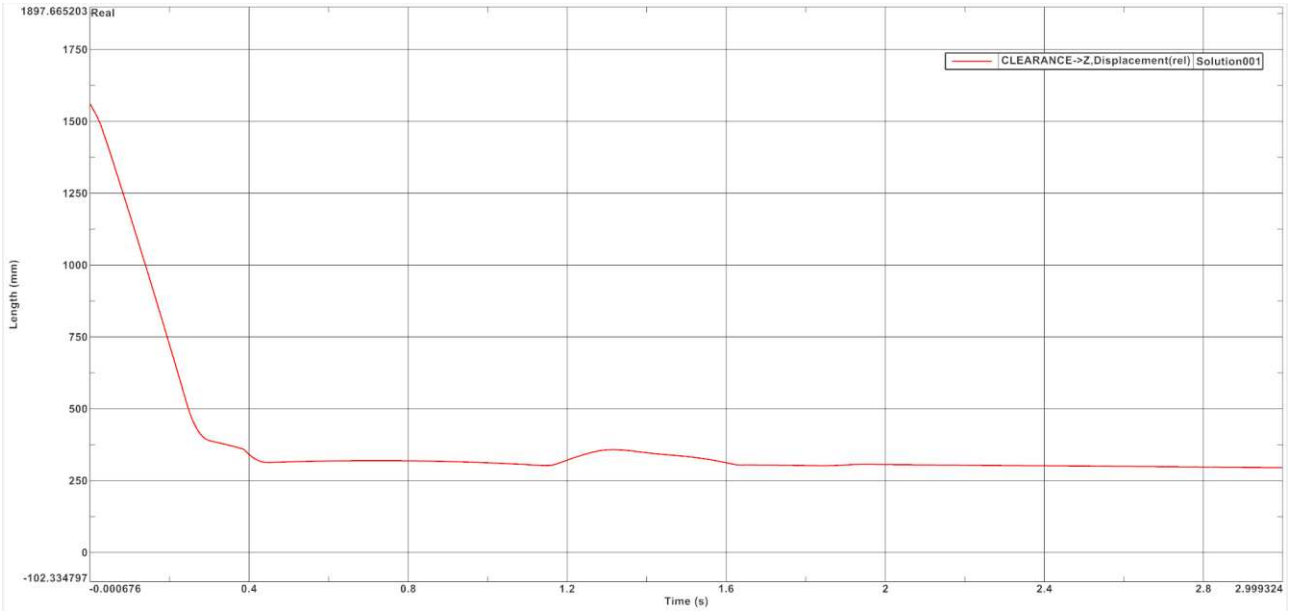


Figure 49: safety margin graph – case 9, single cartridge

6.4 Crush- box deformation (single cartridge)

In the figure below, one can see the comparison graph of the four crush-box deformation.

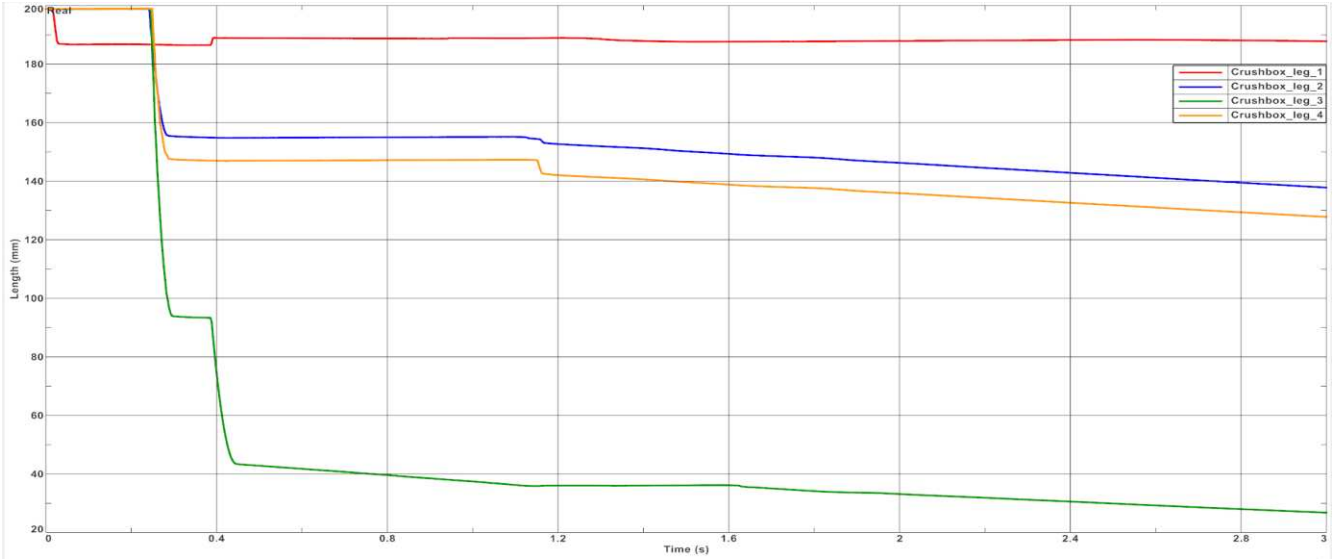


Figure 50: crush-box deformation – case 9, single cartridge

The results obtained are consistent with theoretical expectations. The most deformed crush-box is the one on leg 3. This is due to the fact that, after the initial impact involving leg 1, the entire weight of the lander shifts and is transferred onto leg 3. Conversely, the crush-box on leg 1 is the least deformed, as the first impact is very brief and is immediately followed by the lander's overturning. The deformations observed in the crush-boxes of legs 2 and 4 are fairly similar, although not perfectly identical. This slight difference may be attributed to the position of the center of gravity and the values of the moments of inertia, which influence how the load is distributed during the landing dynamics.

In the following table, one can see the precise values of deformation.

	CRUSHBOX 1	CRUSHBOX 2	CRUSHBOX 3	CRUSHBOX 4
INITIAL VALUE	198.8	198.8	198.8	198.8
FINAL VALUE	187.77	137.8	26.87	127.85
% DEFORMATION	5.54	30.68	86.48	35.68

Table 9 : crush-box deformation – case 9, single cartridge

6.5 Impact loads – single cartridge

The graphs show in the next parts have been normalized and smoothed in order to have a better view and to help to understand better the trends.

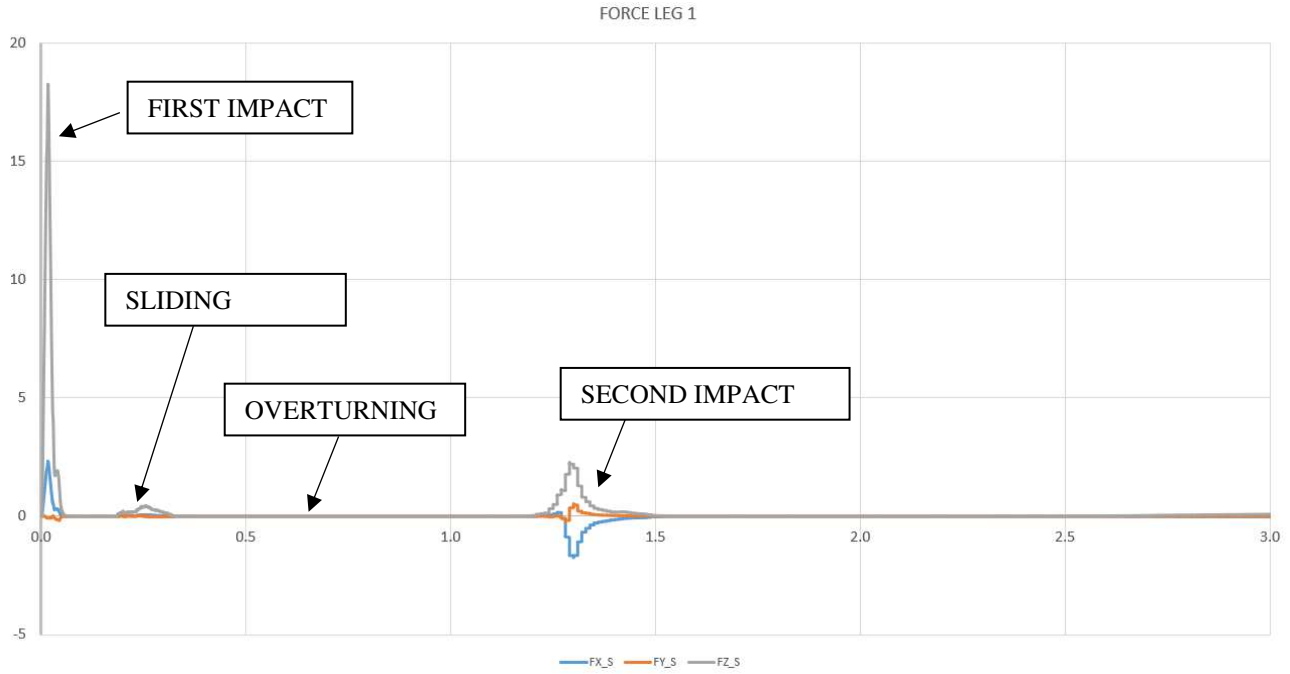


Figure 51: impact loads – leg 1, case 9, single cartridge. Dimensionless force (Y), time in s (X)

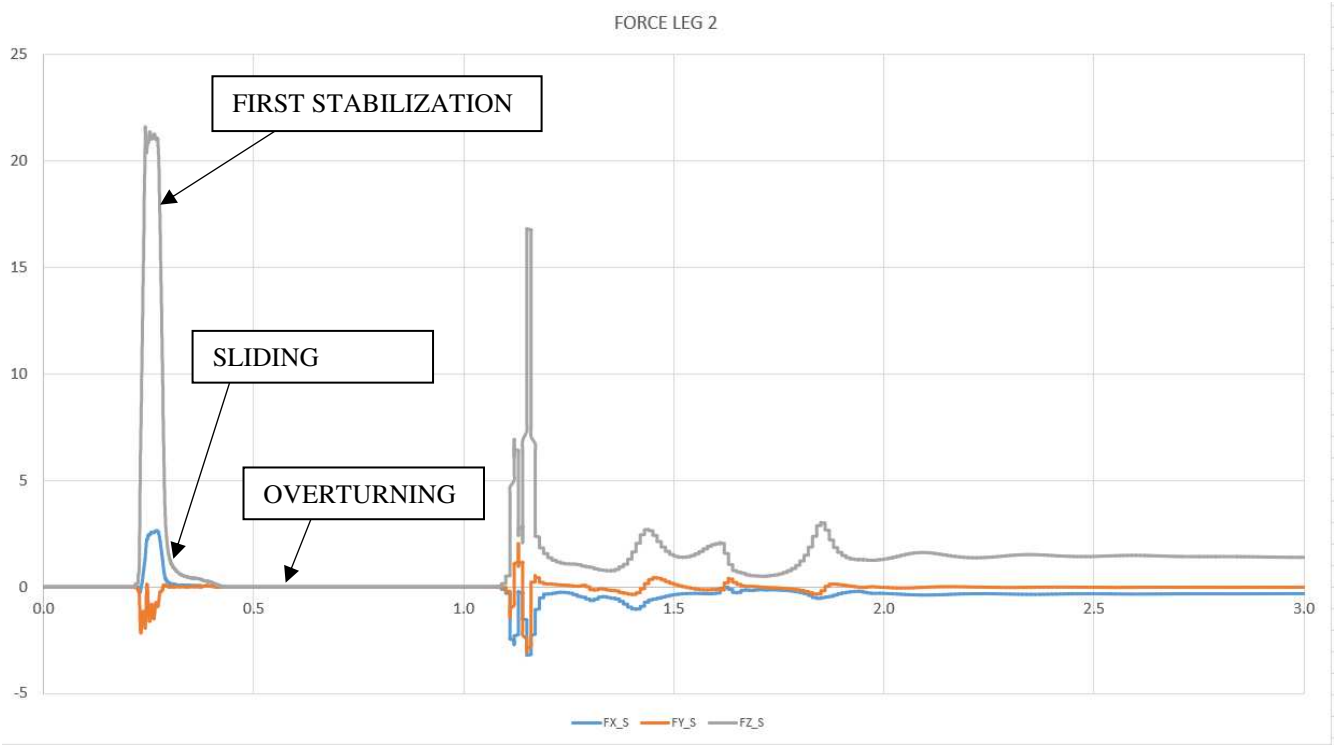


Figure 52: impact loads – leg 2, case 9, single cartridge. Dimensionless force (Y), time in s (X)

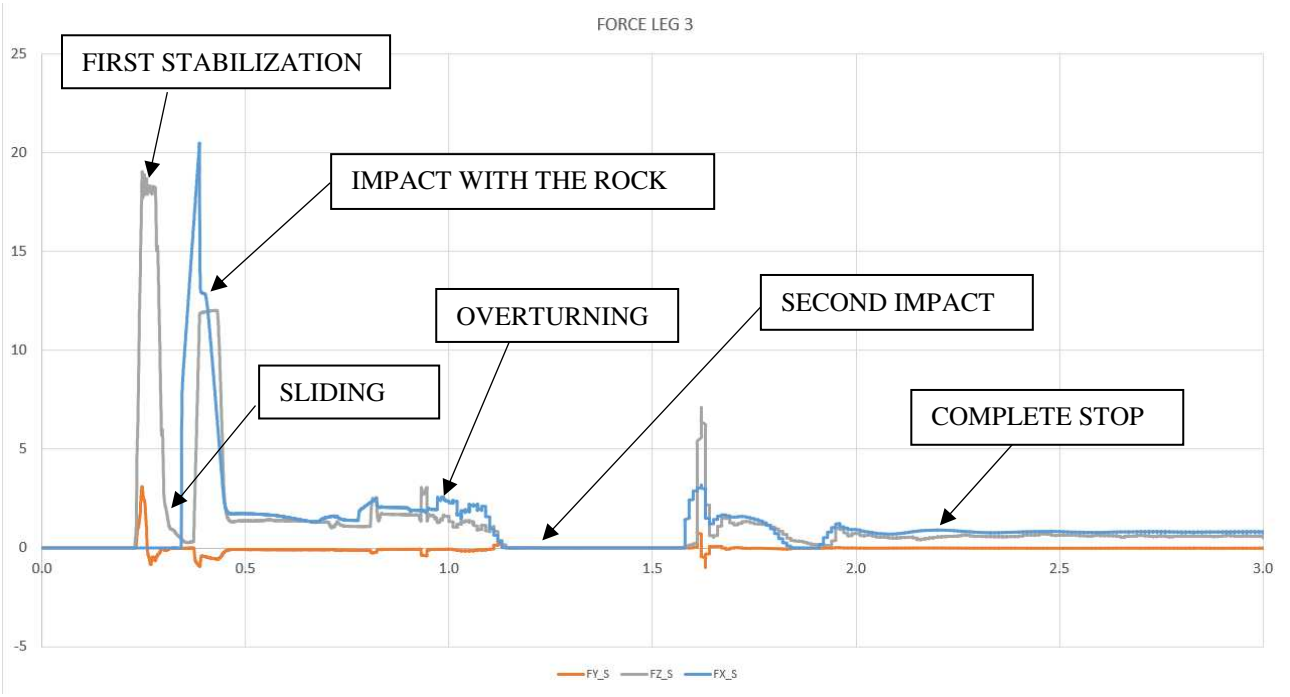


Figure 53: impact loads – leg 3, case 9, single cartridge. Dimensionless force (Y), time in s (X)

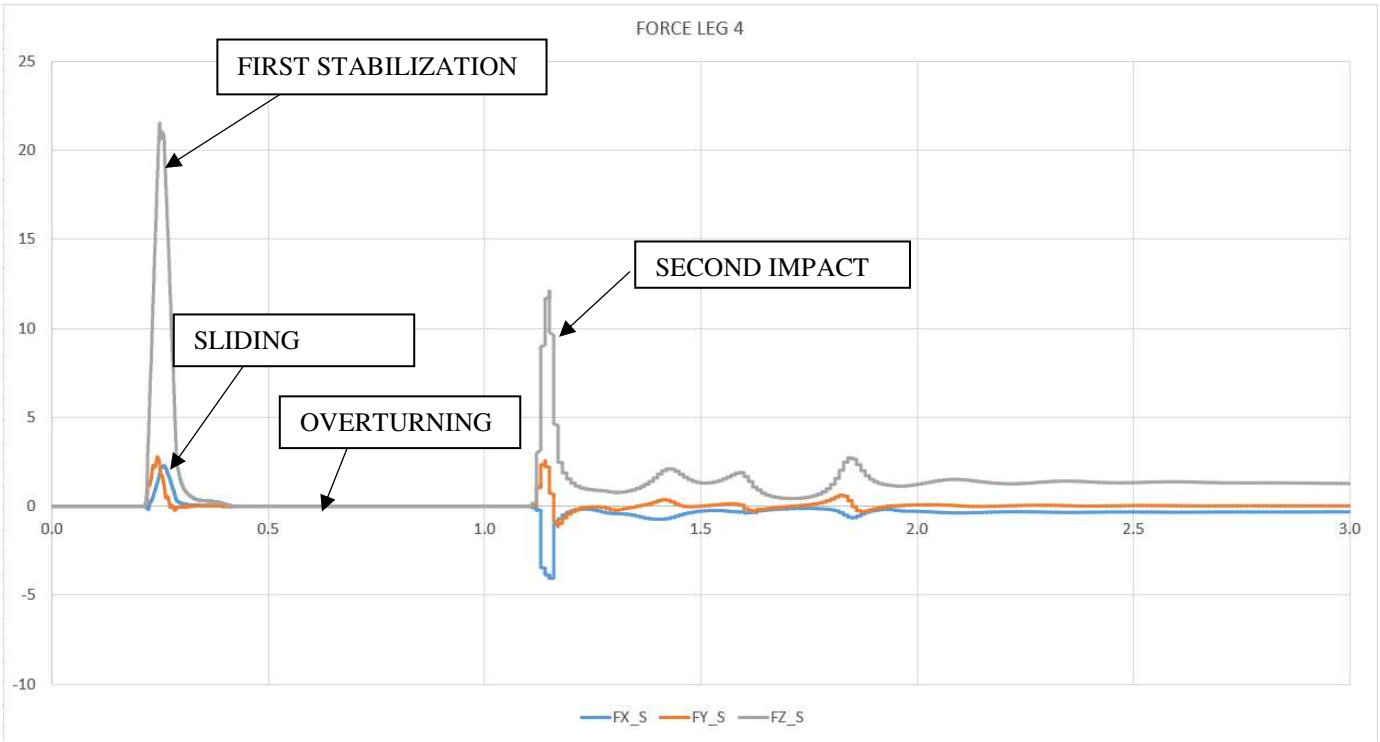


Figure 54: impact loads – leg 4, case 9, single cartridge. Dimensionless force (Y), time in s (X)

6.6 Consideration to better understand the graphs

During the simulation phase, a recurring issue emerged concerning the trends observed in the output graphs. Specifically, the graphs do not exhibit a perfectly linear behavior; instead, they are characterized by fluctuations and irregular variations. To gain a deeper understanding of these phenomena, a series of tests were conducted under varying conditions.

The first step in the investigation involved identifying potential causes that could affect the contact behavior between the pad and the ground. One key aspect is the way the software models and detects the actual contact points, which can dynamically change during the landing phase. These dynamic variations can result in a nonlinear contact force output.

A possible contributing factor is the orientation of the pads. Due to their inclined geometry, the contact points can change rapidly, leading to fluctuations in the recorded force data. Another significant factor analyzed is the stiffness of the spring connecting the pad to the spherical support. A higher spring stiffness limits the relative movement of the pad during landing, which in turn alters the landing dynamics and the resulting contact forces.

In ideal conditions (a flat surface, a lander with zero inclination, infinitely stiff springs, and perfectly vertical pads) the observed fluctuations are minimal. This suggests that the irregularities in the graph trends are primarily caused by the dynamic nature of the contact points, the pad inclination, and the mechanical properties of the system.

The following sections illustrate a selection of the tests conducted and highlight the differences observed under varying conditions.

6.6.1 Influence of pad orientation on force fluctuations

These results confirm that pad inclination significantly affects the contact behavior, with perfectly vertical pads producing more stable and linear responses.

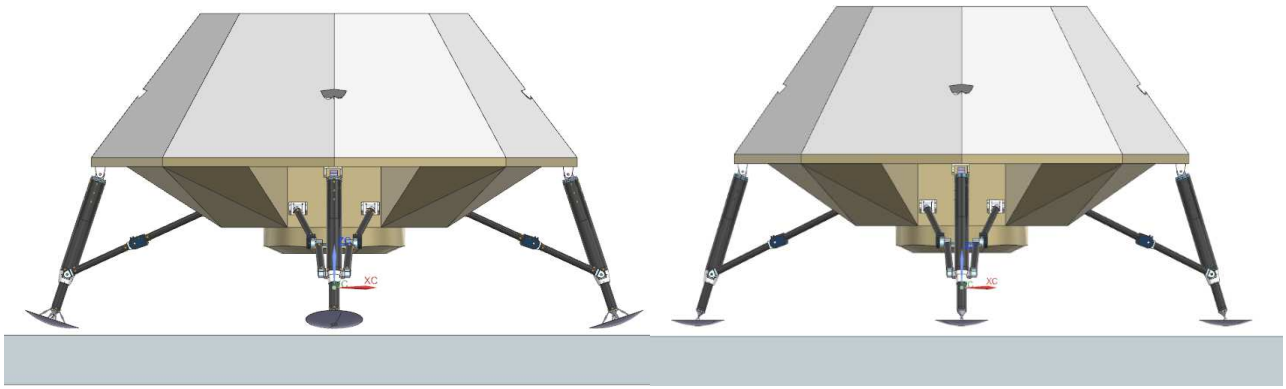


Figure 55: comparison between lander with footpads with different orientation

The graph below shows the contact force between the footpad and the ground for leg 1, with the pad inclined.

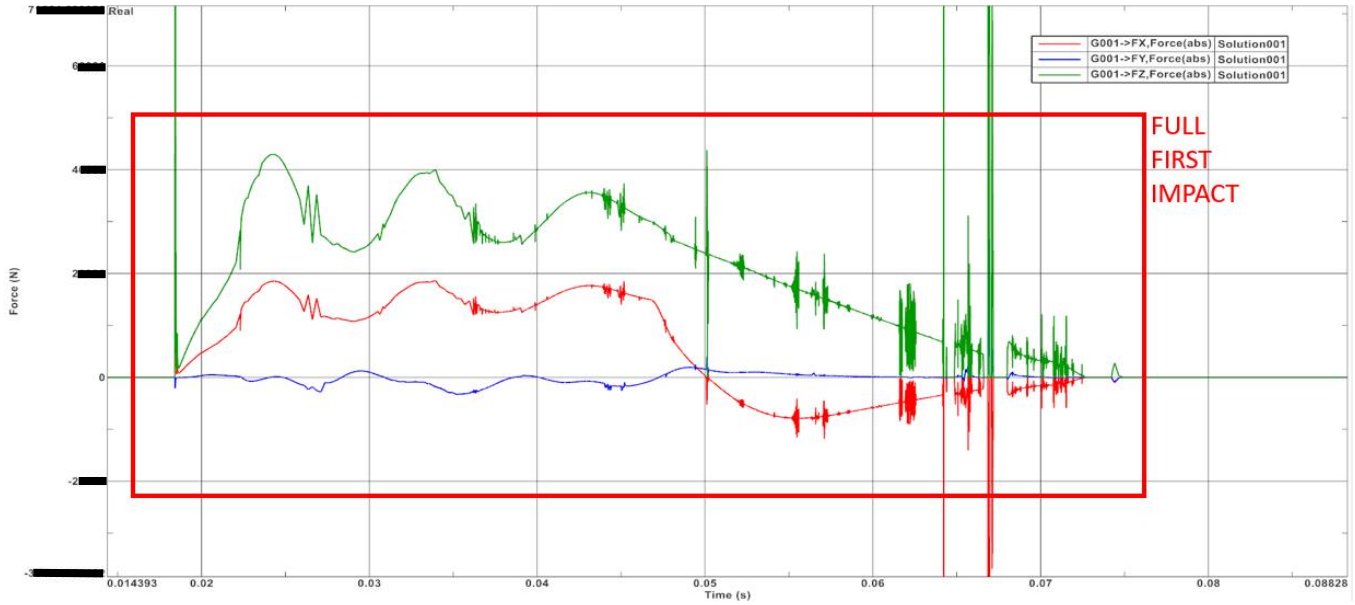


Figure 56: contact force footpad-ground with pads inclined

The graph below shows the contact force between the footpad and the ground for leg 1, with the pad not inclined.

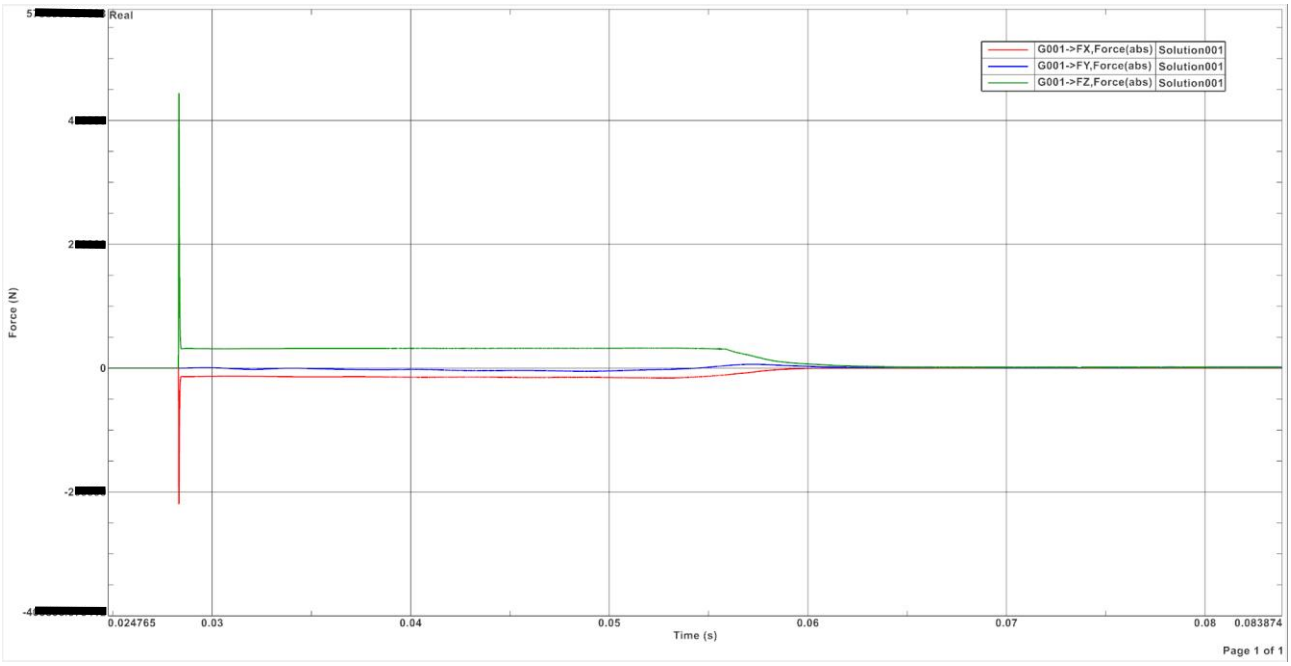


Figure 57: contact force footpad-ground with pads not inclined

As observed under identical conditions, with the only variation being the pad inclination, the fluctuations in the contact force response disappear.

6.6.2 Influence of spring's stiffness on force fluctuations

These results confirm that the stiffness of the spring significantly affects the contact behavior, with perfectly vertical pads producing more stable and linear responses. The two simulations were carried out with spring stiffness values on the order of 10,000 N/mm and 100 N/mm, respectively.

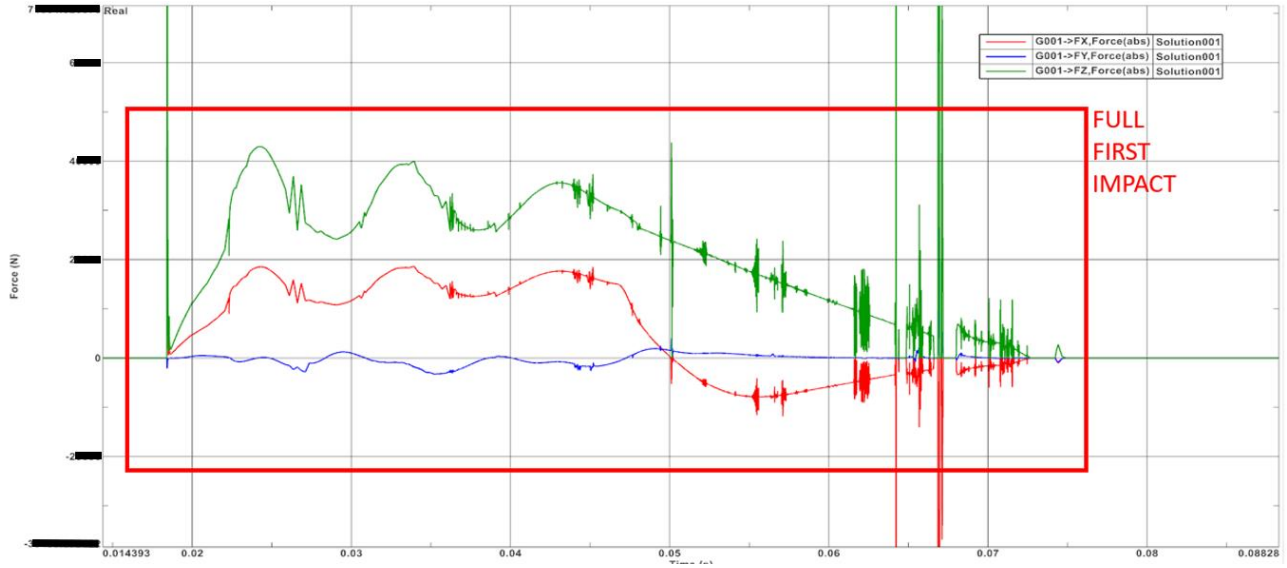


Figure 58: contact force footpad-ground with high value of stiffness

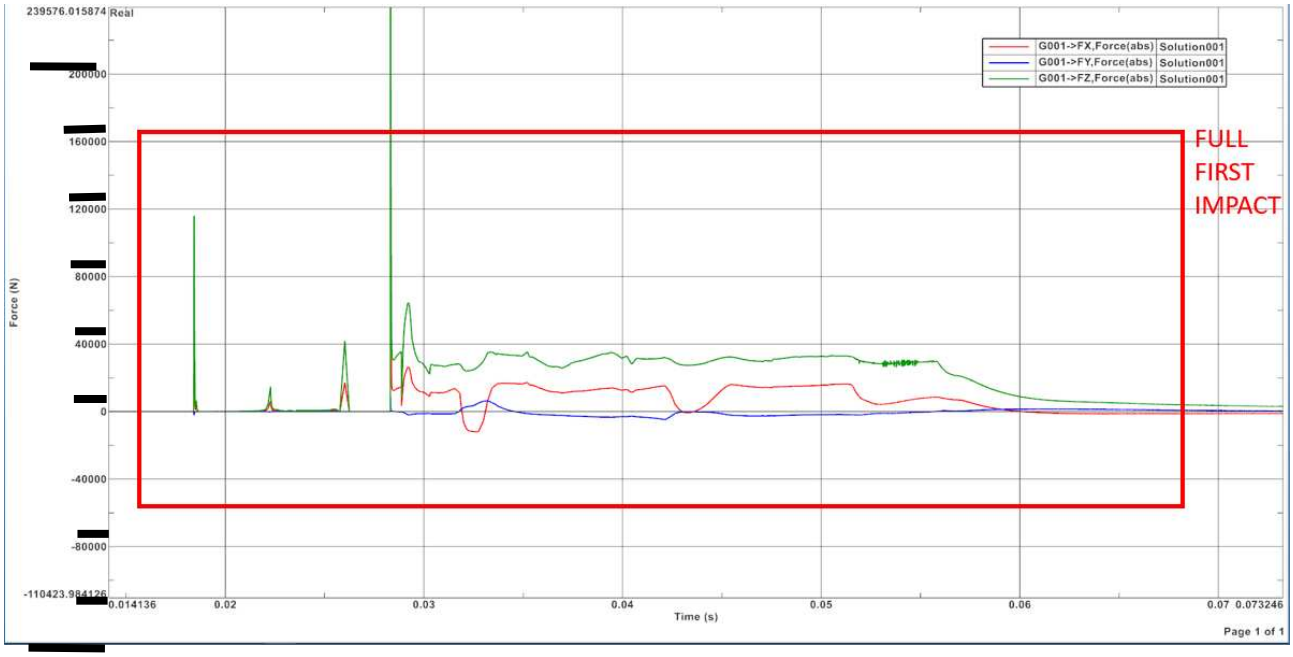


Figure 59: contact force footpad-ground with low value of stiffness

As observed under identical conditions, with the only variation being the spring's stiffness, the fluctuations in the contact force response disappear.

6.7 Stability index – Double cartridge

The same considerations are made for the configuration with the double cartridge.

- $H_{m=}$ 1270,304 mm
- $H_i = 2451{,}148\ mm$
- $H = 1780\ mm$

$$K_s = \frac{2451 - 1270.304}{1780 - 1270.304} = 2{,}27$$

The criterion is satisfied because the Ks is higher than 1,5.

6.8 Safety margin – Double cartridge

The same considerations are made for the configuration with the double cartridge

The reference taken to consider the landing safe is 200 mm. As one can see in the graph, the final value is 291.693 mm.

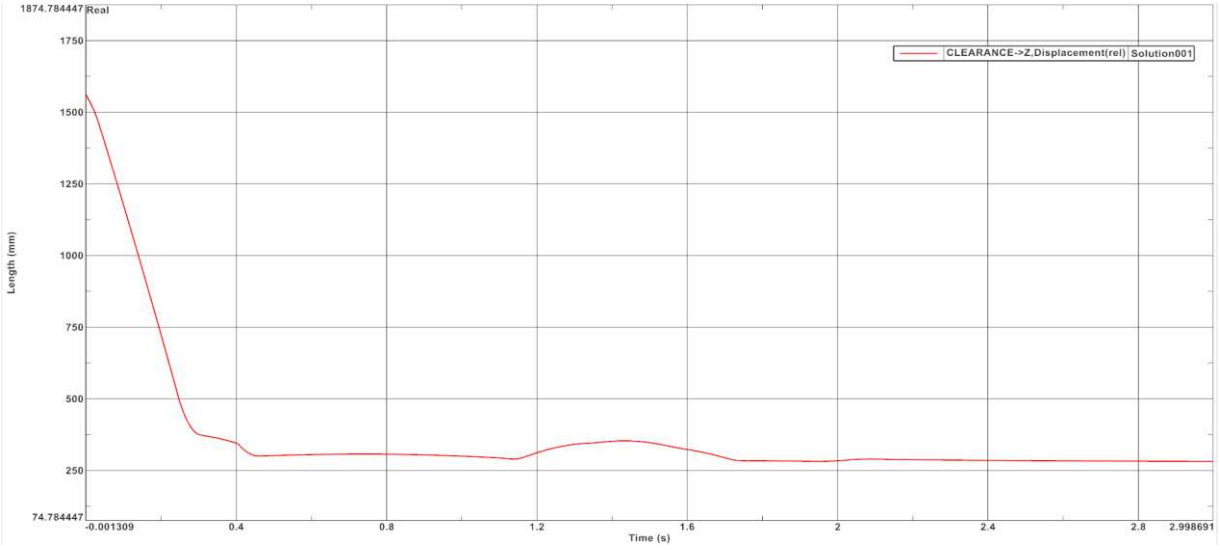


Figure 60: safety margin – case 9, double cartridge

6.9 Crush-box deformation – double cartridge

The same considerations are made for the configuration with the double cartridge.

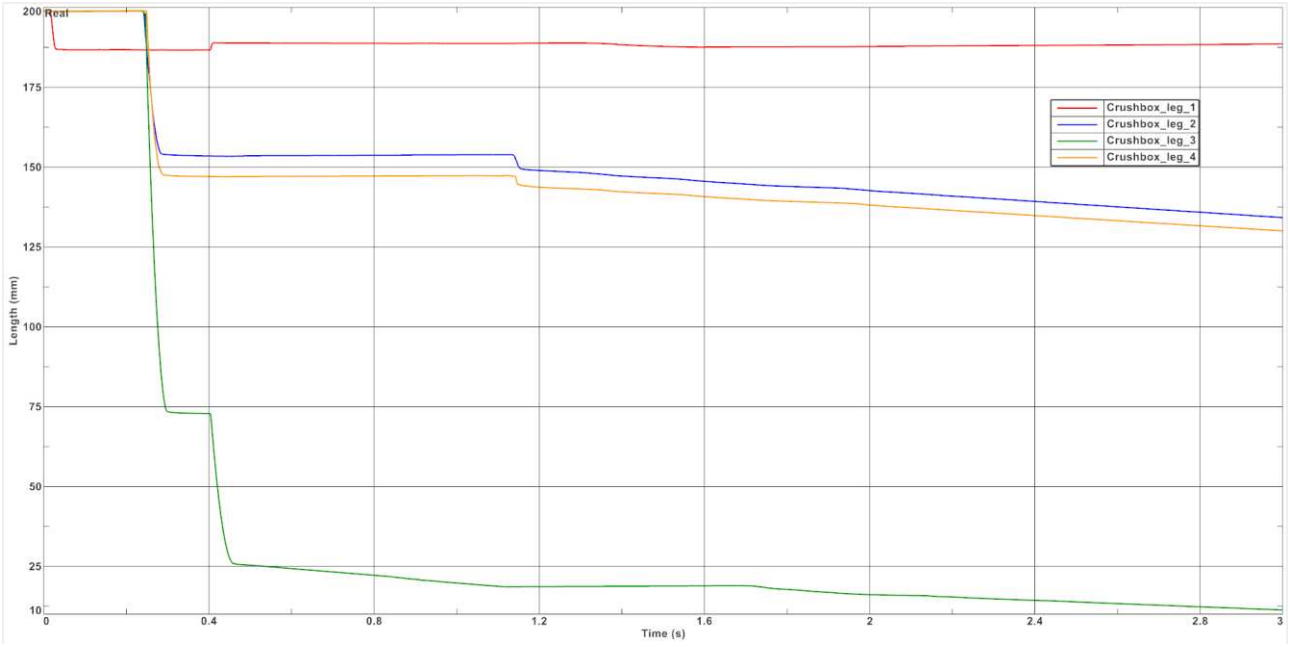


Figure 61: crush-box – case 9, double cartridge

	CRUSHBOX 1	CRUSHBOX 2	CRUSHBOX 3	CRUSHBOX 4
INITIAL VALUE	198.8	198.8	198.8	198.8
FINAL VALUE	188.49	134.12	11.1	129.9
% DEFORMATION	5.18	32.53	94.41	34.65

Table 10 : crush-box deformation – case 9, double cartridge

6.10 Impact loads – double cartridge

The graphs show in the next parts have been normalized and smoothed in order to have a better view and to help to understand better the trends.

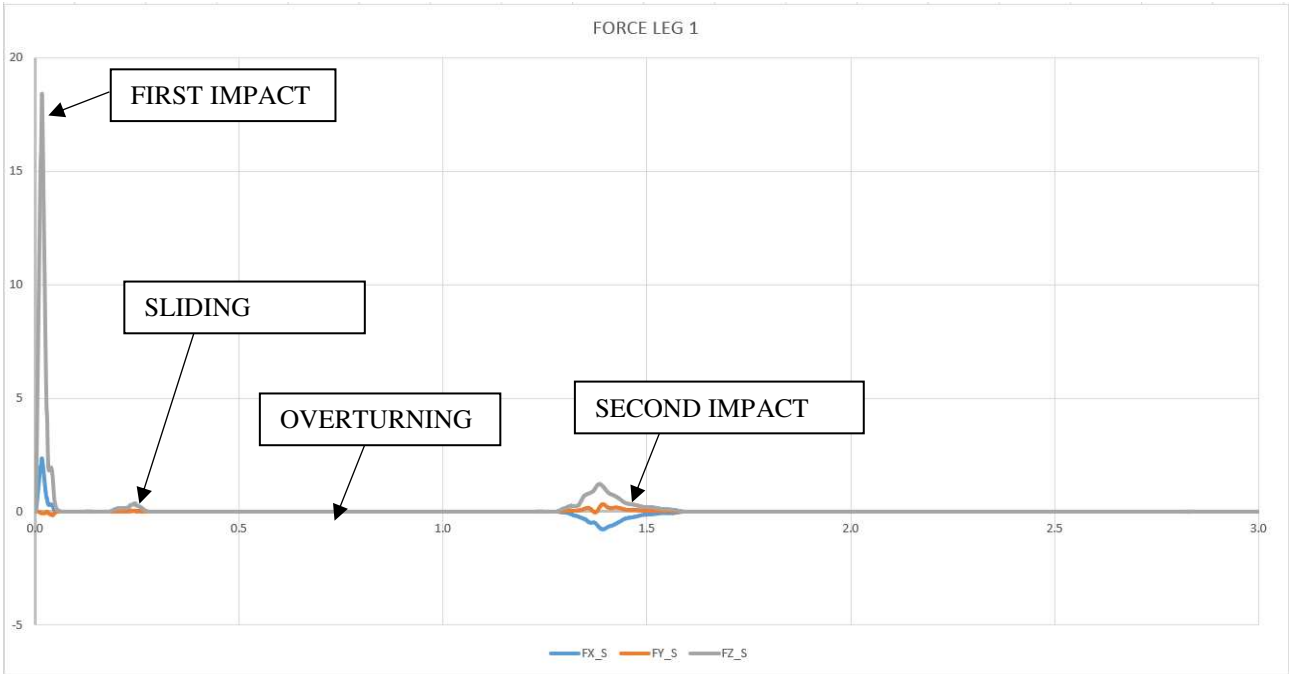


Figure 62: impact loads – leg 1, case 9, double cartridge. Dimensionless force (Y), time in s (X)

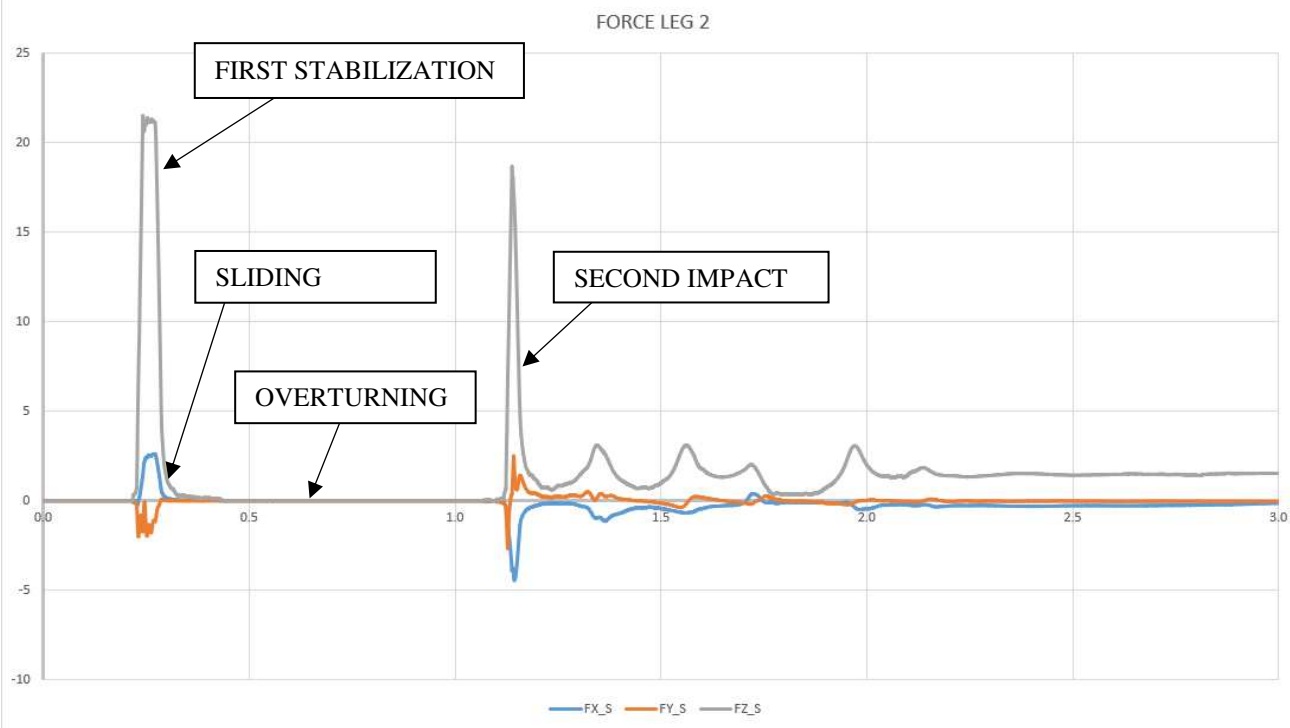


Figure 63: impact loads – leg 2, case 9, double cartridge. Dimensionless force (Y), time in s (X)

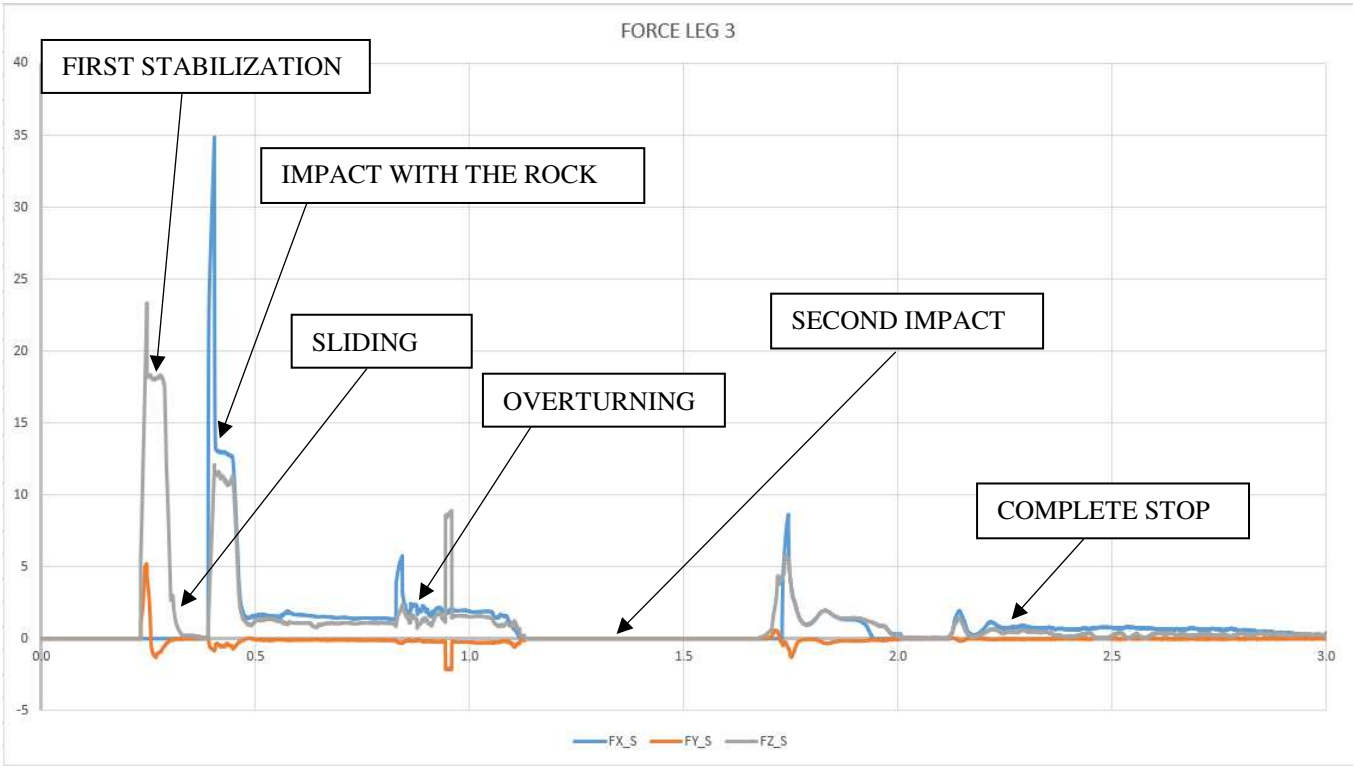


Figure 64: impact loads – leg 3, case 9, double cartridge. Dimensionless force (Y), time in s (X)

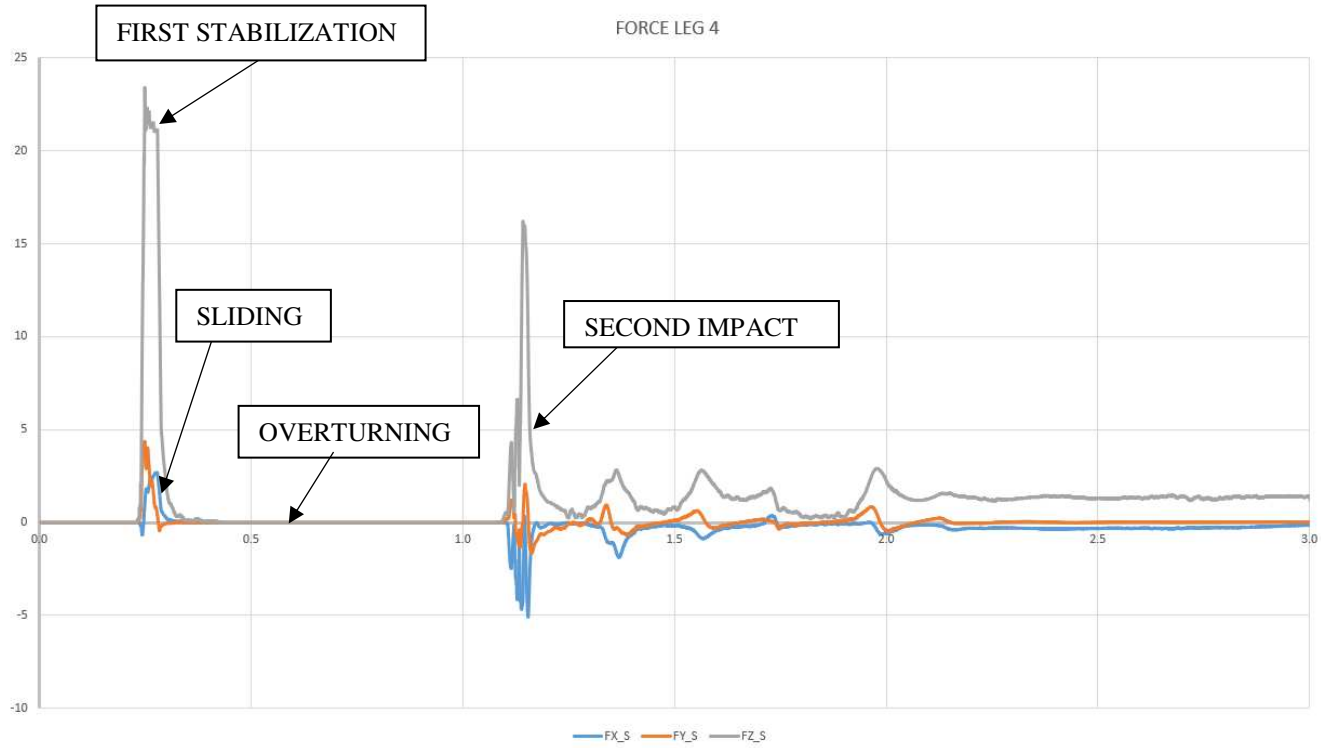


Figure 65: impact loads – leg 4, case 9, double cartridge. Dimensionless force (Y), time in s (X)

CHAPTER 7 : CASE 10

In this chapter, the main results of Case 10 are presented and discussed.

Unlike case 9, which involved a frontal impact, this scenario features a lateral collision with the rock. As previously noted, the boundary conditions remain the same, except for the positioning of the rock.

7.1 Landing dynamics

The main phases of the landing can now be observed. For clarity in the following description, the numbering of the lander's legs is shown in the figure below. This reference will help to better understand the sequence of events. The name given to each phase will be reused in the following paragraphs in order to link the events to the graphs.

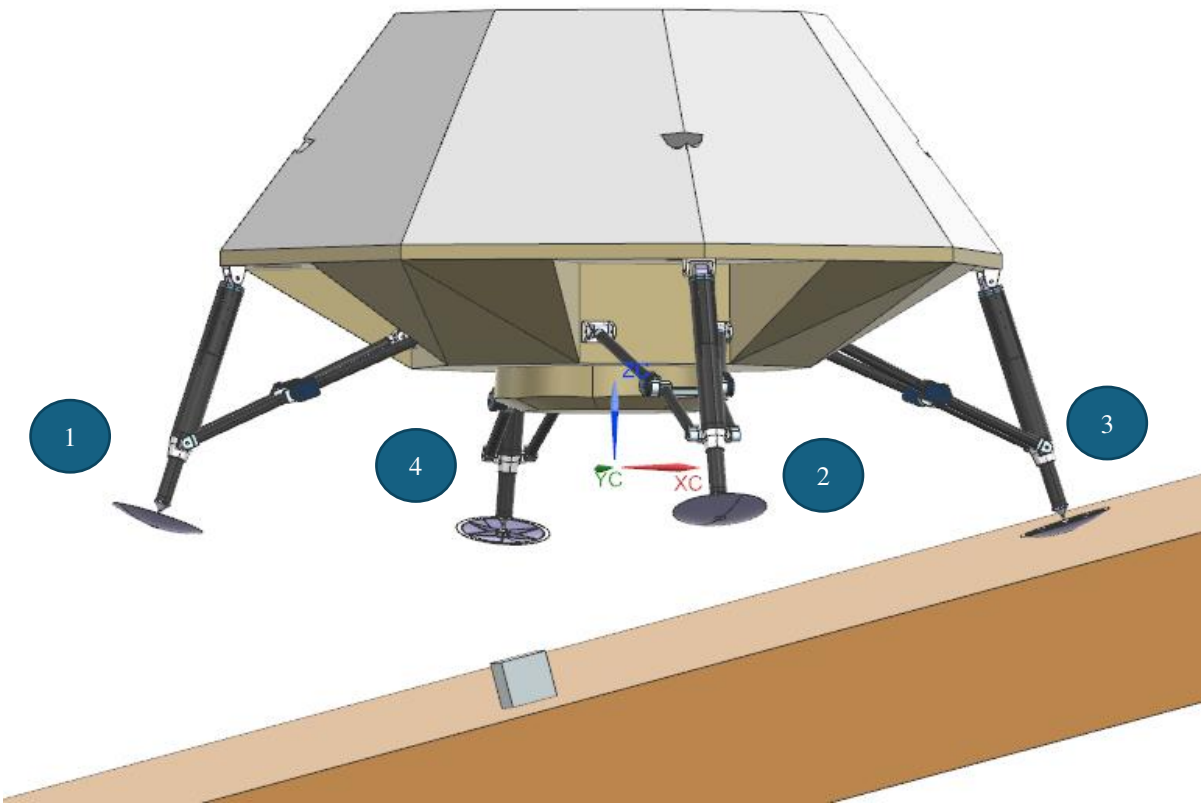


Figure 66: legs numerations, case 10

7.1.1 Initial condition

The lander is ready to land.

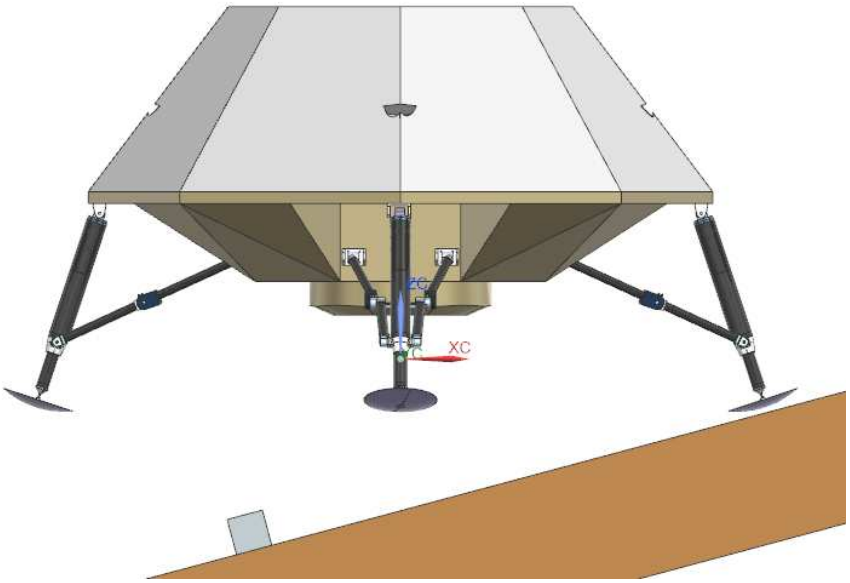


Figure 67: initial condition phase, case 10

7.1.2 First impact

The first leg that impact the land is the leg 1 and its crush-box starts to deform.

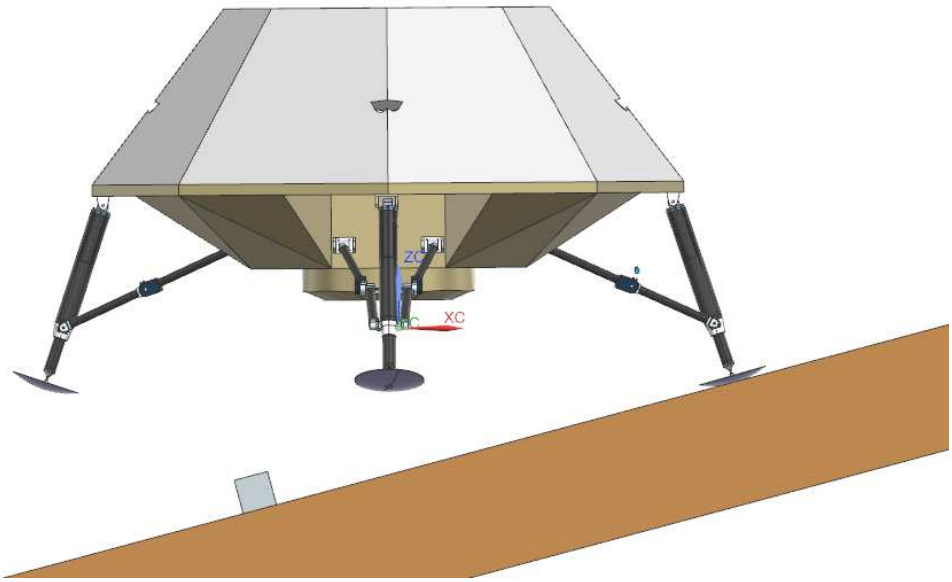


Figure 68: first impact phase, case 10

7.1.3 Impact of other legs and sliding

Before hurt the rock, the lander has a short sliding

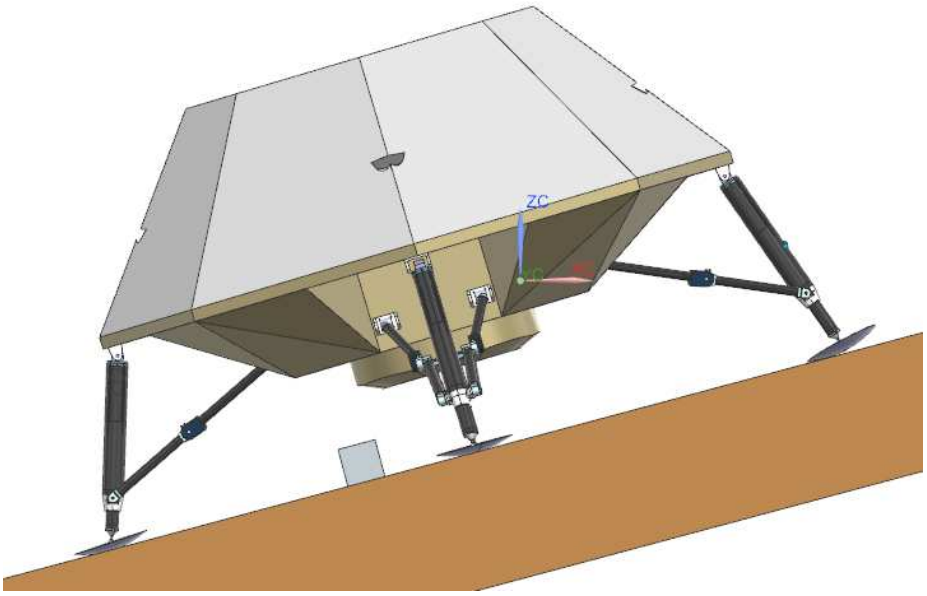


Figure 69: impact of other legs and sliding phase, case 10

7.1.4 Impact with the rock

The leg 2 impact with the rock.

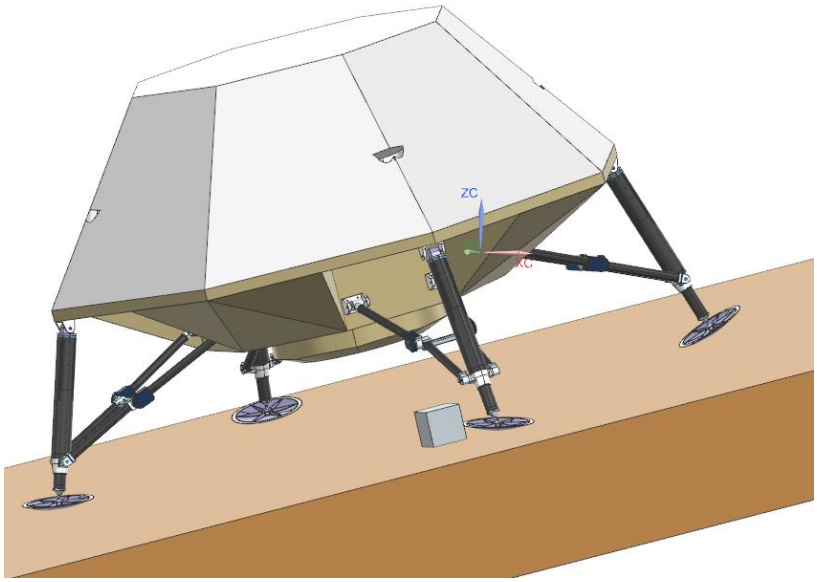


Figure 70: impact with the rock phase, case 10

7.1.5 Bounce

The leg 2 bounces with the rock.

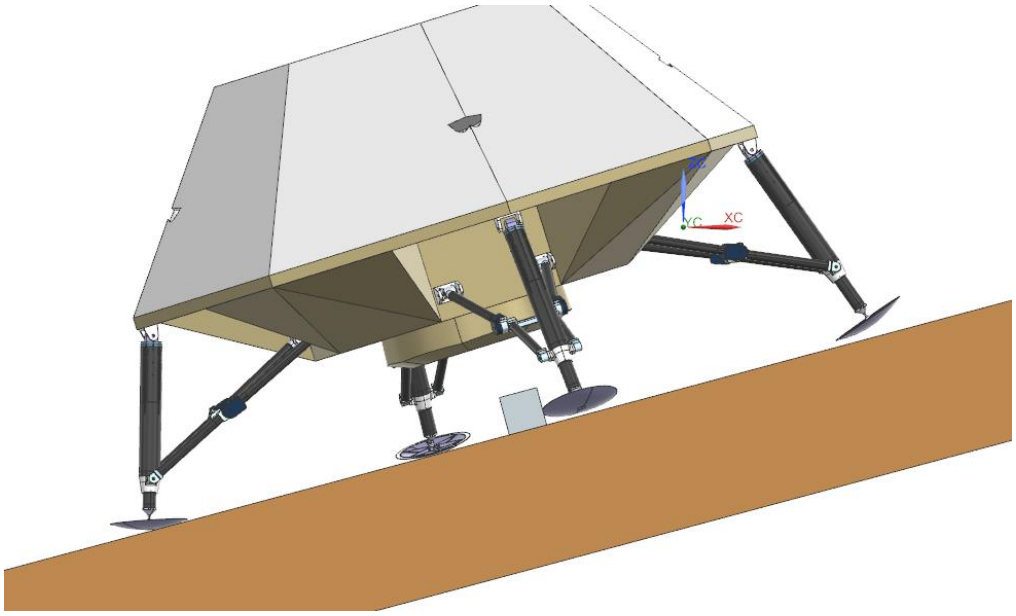


Figure 71: bounce phase, case 10

7.1.6 Second impact with the rock

The leg 2 retouch the rock.

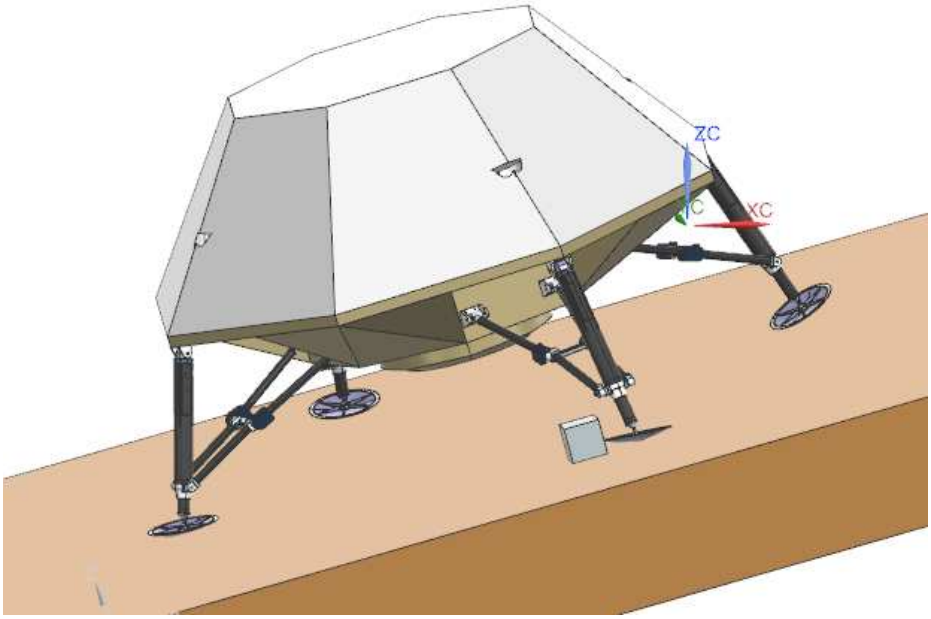


Figure 72: second impact with the rock phase, case 10

7.1.7 Rotation

The lander rotates around the “axis” created by the contact of the leg 2 with the rock

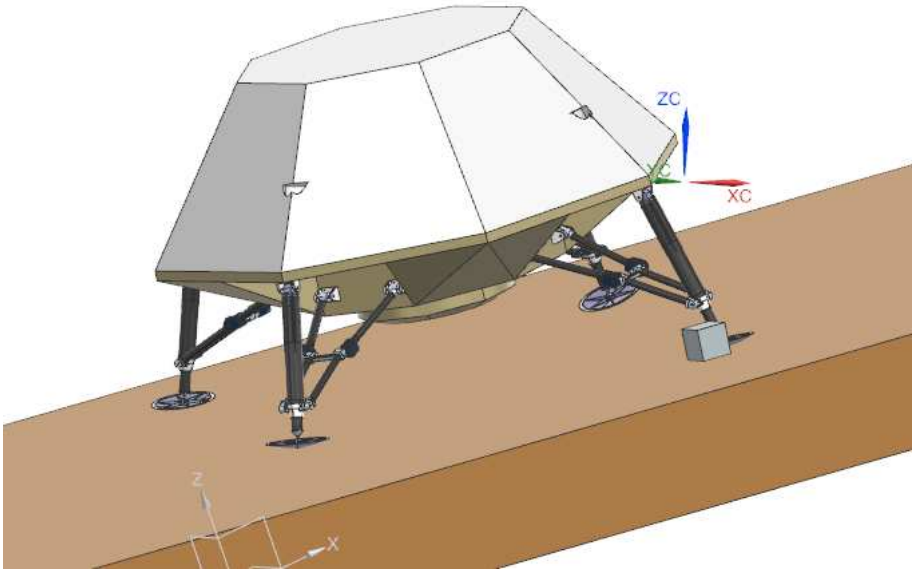


Figure 73: rotation phase, case 10

7.2 Crush-box deformation – single cartridge

In the figure below, one can see the comparison graph of the four crush-box deformation.

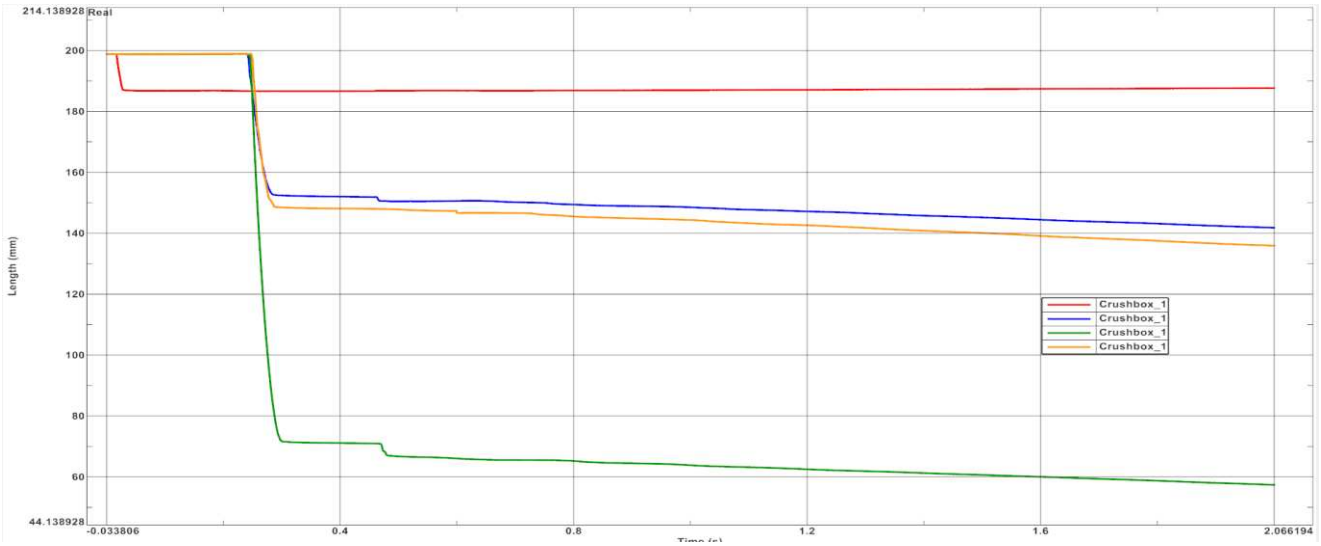


Figure 74: crush-box deformation – case 10, single cartridge

	CRUSHBOX 1	CRUSHBOX 2	CRUSHBOX 3	CRUSHBOX 4
INITIAL VALUE	198.8	198.8	198.8	198.8
FINAL VALUE	187	142	57	137
% DEFORMATION	5.18	32.53	94.41	34.65

Table 11 : crush-box deformation – case 10, single cartridge

7.3 Impact loads – single cartridge

The graphs show in the next parts have been normalized and smoothed in order to have a better view and to help to understand better the trends.

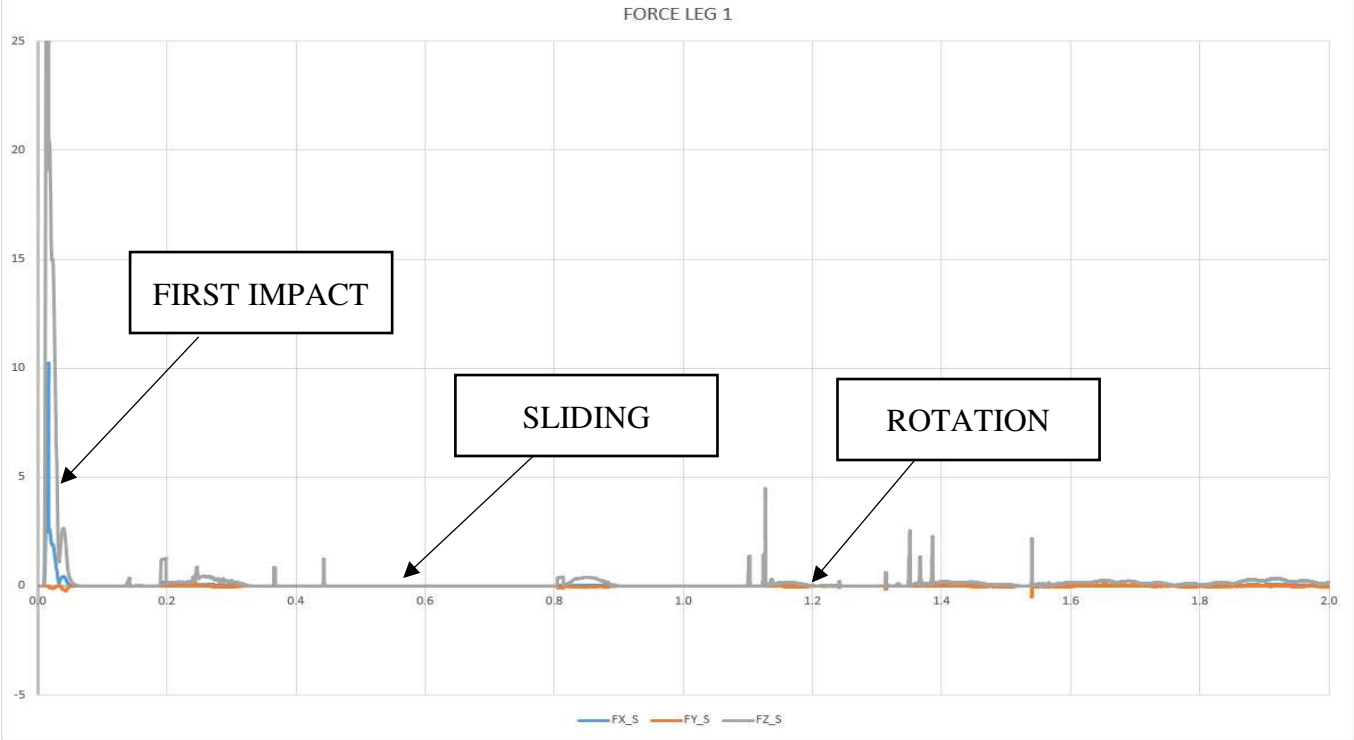


Figure 75: impact loads – leg 1, case 10, single cartridge. Dimensionless force (Y), time in s (X)

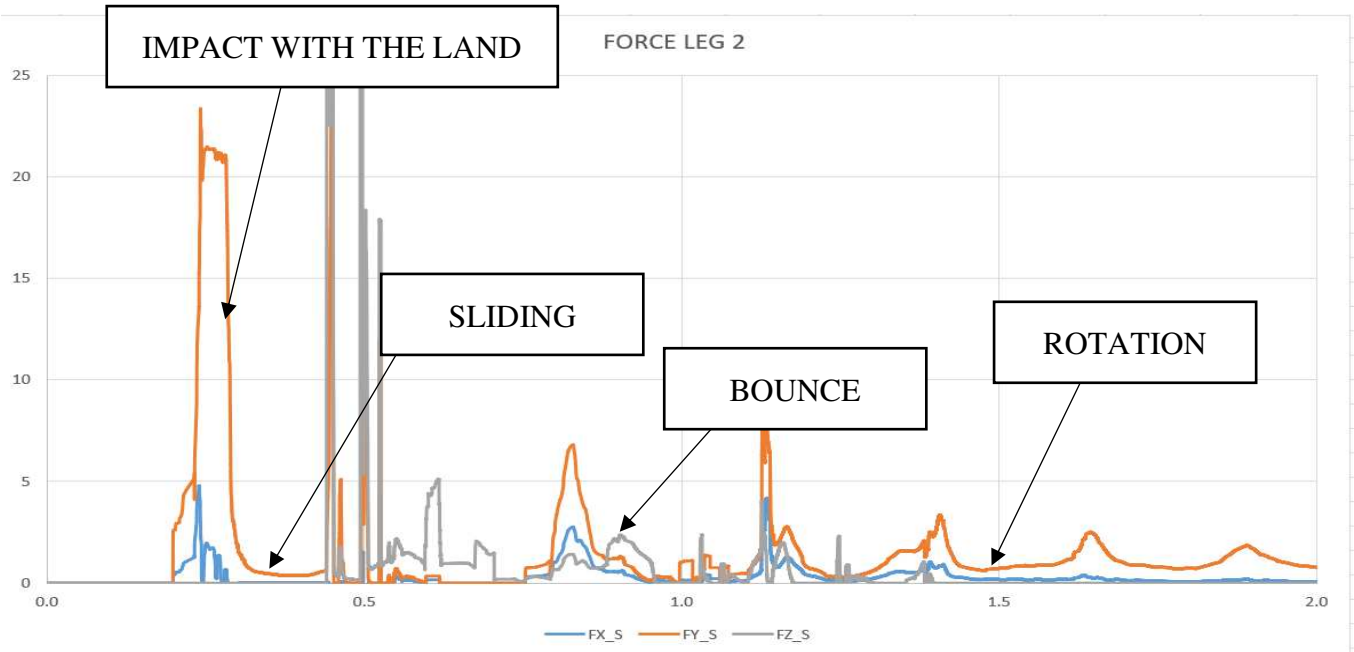


Figure 76: impact loads – leg 2, case 10, single cartridge. Dimensionless force (Y), time in s (X)

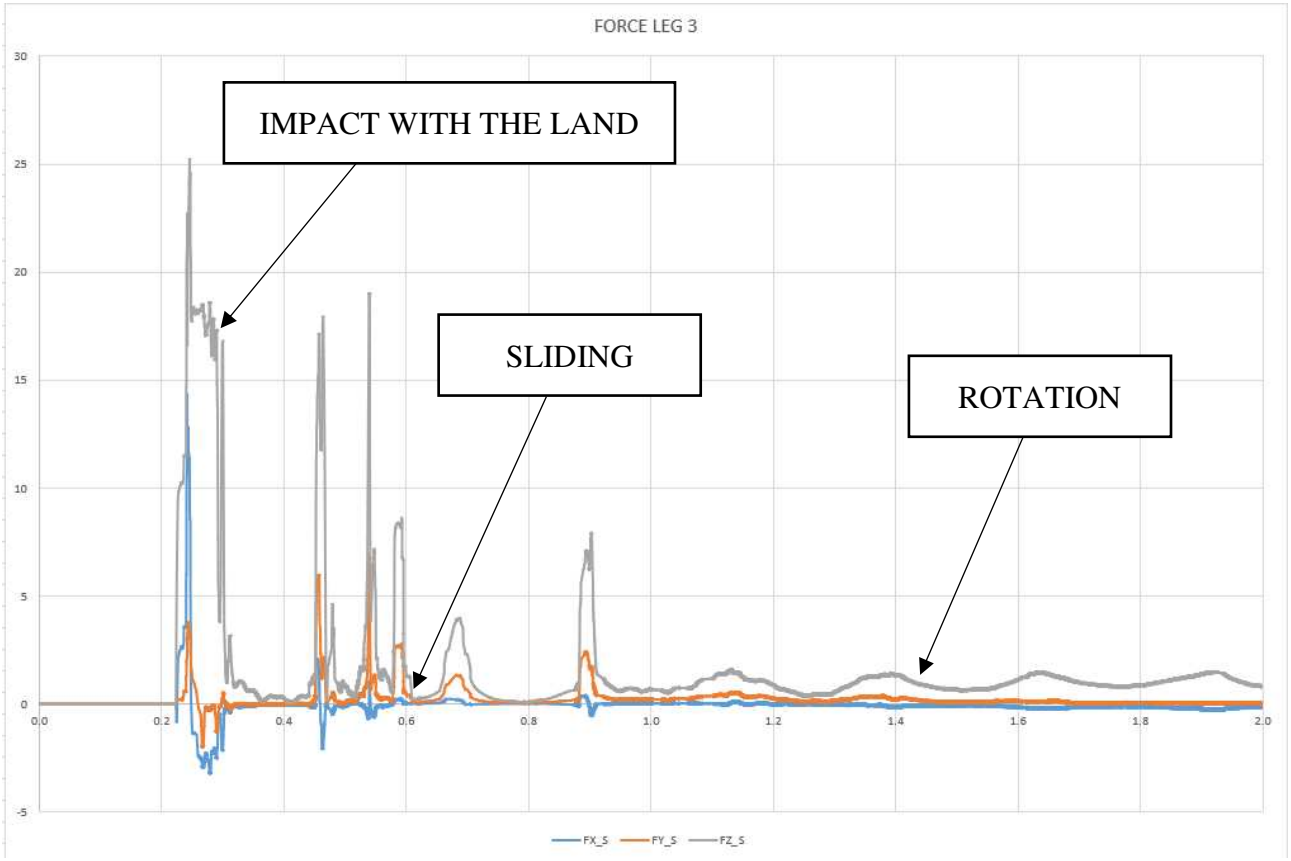


Figure 77: impact loads – leg 3, case 10, single cartridge. Dimensionless force (Y), time in s (X)

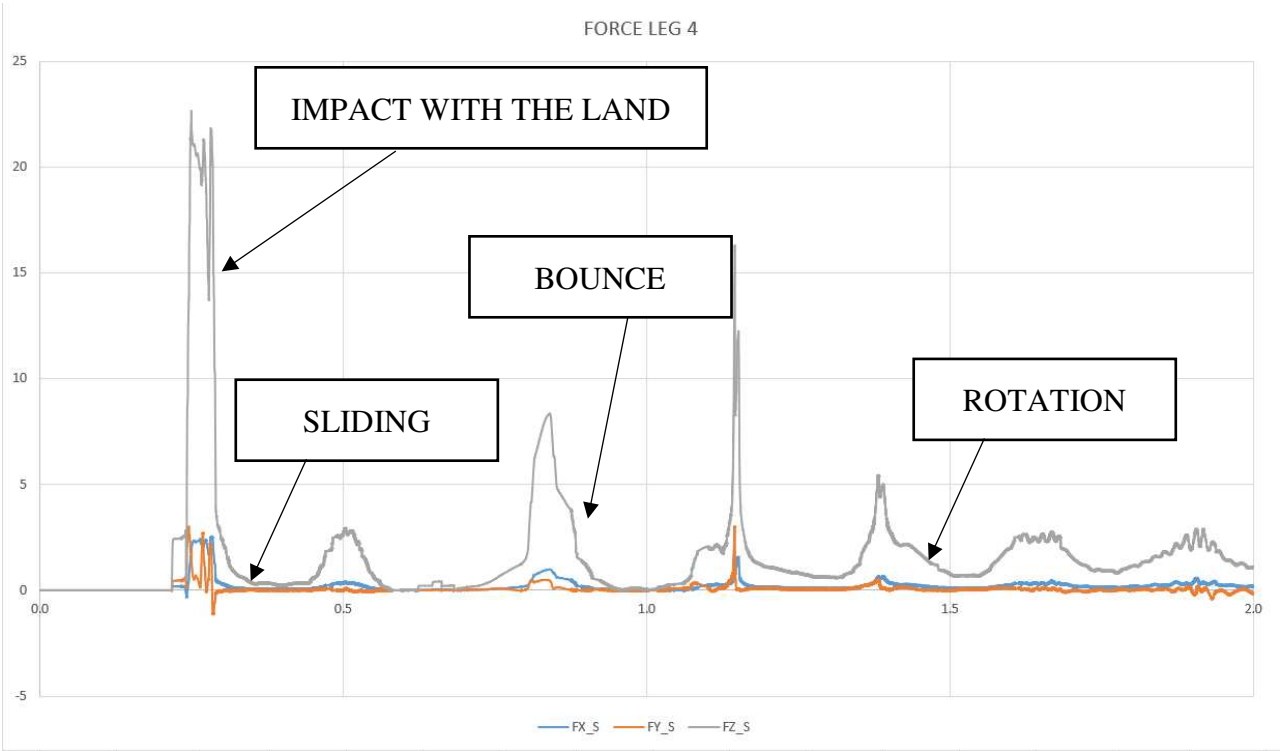


Figure 78: impact loads – leg 4, case 10, single cartridge. Dimensionless force (Y), time in s (X)

7.4 Crush-box deformation – double cartridge

In the figure below, one can see the comparison graph of the four crush-box deformation.

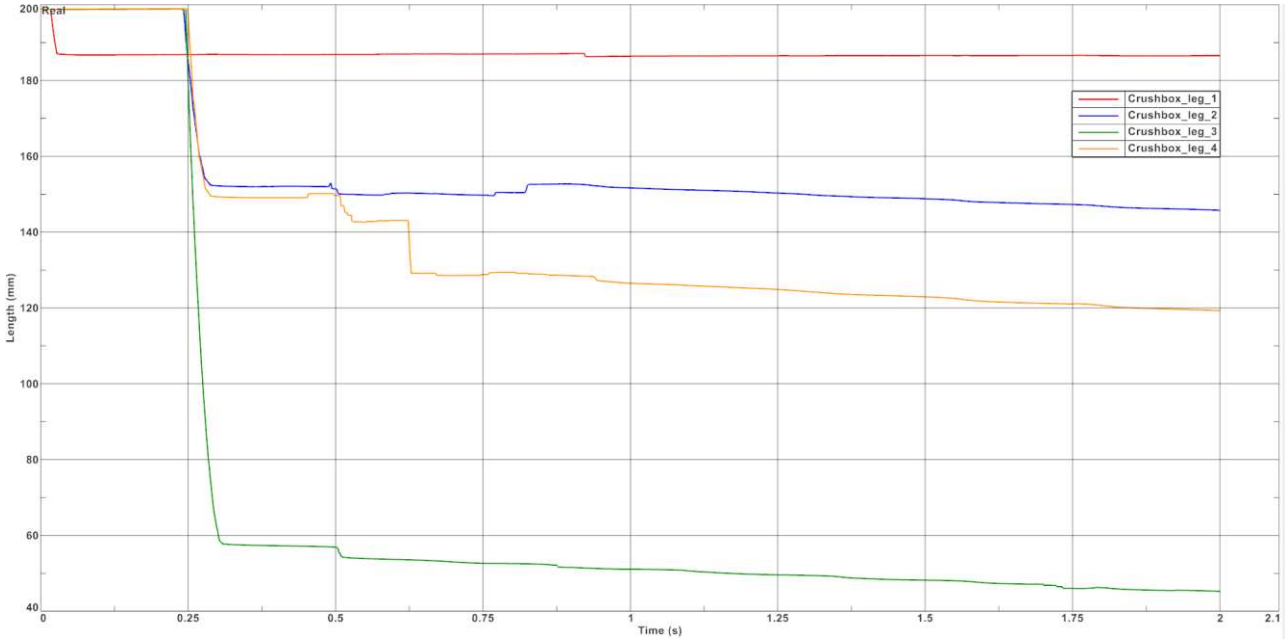


Figure 79: crush-box deformation – case 10, double cartridge

	CRUSHBOX 1	CRUSHBOX 2	CRUSHBOX 3	CRUSHBOX 4
INITIAL VALUE	198.8	198.8	198.8	198.8
FINAL VALUE	186	144	44	119
% DEFORMATION	6.43	27.56	77.86	40.14

Table 12 : crush-box deformation – case 10, double cartridge

7.5 Impact loads – double cartridge

The graphs show in the next parts have been normalized and smoothed in order to have a better view and to help to understand better the trends.

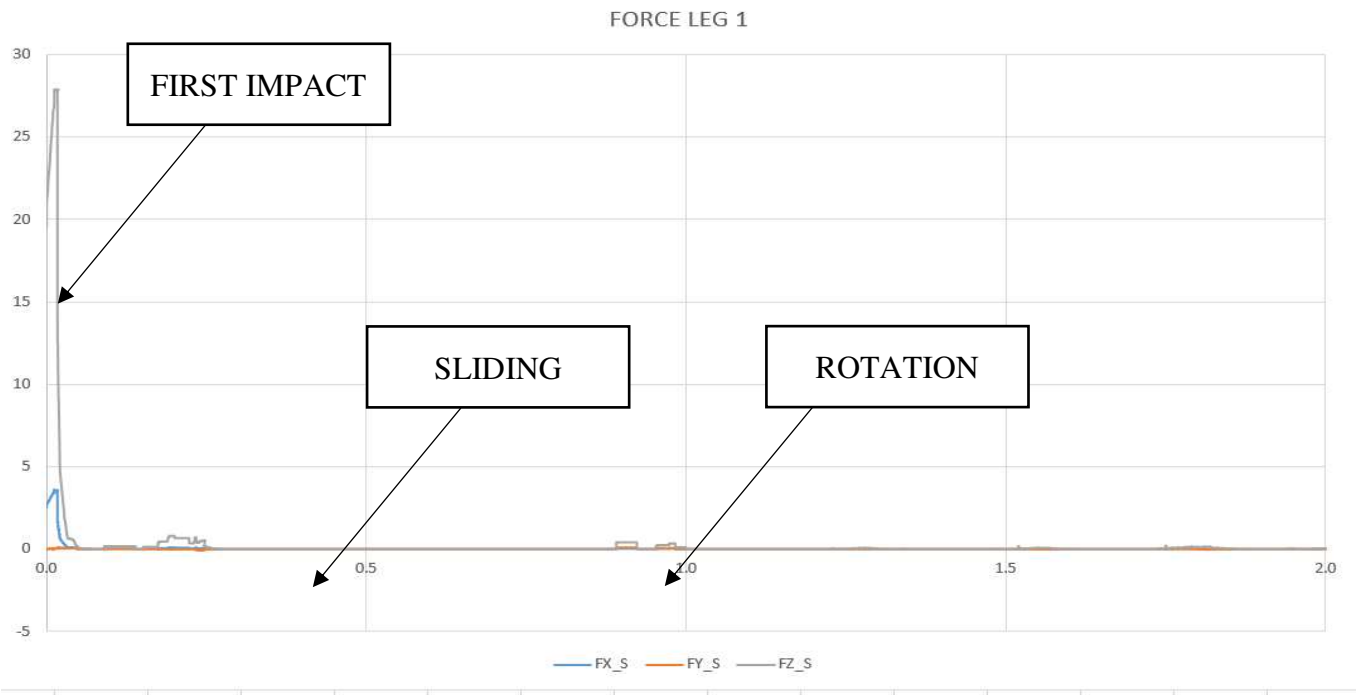


Figure 80: impact loads – leg 1, case 10, double cartridge. Dimensionless force (Y), time in s (X)

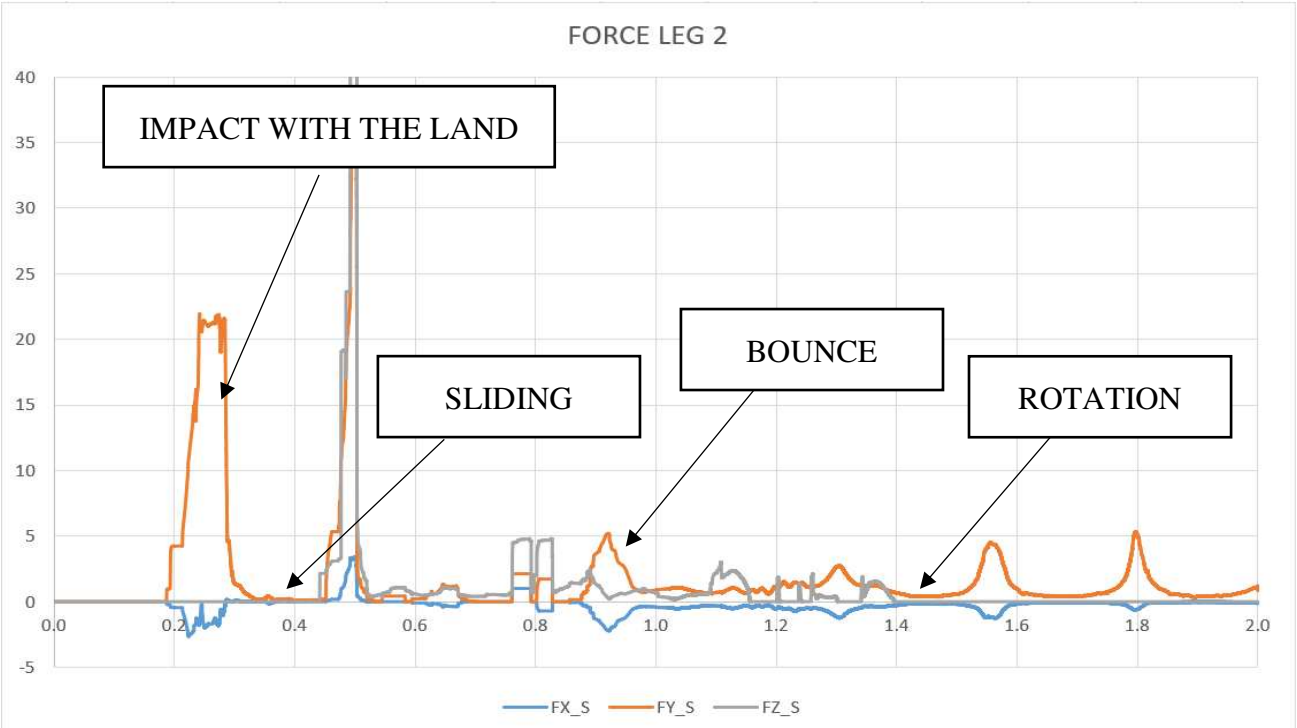


Figure 81 impact loads – leg 2, case 10, double cartridge. Dimensionless force (Y), time in s (X)

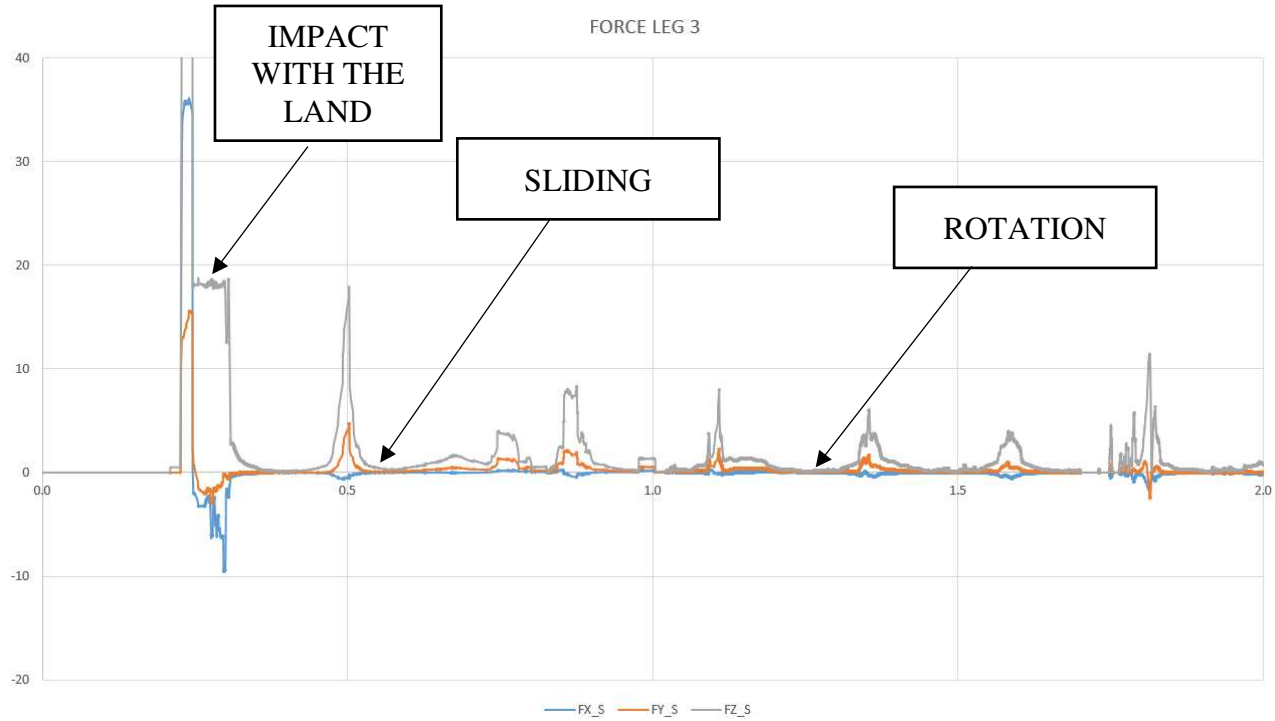


Figure 82: impact loads – leg 3, case 10, double cartridge. Dimensionless force (Y), time in s (X)

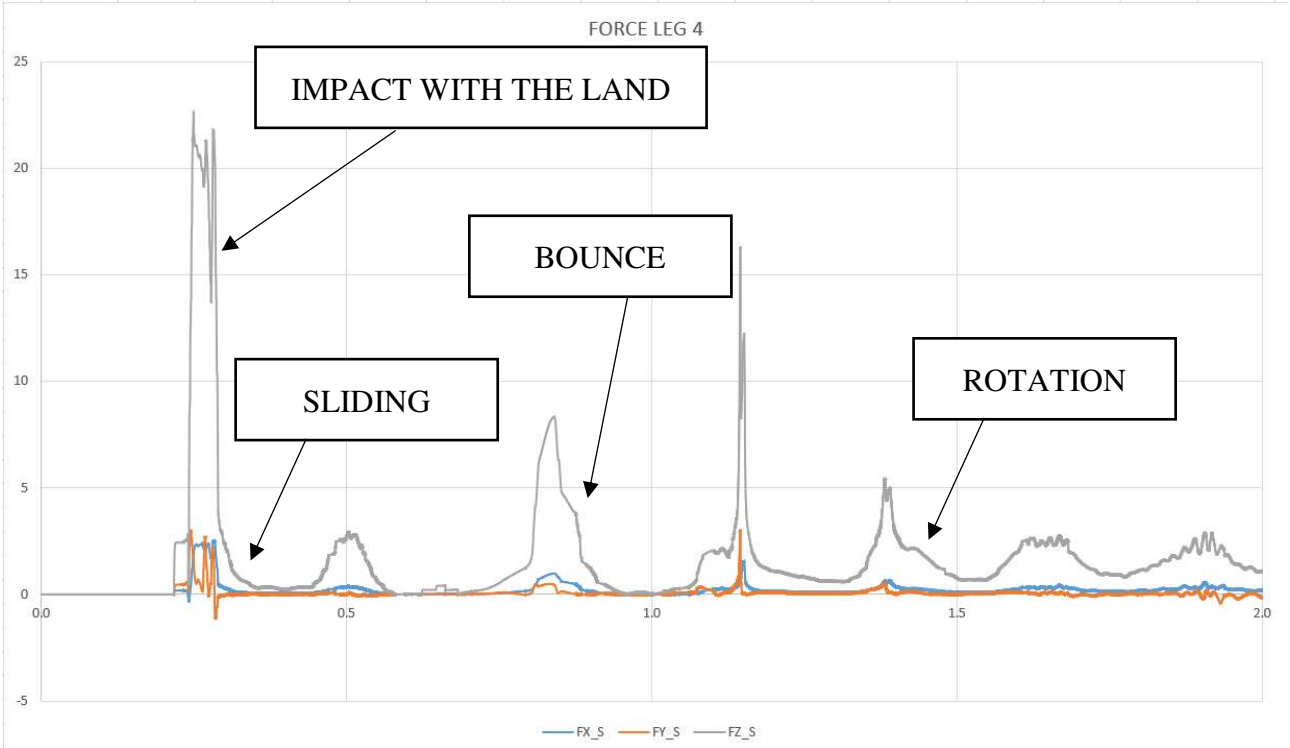


Figure 83: impact loads – leg 1, case 10, double cartridge. Dimensionless force (Y), time in s (X)

CHAPTER 8 : NEW CASE TEST

In order to further investigate a potential worst-case landing scenario, a new case was analyzed. The main objective of this case is to assess how different landing conditions develop as the inclination of the lander increases. The lander continues to make the first contact with the ground using only one leg. For simulation purposes, the lander's inclination is not directly altered; instead, the inclination of the terrain is increased. During the initial phase of the simulation, it became necessary to increase the stiffness of the footpad springs.

8.1 Initial condition

In the following table, a summarize of the initial conditions is shown

	Value
Land's inclination	23.5°
Lander's inclination	0°
Vz	-2.5 m/s
Vx	-2 m/s
Spring's stiffness	(NORMALIZED VALUE) 5.35 N/mm → 6.42 N/mm

Table 13 : initial conditions of new case test

8.2 Landing's dynamics

The landing's dynamics are similar to the case 9 previously studied. The most critical point that deserve attention is the contact of the leg 3 with the land (and the consequential force at footpad) and the possibility of overturning.

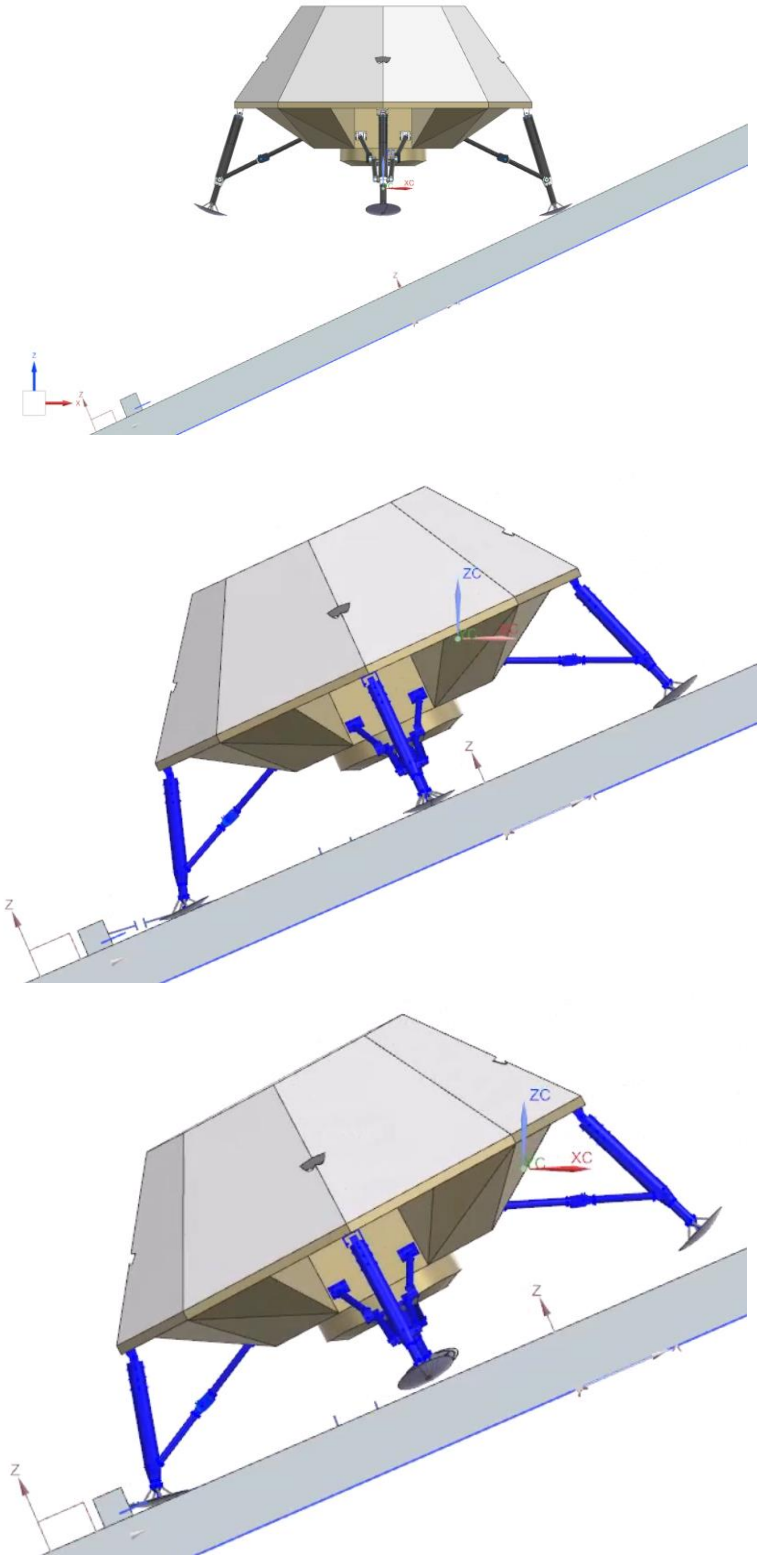


Figure 84: dynamics of landing of new case test

8.3 Stability index

In order to verify if the criterion of the stability index are satisfied, the parameters before discussed in the paragraph 3.3 are calculated

- $H_{m=}\ 1270{,}304\ mm$
- $H_i = 2451{,}148\ mm$
- $H = 1778\ mm$

$$K_s = \frac{2451 - 1270.304}{1956 - 1270.304} = 1.72$$

The criterion is satisfied because the Ks is higher than 1,5.

8.4 Impact loads

For this new case test, one has analyzed only the Fz and the Fx force of the leg 3

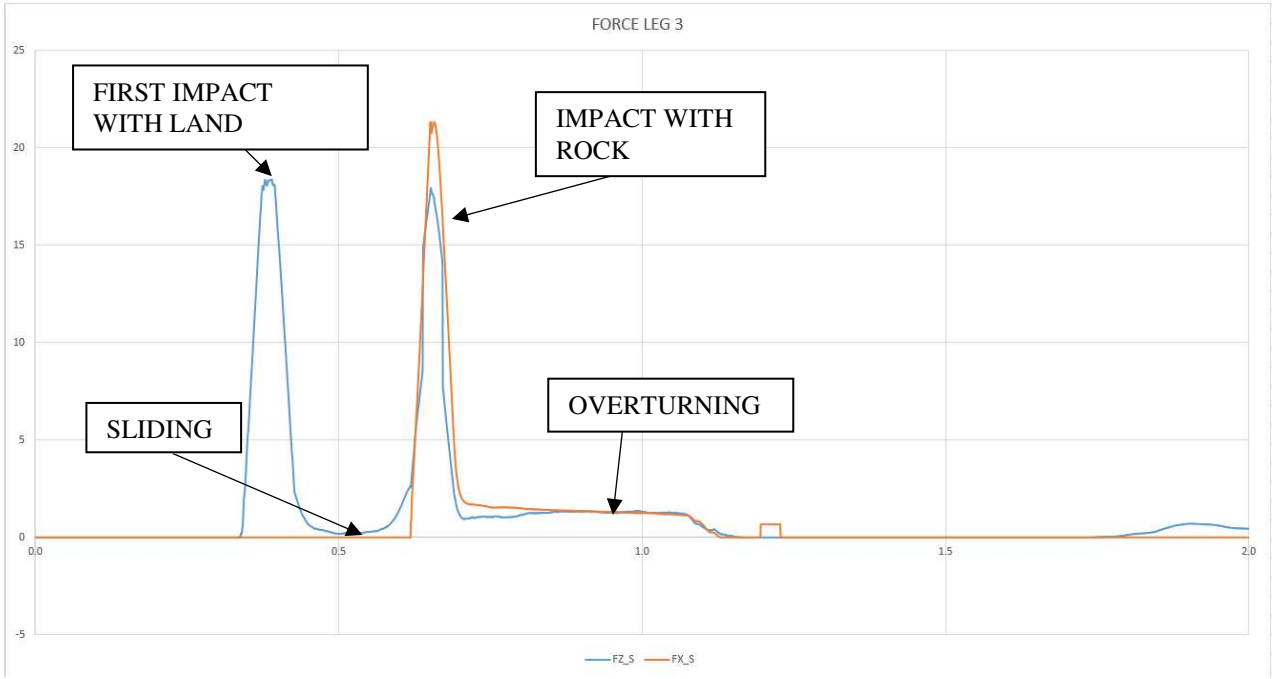


Figure 85: impact loads – leg 3, new case test, single cartridge. Dimensionless force (Y), time in s (X)

The results are particularly interesting, as they show that even though the lander does not fail structurally, the forces on the footpad are significantly higher compared to those in Case 9. The peak force in the Z-axis reaches values above 2000 N (non-normalized, extracted directly from the actual

graph). This new test case highlights the need to explore alternative lander design strategies, as well as to carefully consider the selection of both the landing site and the lander's dimensions.

CHAPTER 9 : DOUBLE CARTRIDGE COMPARISON

Another important factor analyzed is the selection of the crush-box stiffness. Specifically, several simulations were carried out to observe how the deformation behavior of the crush-box changes with different stiffness values. The case evaluated is the case 9.

9.1 Crush-box choice

Starting from the selected crush strength values (in Newtons), the following table presents the parameters used for the simulations. In particular, the directions corresponding to the different values were chosen to evaluate how the presence or absence of symmetry in the stiffness of the two crush-boxes could influence the simulation outcomes. The values are normalized.

	FORCE CRUSH-BOX 1	FORCE CRUSH-BOX 2	TYPE
THESIS	13,012 N	5,219 N	REFERENCE
TEST 1	9,26 N	7,790 N	LOW ASYMMETRY
TEST 2	13,009 N	4,143 N	STRONG ASYMMETR
TEST 3	4,143 N	13,009 N	INVERTED STRONG ASYMMETR

Table 14 : crush-box data for double cartridge comparison

9.1 Results

In the following paragraphs, one can see the values of the deformation, compared with the ones of the reference. For each test, some considerations are made.

9.1.1 TEST 1

In the following table, on can see the final length of the crush-box, at the end of the landing. One wants to remember that the initial value is 198.8 mm.

	FINAL LENGTH (REFERENCE)	FINAL LENGTH (TEST 1)
LEG 1	188 mm	187 mm
LEG 2	136 mm	136 mm
LEG 3	6 mm	18 mm
LEG 4	127 mm	135 mm

Table 15 : reference vs test 1 comparison between the final length of crush-box

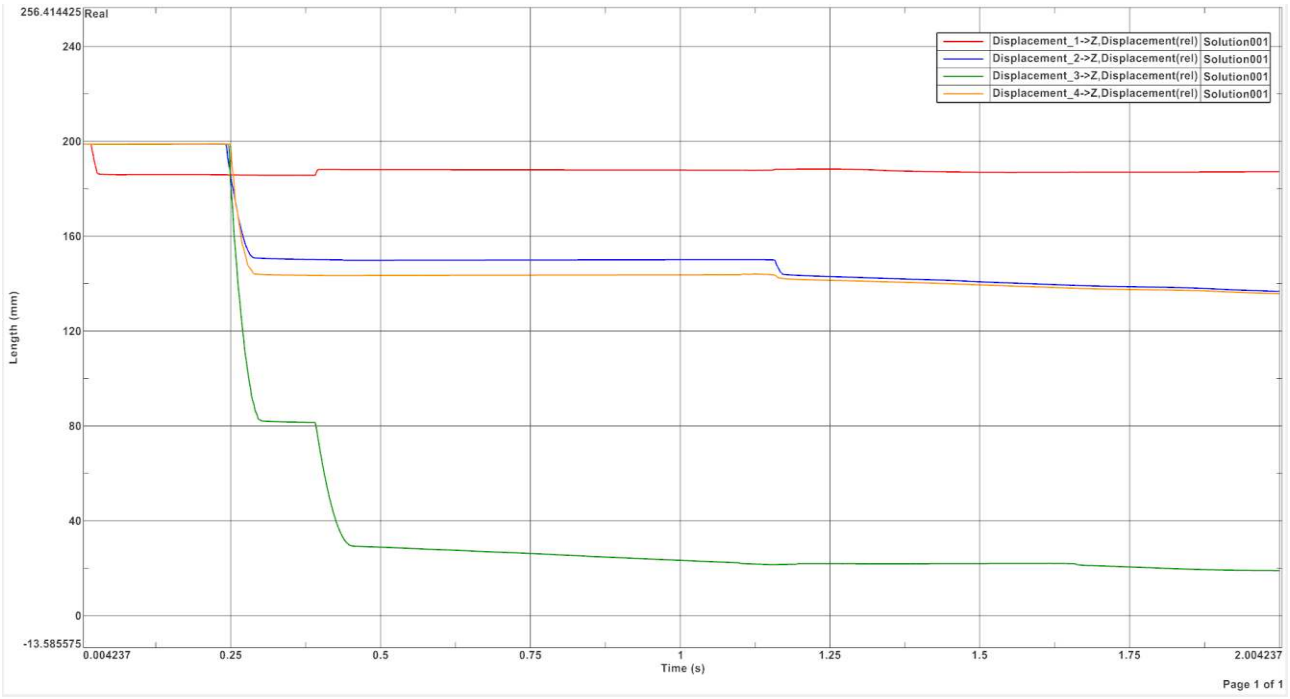


Figure 86: crush-box deformation, test 1

Stability index:

$$K_s = \frac{2451 - 1270.304}{1956 - 1270.304} = 2.28$$

Test 1 demonstrates that employing two cartridges with nearly equivalent stiffness yields results that do not significantly deviate from the reference condition. However, when analyzing the total crush-box deformations, it becomes evident that the final overall length of the crushbox in legs 3 and 4 is greater than in the reference configuration. Legs 3 and 4 are the most stressed components.

Specifically, leg 3 plays a crucial role during the "first stabilization" phase and also it is the leg that impacts the rock. A smaller deformation in this leg may indicate reduced energy absorption by the damping system, potentially resulting in higher loads transmitted to the lander structure. Similarly, leg 4, subjected to the highest vertical force due to the dynamic modeling setup, also shows a reduced crushbox deformation. This once again suggests a lower energy dissipation capacity of the crushbox in this configuration.

9.1.2 TEST 2

In the following table, on can see the final length of the crush-box, at the end of the landing. One wants to remember that the initial value is 198.8 mm.

	FINAL LENGTH (REFERENCE)	FINAL LENGTH (TEST 1)
LEG 1	188 mm	187 mm
LEG 2	136 mm	138 mm
LEG 3	6 mm	2.5 mm
LEG 4	127 mm	134 mm

Table 16 : reference vs test 2 comparison between the final length of crush-box

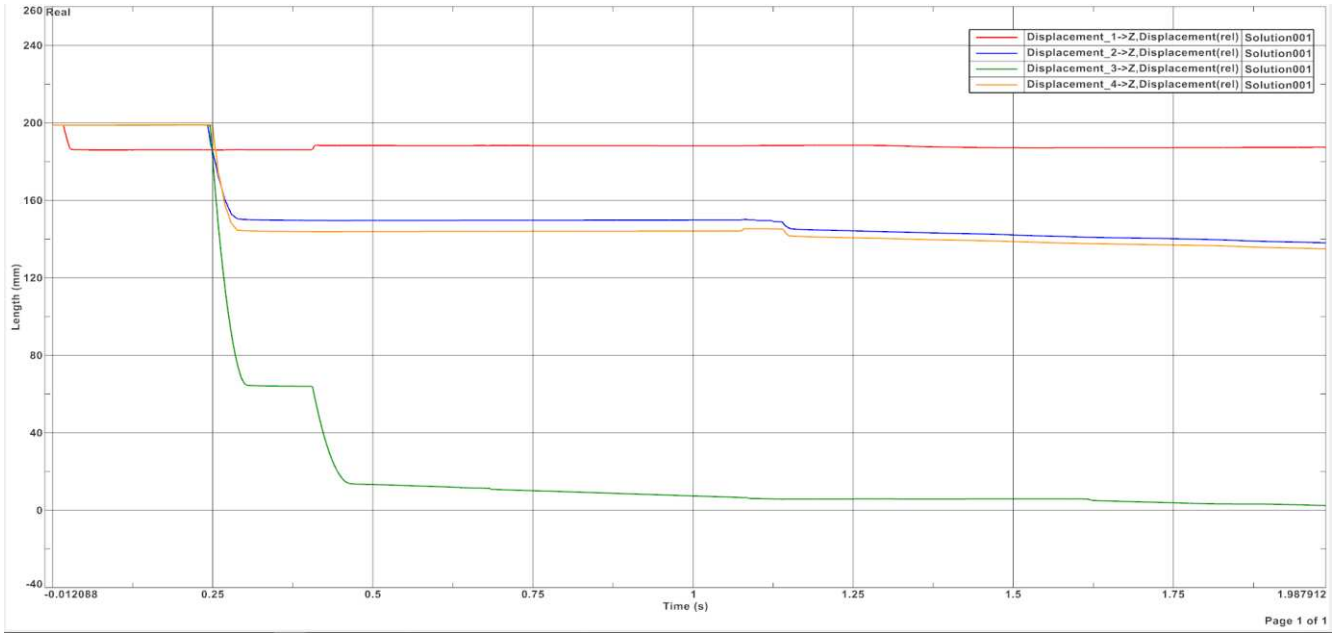


Figure 87: crush-box deformation, test 2

Test 2 indicates that this configuration also adapts well to the landing dynamics. The final overall length of crushbox 4 is greater than its initial value; however, crushbox 3 exhibits a shorter final

length. This observation could suggest a potential opportunity to leverage this configuration to increase energy absorption at leg 3.

9.1.3 TEST 3

In the following table, on can see the final length of the crush-box, at the end of the landing. One wants to remember that the initial value is 198.8 mm.

	FINAL LENGTH (REFERENCE)	FINAL LENGTH (TEST 1)
LEG 1	188 mm	175 mm
LEG 2	136 mm	136 mm
LEG 3	6 mm	- mm
LEG 4	127 mm	13 mm

Table 17 : reference vs test 3 comparison between the final length of crush-box

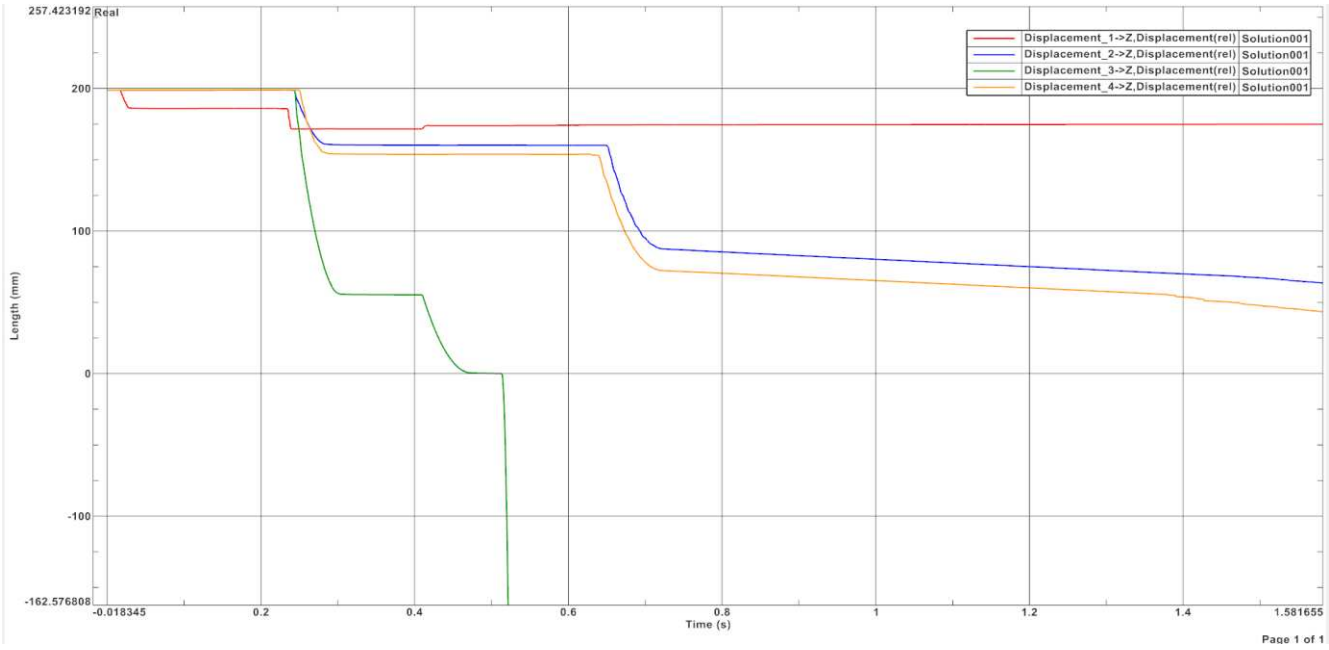


Figure 88: crush-box deformation, test 3

Test 3 failed to complete the full landing sequence. The crush-box configuration proved inadequate to manage the forces generated during touchdown. In particular, leg 3 experienced forces during the initial stabilization phase that were sufficiently high to cause structural failure.

9.2 Conclusion

These tests provided valuable insights, firstly into which double-cartridge honeycomb configurations are capable of ensuring a safe landing, and secondly into the force distribution and deformation behavior associated with each setup. These preliminary results may serve as a foundation for further investigations aimed at optimizing honeycomb selection, in order to achieve the best possible trade-off between structural stiffness and energy absorption capability.

CHAPTER 10 : COMPARISON SINGLE AND DOUBLE CARTRIDGE

In the following chapter, the single and double cartridge configurations are compared to evaluate their respective advantages and disadvantages, as well as their influence on the results. The case take in consideration is the case 9.

10.1 Comparison: crush-box deformation

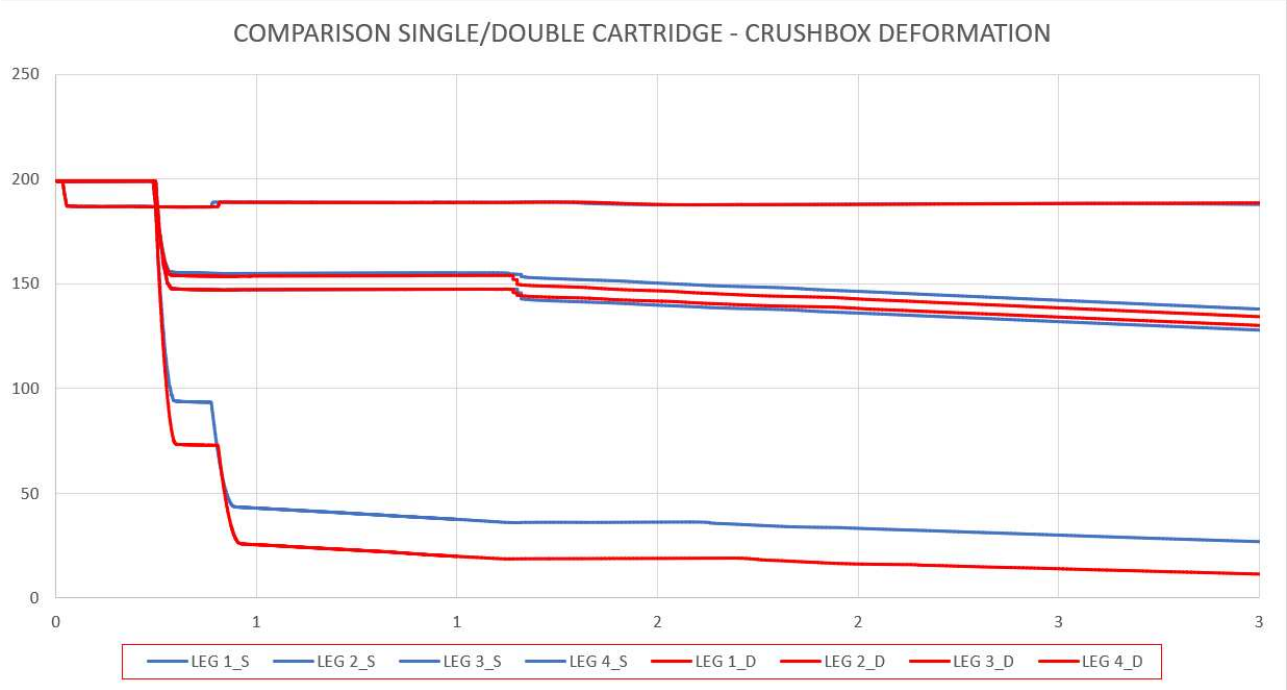


Figure 89: crush-box deformation comparison, single vs double cartridge

As can be observed from the graphs below, the trend between the single-cartridge and double-cartridge configurations remains fairly similar, with the exception of leg 3, where the crush boxes exhibit greater deformation. This deviation highlights a localized structural difference that may influence the overall behavior of the system under load. From the comparison, it can be inferred that the double-cartridge configuration demonstrates a more favorable performance in terms of energy absorption. In particular, the increased capacity of the double-cartridge setup to dissipate impact energy suggests a higher level of structural efficiency and improved crashworthiness

10.2 Comparison: vertical loads

On the figure below, one can see the force at the contact between the footpad 3 and the land. It can be observed that the double-cartridge configuration shows a marginal advantage under vertical loading conditions. Overall, the differences are not drastic, but they indicate that the selection of the optimal configuration should consider the predominant load orientation in the intended application.

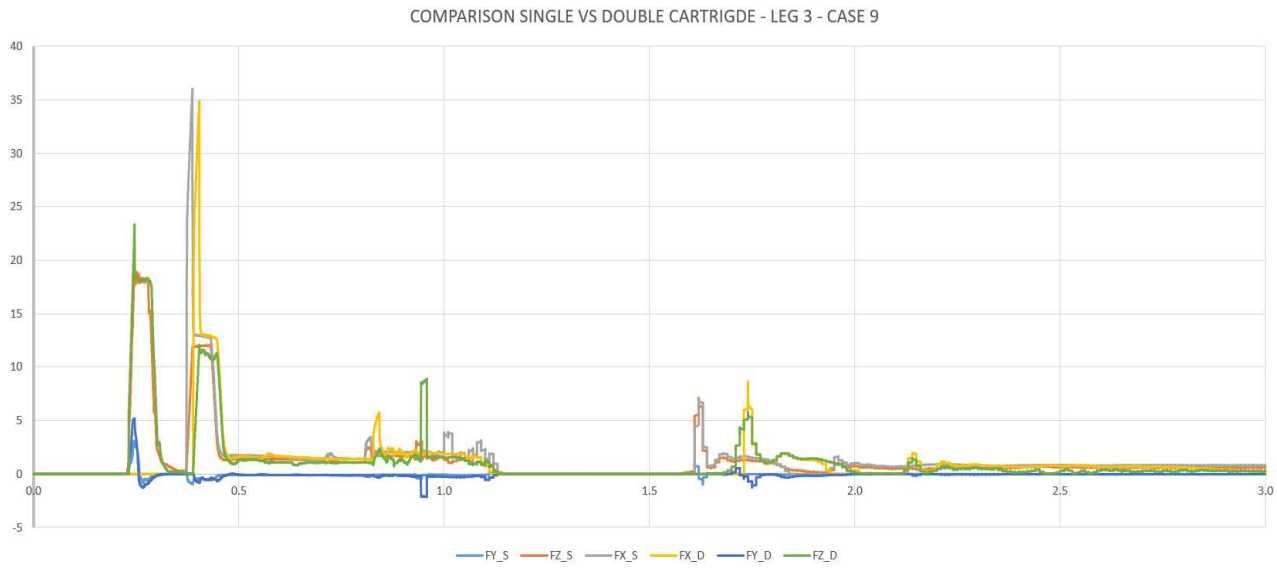


Figure 90: vertical loads comparison, single vs double cartridge

10.3 Comparison: acceleration

The graphs present a comparative analysis of the vertical and horizontal acceleration components recorded during the lander's descent and touchdown. It can be observed that, although the overall differences between the two configurations are not particularly significant, the dual-cartridge system results in slightly lower vertical accelerations, indicating a marginal improvement in the mitigation of the downward impact forces. Conversely, the horizontal accelerations, which are directly related to the interaction with surface obstacles, exhibit an opposite trend: in this case, the single-cartridge configuration achieves marginally lower values. This suggests that while the dual-cartridge setup is more effective in reducing vertical loads, the single-cartridge arrangement provides a modest advantage in limiting lateral impact stresses.

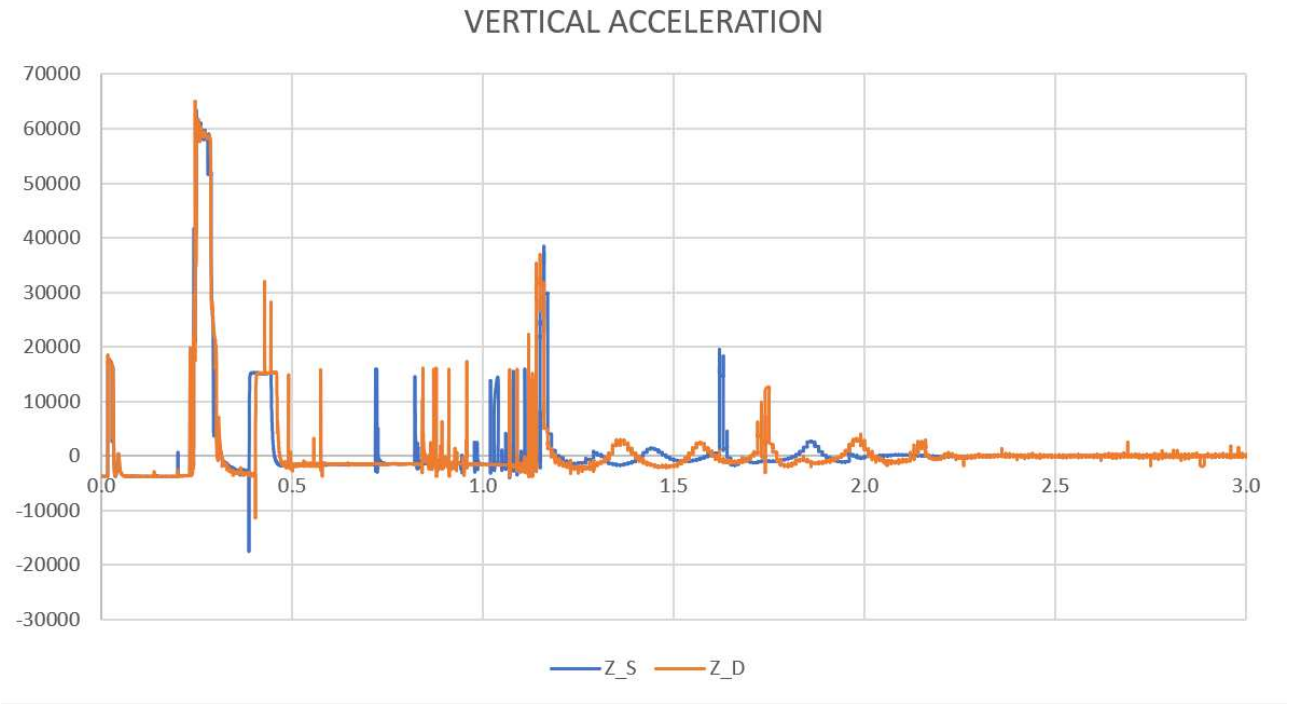


Figure 91: vertical acceleration comparison, single vs double cartridge

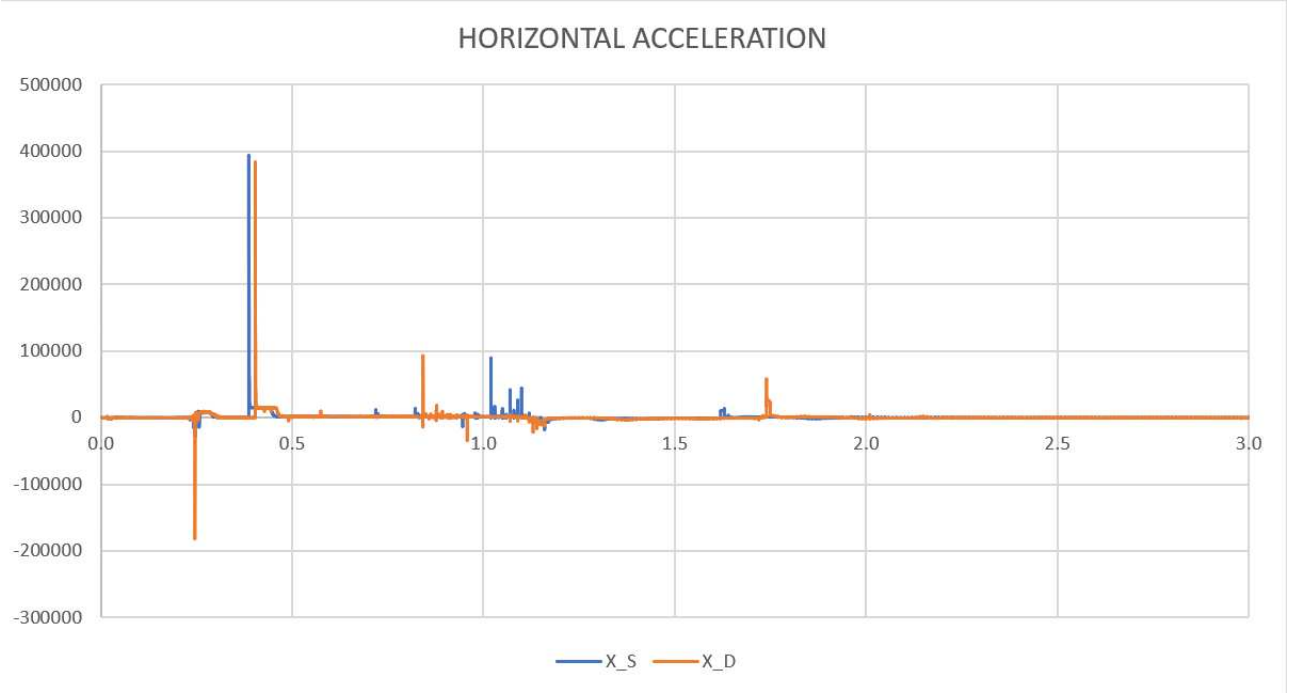


Figure 92: horizontal acceleration comparison, single vs double cartridge

10.4 Comparison: force at joints

In this section, the graphs of the forces acting on the Latch and Brackets components are presented. Since these components are actually duplicated on both the right and left sides of the structure, only one representative case is reported here, as the corresponding graphs exhibit a very similar trend.

10.4.1 Comparison: force at latch

It can be observed that, at the instant corresponding to the impact with the obstacle, the latch is subjected to a significant load, which would cause the leg to fold back if it were not restrained by the latch itself.

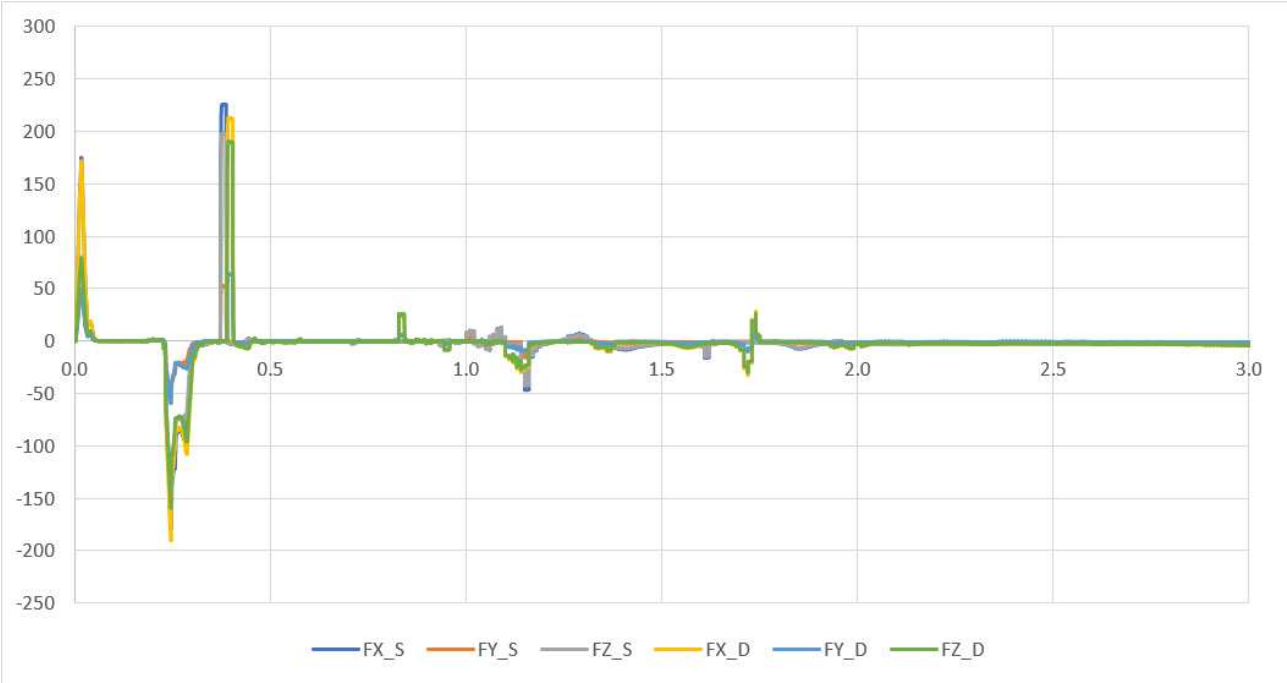


Figure 93: force at latch comparison, single vs double cartridge

10.4.2 Comparison: force at bracket

In the graph below, the forces acting on the bracket are illustrated. It can be clearly observed that, in the double-cartridge configuration, the resulting forces are higher when compared to the single-cartridge setup. This indicates that the presence of two cartridges leads to an increased load transfer to the bracket, which in turn may result in greater mechanical stresses on the component.

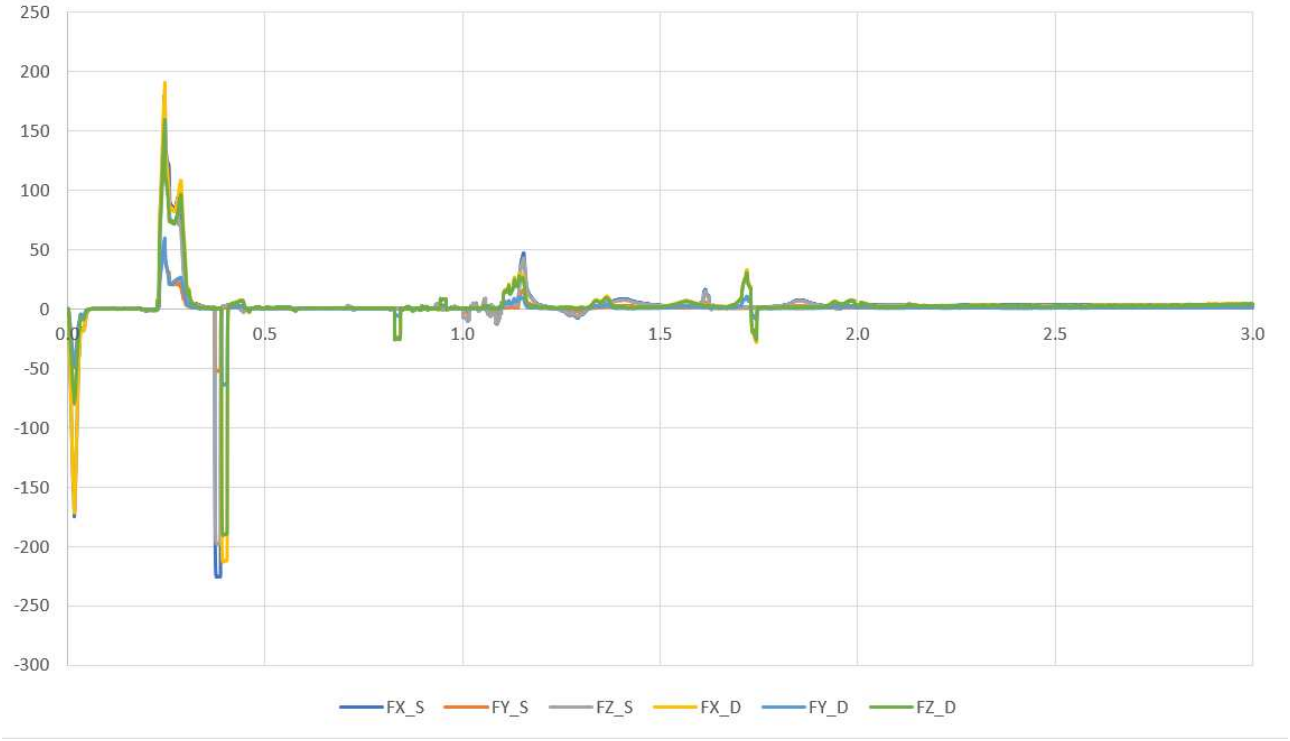


Figure 94: force at bracket comparison, single vs double cartridge

10.5 Comparison overall review

The table below summarizes the comparison between the single-cartridge and dual-cartridge layouts, drawing on the simulation outcomes discussed earlier. Different performance aspects are taken into account to assess which configuration can be considered more suitable.

In terms of cartridge deformation, a larger deformation is interpreted as beneficial, since it corresponds to a higher amount of energy being dissipated during landing. Concerning the loads transmitted to the Latches, Brackets, and Fixing Supports, the preferable configuration is the one that limits the mechanical stresses acting on these parts.

When examining accelerations, both in the vertical and horizontal directions, the configuration producing the lowest values is regarded as the most favorable, as reduced accelerations help safeguard the lander's structure and internal equipment. Finally, for clearance, the configuration that provides the greatest distance from the ground is considered to offer the best overall performance.

	SINGLE CARTRIDGE	DOUBLE CARTRIDGE
CRUSHBOX DEFORMATION		X
FORCE AT LATCH	X	
FORCE AT BRACKET	X	
VERTICAL ACCELERATION		X
HORIZONTAL ACCELERATION	X	
CLEARANCE		X
STABILITY INDEX	X	

Table 18 : overall comparison between single and double cartridge

CHAPTER 11 : CONCLUSION

The aim of this thesis was the development and conceptual validation of a Landing Leg System (LLS) intended for a space exploration module. The analysis was carried out through Multibody Dynamics (MBD) simulations implemented in Simcenter 3D, with particular attention to landing scenarios involving both direct impacts on inclined terrain and frontal or lateral collisions with rocky obstacles. An additional scenario characterized by particularly severe conditions was also considered, in order to assess the system's ability to maintain adequate performance even under the most critical circumstances.

A central element of the project was the modeling of an aluminum honeycomb crush-box, designed as an energy absorber to reduce the stress peaks transmitted to the lander during impact. The behavior of the crush-box was reproduced using dedicated scripts capable of simulating the element's force-displacement response and implemented directly within the landing system model. Two configurations were analyzed: a single-cartridge and a double-cartridge design, both evaluated under boundary conditions compatible with a Martian exploration mission. To increase simulation fidelity, the lander model was rendered flexible, while maintaining certain simplifications for components made of composite materials, allowing for a more detailed investigation of the most severe impact scenarios.

The simulations provided valuable insights into the plastic deformations of the crush-boxes, the loads transmitted to the main structural components, the accelerations experienced at the central body's center of mass, and stability indices related to the risk of tipping. The analysis of the results demonstrated that both configurations are capable of effectively absorbing impact energy while maintaining conditions compatible with a safe landing. However, while the overall system response was largely balanced, the double-cartridge configuration showed wider safety margins under the most severe conditions, making it the more suitable reference solution for the future development of the LLS.

In conclusion, the proposed Landing Leg System concept proved to be technically sound and capable of meeting the safety and reliability requirements necessary for space exploration. The results obtained provide a solid foundation for further work, which could be enhanced through additional simulations in supplementary scenarios and experimental validation activities, with the aim of consolidating the system design and progressing toward a future qualification phase.

SUMMARY OF FIGURES

Figure 1: Apollo 11 Lunar Module on the Lunar Surface

Figure 2: Perseverance Rover Conducting Soil Sampling on the Martian Surface

Figure 3: Lateral view of the MML

Figure 4: Inferior view of the MML

Figure 5: Superior view of the MML

Figure 6: Lateral view of the leg

Figure 7: Front view of the leg

Figure 8: External view of the primary strut

Figure 9: Internal view of the primary strut

Figure 10: Secondary strut

Figure 11: Landing footpad

Figure 12: Brackets and fixing support

Figure 13: Representation of four springs in software view

Figure 14: Plascore CrushLite honeycomb damper

Figure 15: Honeycomb damper representation

Figure 16: Double-cartridge crush-box behaviour

Figure 17: Axis orientation

Figure 18: Safety margin

Figure 19: Stability index references

Figure 20: Joints positioning

Figure 21: Joint position in the menu

Figure 22: Joint setting

Figure 23: 3D Contact position in the menu

Figure 24: 3D Contact setting

Figure 25: Marker position in the menu

Figure 26: Marker setting

Figure 27: Sensor position in the menu

Figure 28: Sensor setting

Figure 29: Marker on tube B

Figure 30: Marker on Impact Endstop

Figure 31: Safety clearance

Figure 32: Load position in the menu

Figure 32/1: Load setting

Figure 33: Honeycomb replaced by a couple of force

Figure 34: Anti-pullout simulated by a force on tube B

Figure 35: Step function position in the menu

Figure 36: Step function setting

Figure 37: Mesh parameters

Figure 38: RBE2 positioning

Figure 39: Legs numeration (Case 9)

Figure 40: Initial condition phase (Case 9)

Figure 41: First impact phase (Case 9)

Figure 42: First stabilization phase (Case 9)

Figure 43: Sliding phase (Case 9)

Figure 44: Impact with the rock phase (Case 9)

Figure 45: Overturning phase (Case 9)

Figure 46: Second impact phase (Case 9)

Figure 47: Complete stop phase (Case 9)

Figure 48: Safety margin – case 9, single cartridge

Figure 49: Safety margin graph – case 9, single cartridge

Figure 50: Crush-box deformation – case 9, single cartridge

Figure 51–54: Impact loads – legs 1–4, case 9, single cartridge

Figure 55: Comparison between lander with footpads with different orientation

Figure 56: Contact force footpad-ground with pads inclined

Figure 57: Contact force footpad-ground with pads not inclined

Figure 58: Contact force footpad-ground with high spring stiffness

Figure 59: Contact force footpad-ground with low spring stiffness

Figure 60: Safety margin – case 9, double cartridge

Figure 61: Crush-box – case 9, double cartridge

Figure 62–65: Impact loads – legs 1–4, case 9, double cartridge

Figure 66: Legs numeration (Case 10)

Figure 67–73: Phases of Case 10 (initial condition → rotation)

Figure 74: Crush-box deformation – case 10, single cartridge

Figure 75–78: Impact loads – legs 1–4, case 10, single cartridge

Figure 79: Crush-box deformation – case 10, double cartridge

Figure 80–83: Impact loads – legs 1–4, case 10, double cartridge

Figure 84: Dynamics of landing of new case test

Figure 85: Impact loads – leg 3, new case test, single cartridge

Figure 86–88: Crush-box deformation (Tests 1–3, double cartridge comparison)

Figure 89: Crush-box deformation comparison, single vs double cartridge

Figure 90: Vertical loads comparison, single vs double cartridge

Figure 91: Vertical acceleration comparison, single vs double cartridge

Figure 92: Horizontal acceleration comparison, single vs double cartridge

Figure 93: Force at latch comparison, single vs double cartridge

Figure 94: Force at bracket comparison, single vs double cartridge

SUMMARY OF TABLES

Table 1: Single cartridge crush-box data

Table 2: Double cartridge crush-box data

Table 3: Data of case studies

Table 4: Material of the parts

Table 5: Joints involved

Table 6: Number of bolts involved for joint

Table 7: Values used to represent Martian soil

Table 8: Properties of materials used

Table 9: Crush-box deformation – case 9, single cartridge

Table 10: Crush-box deformation – case 9, double cartridge

Table 11: Crush-box deformation – case 10, single cartridge

Table 12: Crush-box deformation – case 10, double cartridge

Table 13: Initial conditions of new case test

Table 14: Crush-box data for double cartridge comparison

Table 15: Reference vs Test 1 – final length of crush-box

Table 16: Reference vs Test 2 – final length of crush-box

Table 17: Reference vs Test 3 – final length of crush-box

Table 18: Overall comparison between single and double cartridge

BIBLIOGRAPHY

[1] Delage P, Marteau E, et. al.: The mechanical properties of the Martian soil at the InSight landing site. In: Proc. 20th int. conf. on soil mechanics and geotechnical engineering. Sydney, Australia. HAL Id: hal-03806564 (May 2022)